

stellingen ontbreken.

674027

2283855

TR 2881

TR diss 2881.

## Mo/Si multilayer optics for micro-lithography

### PROEFSCHRIFT

ter verkrijging van de graad van doctor

aan de Technische Universiteit Delft,

op gezag van de Rector Magnificus Prof.dr.ir. J. Blaauwendraad

in het openbaar te verdedigen ten overstaan van een commissie,

door het College van Dekanen aangewezen,

op maandag 20 januari 1997 te 10.30 uur

door Harm-Jan VOORMA

doctorandus in de natuurkunde

geboren te Boston (Verenigde Staten van Amerika)

NWO

WTA

STW

De minister van Wetenschap en Cultuur heeft de Nederlandse Organisatie voor Wetenschappelijk Onderzoek (NWO) in het kader van het programma voor de Stimulering van de Wetenschappelijke Onderzoek (STW) een subsidie toegekend voor de realisatie van de Stimulering van de Wetenschappelijke Onderzoek (STW) en de realisatie van de Stimulering van de Wetenschappelijke Onderzoek (STW).

Dit proefschrift is goedgekeurd door de promotoren:

Prof.dr.ir. S. Radelaar

Prof.dr. M.J. van der Wiel

Samenstelling promotiecommissie:

Rector Magnificus,		voorzitter
Prof.dr.ir. S. Radelaar,	Technische Universiteit Delft,	promotor
Prof.dr. M.J. van der Wiel,	Vrij Universiteit Amsterdam,	promotor
Dr. F. Bijkerk,	FOM-Instituut voor Plasmafysica "Rijnhuizen"	
Prof.dr. J.F. van Veen,	Universiteit van Amsterdam	
Prof.dr.ir. P. Kruit,	Technische Universiteit Delft	
Prof.dr. E. Granneman,	Technische Universiteit Delft	
Dr. S. Wittekoek,	ASM Lithography	

Dr. F. Bijkerk heeft als begeleider in belangrijke mate aan het totstandkomen van het proefschrift bijgedragen.



Het onderzoek beschreven in dit proefschrift is uitgevoerd op het FOM-Instituut voor Plasmafysica "Rijnhuizen" (Edisonbaan 14, 3439 MN Nieuwegein, Nederland). Het onderzoek is onderdeel van het onderzoeksprogramma van de Stichting Technische Wetenschappen (STW) en van de Stichting voor Fundamenteel Onderzoek der Materie (FOM), en is financieel ondersteund door STW, de Nederlandse Organisatie voor wetenschappelijk onderzoek (NWO) en het EUREKA programma van het Ministerie voor Economische Zaken.



## Publications

Various chapters of this thesis have been or will be published:

- Chapter 1b: N.B. Koster, H.-J. Voorma, E. Louis, and F. Bijkerk, *Novac*, nov/dec (1996)
- Chapter 2: H.-J. Voorma and F. Bijkerk, *Microelectron. Eng.* **17** (1992) 145-148  
H.-J. Voorma, F. Bijkerk, E. Louis, L. Shmaenok, N. Koster, *Nederlands Tijdschrift fotonica* **3** (1993) 5-9
- Chapter 3: H.-J. Voorma, E. Louis, N.B. Koster, F. Bijkerk and M.J. van der Wiel, *Physics of X-ray Multilayer Structures*, OSA Technical Digest Series, **6** (1994) 134-137  
H.-J. Voorma, E. Louis, N.B. Koster, F. Bijkerk, M.J. van der Wiel, and E. Spiller, submitted to *J. Appl. Phys.*
- Chapter 4: H.-J. Voorma, E. Louis, F. Bijkerk, and M.J. van der Wiel, *MRS sym. proc.* **382** (1995) 375-380  
H.-J. Voorma, E. Louis, N.B. Koster, and F. Bijkerk submitted to *J. Appl. Phys.*
- Chapter 5: H.-J. Voorma, E. Louis, N.B. Koster, D.J. Pfaff, F. Bijkerk, *Proc. Physics of X-ray Multilayer Structures* (1996) 10.6  
H.-J. Voorma, E. Louis, F. Bijkerk, and S. Abdali, to be submitted
- Chapter 6: H.-J. Voorma, G.E. van Dorssen, E. Louis, N.B. Koster, A.D. Smith, M.D. Roper, F. Bijkerk, *Appl. Surf. Sci.* **93** (1996) 221-230
- Chapter 7: H.-J. Voorma, E. Louis, N.B. Koster, F. Bijkerk, T. Zijlstra, L.E.M. de Groot, B.A.C. Rousseeuw, J. Romijn, and E.W.J.M. van der Drift, and J. Friedrich, submitted to *J. Vac. Sci. Technol. B*

Other publications:

1. F. Bijkerk, E. Louis, L. Shmaenok, H.-J. Voorma, M.J. van der Wiel, I.C.E. Turcu, G.J. Tallents, Proc. SPIE **1848** (1992) 516-520
2. F. Bijkerk, E. Louis, L. Shmaenok, H.-J. Voorma, M.J. van der Wiel, R. Schlatmann, J. Verhoeven, E.W.J.M. van der Drift, J. Romijn, B.A.C. Rouseeuw, F. Voß, R. Désor and B. Nikolaus, OSA Proc. Soft X-ray projection lithography **18** (1993) 114-116
3. E. Louis, F. Bijkerk, L. Shmaenok, H.-J. Voorma, M.J. van der Wiel, R. Schlatmann, J. Verhoeven, E.W.J.M. van der Drift, J. Romijn, B.A.C. Rouseeuw, F. Voß, R. Dresor and B. Nikolaus. Microelectron. Eng. **21** (1993) 67-70
4. E. Louis, H.-J. Voorma, N.B. Koster, F. Bijkerk, Yu.Ya. Platonov, G.E. van Dorssen, H.A. Padmore, Physics of X-ray Multilayer Structures, O.S.A. Technical Digest Series 6 (1994) 35-38
5. E. Louis, H.-J. Voorma, N.B. Koster, L. Shmaenok, F. Bijkerk, R. Schlatmann, J. Verhoeven, Yu.Ya. Platonov, G.E. van Dorssen and H. Padmore, Microelectron. Eng. **23** (1994) 215-218
6. F.E. Christensen, S. Abdali, P.K. Frederiksen, A. Hornstrup, I. Rasmussen, N.J. Westergaard, H.W. Schnopper, E. Louis, H.-J. Voorma, N. Koster, H. Wiebicke, I. Halm, U. Geppert, E. Silver, M. Legros, K. Borozdin, K.D. Joensen, P. Gorestein, J.L. Wood and G. Gutman, J. Phys. III (France) **4** (1994) 1599-1612
7. E. Louis, H.-J. Voorma, N.B. Koster, F. Bijkerk, Yu.Ya. Platonov, S. Yu. Zuev, S.S. Andreev, E.A. Shamov, and N.N. Salashchenko, Microelectron. Eng. **27** (1995) 235-238
8. E. Louis, E. Spiller, S. Abdali, F.E. Christensen, H.-J. Voorma, N.B. Koster, P.K. Frederiksen, C. Tarrío, E.M. Gulikson, and F. Bijkerk, Proc. SPIE **2515** (1995) 194-203
9. F. Bijkerk, L. Shmaenok, E. Louis, H.-J. Voorma, N.B. Koster, C. Bruineman, R.K.F.J. Bastiaensen, E.W.J.M. van der Drift, J. Romijn, L.E.M. de Groot, B.A.C. Rouseeuw, T. Zijlstra, Yu.Ya. Platonov, and N.N. Salashchenko, Microelectron. Eng. **30** (1996) 183-186
10. R.C. Constantinescu, H.G. Mullter, J.M. Schins, P. Breger, P. Agostini, H.-J. Voorma, E. Louis, F. Bijkerk, A. Boural, G. Grillon, A. Antonetti, and A. Myszyrowicz, Proc. Super-Intense Laser Atom Physics **IV** (1996) 371-380
11. A.M. Ahsen, K.D. Joensen, P. Høghøj, F.F. Christensen, E. Louis, H.-J. Voorma, Y. Soong, N. White, P.J. Serlemitsos, I. Andersen, Proc. SPIE **2805** (1996) 336-342
12. J. Friedrich, K. Behrens v. Rautenfeldt, M. Fonefett, M. Pretorius, A. Ranck, M. Schroeder, H. Sievers, J. Voss, V. Wedemeier, E. Louis, H.-J. Voorma, N.B. Koster, and F. Bijkerk, Proc. X-ray Microscopy, Würzburg, (1996) in print



Het onderzoek beschreven in dit verslag is uitgevoerd op de afdeling voor  
Plasmatische Kwaliteitscontrole, afdeling van de FOM (Fonds voor  
Onderzoek naar de Wetenschap) en van de Stichting voor Fundamenteel Onderzoek der  
Natuur (Vernieuwingsimpuls) en is financieel  
ondersteund door STW, de Nederlandse Organisatie voor Wetenschappelijk Onderzoek, binnen  
het BUREKA programma van het Ministerie voor Economische Zaken.

## Table of contents

<b>Publications</b>	<b>3</b>
<b>Table of contents</b>	<b>5</b>
<b>1a. General Introduction</b>	<b>9</b>
1. Introduction	9
1.1 Extreme Ultra-Violet Lithography	10
2. Current research topics	12
2.1 Developements in characterization techniques	12
2.2 Improvement of multilayer quality	12
2.3 Fabrication of mirror substrates	13
3. This thesis	14
3.1 Design, construction and alignment of an EUVL system.	14
3.2 Characterization of multilayer mirrors	14
3.3 Optimization of multilayer reflectivity	14
3.4 Fabrication of reflection masks	15
4. Future work	16
4.1 Production of defect free reflection masks	16
4.2 Chemical contamination	16
4.3 Other multilayer materials	16
4.4 Scattering from multilayer optics	17
5. References	17
<b>1b. Coating facility</b>	<b>21</b>
1. Substrate holder	22
1.1 Ion gun	22
1.2 In-situ reflectometer	22
2. References	24
<b>2. Design, construction and alignment of a compact four-mirror projection system for 13 nm radiation</b>	<b>25</b>
1. Abstract	25
2. Introduction	25
3. Design	28
3.1 Projection system and reflection mask	28
3.2 Illuminator	30
4. Tolerances	31
4.1 Surface figure	31
4.2 Surface roughness	32
4.3 Alignment tolerances	33
5. Construction and alignment	34
5.1 Construction of mirror system	34
5.2 Alignment	35
6. Conclusions	36
7. Acknowledgements	36
8. References	36



<b>3. Characterization of multilayers using a new FFT analysis method of grazing-incidence x-ray reflectivity</b>	<b>39</b>
1. Abstract	39
2. Introduction	39
3. Theory of BMFT analysis	42
4. Experimental	47
4.1 Fabrication of multilayers analysed	47
4.2 Reflectivity measurement set-ups	48
5. Result	48
5.1 Application to a Mo/Si multilayer	48
5.2 Application to a Co/C multilayer	51
5.3 Verification of assumptions in theory	53
6. Conclusions	54
7. Acknowledgements	54
8. References	54
<b>4. Temperature induced diffusion in Mo/Si multilayer mirrors</b>	<b>57</b>
1. Abstract	57
2. Introduction	57
3. Experimental	58
3.1 Coating procedure	58
3.2 Multilayer samples	59
3.3 X-ray measurements	60
3.4 High resolution transmission electron microscopy (TEM)	61
4. Results and discussion	61
4.1 Interface roughness	61
4.2 D-spacing	64
5. Diffusion processes	68
5.1 Type of diffusion	68
5.2 Annihilation of free volume	69
5.3 Model	72
6. Conclusions	73
7. Acknowledgements	74
8. References	74
<b>5. Angular and energy dependence of ion bombardment of the Mo/Si multilayer</b>	<b>77</b>
1. Abstract	77
2. Introduction	77
3. Experimental	79
3.1 Multilayer production	79
3.2 Multilayer characterization	79
4. Basic growth equations	80
5. Results	82
5.1 Ion etch yield	82
5.2 Penetration depth	83
5.3 Growth parameters	84
5.4 Interface roughness	87



6.	Conclusions	88
7.	Acknowledgements	89
8.	References	89
<b>6.</b>	<b>Exafs measurements on the structure of Mo/Si multilayers using ion bombardment and increased deposition temperature</b>	<b>91</b>
1.	Abstract	91
2.	Introduction	91
3.	Production of the multilayers	92
4.	Experimental	93
4.1	Small angle reflectivity measurements	93
4.2	Soft x-ray measurements	94
4.3	EXAFS measurements	95
5.	Interpretation of the multilayer EXAFS analysis	102
6.	Conclusions	103
7.	Acknowledgements	104
8.	References	104
<b>7.</b>	<b>Fabrication and analysis of Extreme Ultra-Violet reflection mask with patterned W/C absorber bi-layer</b>	<b>107</b>
1.	Abstract	107
2.	Introduction	107
3.	Mask production	108
3.1	Multilayer production	108
3.2	Production of absorber bi-layer	109
3.3	Patterning	109
3.4	Mask repair options	110
4.	Mask characterization	112
4.1	Small-angle reflectivity measurements	112
4.2	Soft x-ray reflectivity measurements	112
4.3	X-ray photo-electron spectroscopy	112
5.	Results and discussion	112
5.1	Individual process steps of the mask fabrication procedure	113
5.2	Full mask fabrication procedure	114
5.3	Inspection of mask structures	116
6.	Conclusions	117
7.	Acknowledgements	117
8.	References	118
	<b>Summary</b>	<b>119</b>
	<b>Samenvatting</b>	<b>121</b>
	<b>Curriculum Vitae</b>	<b>123</b>
	<b>Dankwoord</b>	<b>125</b>

## General Introduction

### 1. Introduction

This thesis describes the development of x-ray optical elements for micro-lithography, such as mirrors, and the design of an imaging system. The most simple form of an x-ray mirror is a single metal film, which can be used as an x-ray mirror in grazing incidence configuration, i.e. reflecting below the critical angle. Examples can be found in space telescopes [1] and in beam lines at synchrotron radiation facilities. In order to produce x-ray imaging systems with a practical field size using relatively small mirrors, x-ray reflectors have to be developed that can be used in a normal-incidence configuration. The disadvantage of single metal films is the low reflectivity (less than a few per cent) at normal-incidence.

High reflectivity at normal-incidence can be achieved by the use of a multilayer mirror, which consists of a stack of alternating layers of a reflecting material and a spacer material. The high reflectivity is obtained by positive interference of the radiation reflected by the individual layers. The reflectivity is determined by the wavelength given, the angle of the incidence of the radiation and the spacing between the reflecting layers. The relation is formulated in Bragg's law for positive interference:  $n\lambda = 2d\sin\theta$ , where  $d$ , referred to as  $d$ -spacing, is the thickness of one metal layer and one spacer layer, and  $\theta$  is the angle of incidence with respect to the surface of the mirror. A deviation of the  $d$ -spacing or angle of incidence leads to phase differences between the reflected radiation of each interface and, therefore, results in a decrease of the overall reflectivity. This limits the acceptable variation of the  $d$ -spacing of each period, especially for high quality multilayer mirrors. The second issue that needs to be addressed is the interface roughness, because it determines the effective reflectivity of each interface.

At normal-incidence, multilayer mirrors are being used in a broad wavelength range of between 2 and 35 nm using different combinations of multilayer materials [2]. In Figure 1 the measured reflectivity of multilayers at normal-incidence are displayed for various spacer materials [3]. The graph summarizes experimental data from various groups world-wide. The Si and Be based multilayers are of special interest to micro-lithography, because of the high

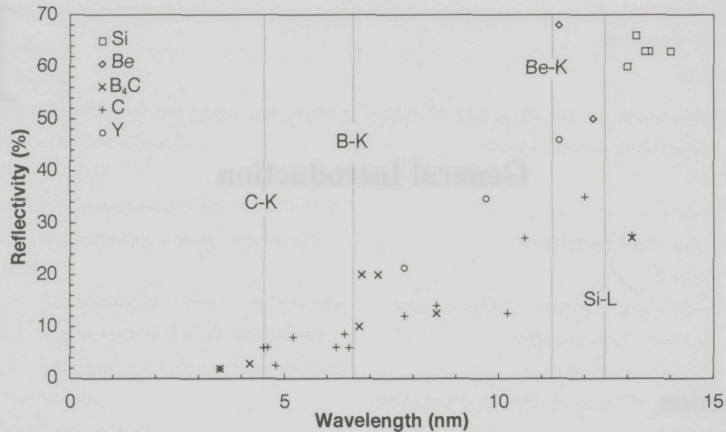


Figure 1 Reflectivity values of multilayer mirrors measured at near-normal-incidence. The lines indicate the absorption edges of the spacer materials.

reflectivity at normal-incidence. Figure 1 also indicates that, moving to smaller wavelengths, the reflectivity decreases, which would reduce the total transmission of any multi-element imaging system.

### 1.1 Extreme Ultra-Violet Lithography

The increasing ability to produce high quality multilayer mirrors has gradually resulted in the development of x-ray optics. One of the advantages of x-ray optical systems is the enhancement of the resolution compared to what is feasible using radiation with longer wavelengths. The ratio between wavelength ( $\lambda$ ) and the numerical aperture (NA) of optical systems determines the diffraction limit of the resolution  $R = k\lambda/NA$ , in which in practice a  $k$ -value of  $> 0.5$  is used. Also the depth of focus scales with the wavelength and the numerical aperture ( $DOF = k\lambda/(NA)^2$ ).

In micro-lithography the diffraction limit has served as an engineering goal in order to decrease the feature sizes on integrated circuits. To increase the resolution the wavelength has decreased from 365 to 248 nm. In the near future lithography systems using a wavelength of 193 nm are expected to be available, which will enable imaging of feature sizes down to 130 nm [4]. The numerical aperture of the optical systems designed nowadays for 248 nm radiation, is at a practical maximum value of approximately 0.5, which limits further improvement of the resolution at reasonable DOF values. These large values for the NA are difficult to produce with the surface accuracy necessary. In order to increase the resolution further, the wavelength again has to be reduced to the few practical. The use of lenses is excluded for wavelengths below 126 nm, because of the high absorption of all materials. As a consequence, the use of mirrors is mandatory. Wavelengths of 157 and 126 nm are considered to offer insufficient gain in relation to the development costs needed, with the



constraint of the difficulty in realizing high NA values for these wavelengths [5]. Also the use of wavelengths between 30 and 70 nm [6], for which some practical material combinations exist, has been investigated. In this wavelength range a maximum theoretical reflectivity of 60% is calculated, but realization of this value is hindered by the severe problem of surface oxidation. However, the calculated reflectivity in the 30 - 70 nm range is lower than values measured for coatings at a wavelength of 13.5 nm. Other advantages for the use of 13 nm radiation are the ability to use a smaller value for the NA, and a higher resolution, a larger depth of focus, and a higher throughput compared to longer wavelengths [7,8]. This imaging technique is nowadays referred to as Extreme Ultra-Violet Lithography (EUVL).

In the last few years, many optical schemes for EUVL have been designed, of which only a few meet the requirements for lithography in a practical prototype. An example of such a system is described in Ref. [9]. World-wide, a few groups are constructing EUVL systems which enable investigations of certain research aspects for EUVL [10,11]. One of these systems is presented in Chapter 2 of this thesis. It is noted that the use of x-ray optics is only possible provided that good x-ray sources, such as synchrotrons and laser plasma sources, are available [12,13]. For small-scale experiments and industrial applications a laser plasma source has advantages, because it enables a high x-ray yield at relatively low investment costs [14].

### 1.1.1 Multilayer mirrors for EUVL systems

A large part of this thesis is devoted to the fabrication of these x-ray mirrors and reflection masks, which are based on multilayer mirrors. The use of Mo (as the reflecting material) and Si (as the spacer material) is considered to be one of the optimal material combinations for EUVL, because of the high reflectivity, in theory up to 70%, that can be obtained at a wavelength of 13 nm. There is one other possible material combination, Mo/Be, which will be discussed later.

Requirements for EUVL optics are very stringent, indicated by the fact that an economical throughput of exposed wafers requires a reflectivity of the optical elements, which exceeds 60% [14,15]. However, a number of assumptions have been made, such as sensitivity of the resist, the power of the source, and the collection efficiency of the collimator. In this thesis the optical elements are investigated, of which the total transmission (T) scales with:

$$T \propto \int \prod_{i=1}^n R_i(\lambda) d\lambda, \quad (1)$$

in which "n" is the number of optical components and  $R_i(\lambda)$  the reflectivity of the  $i$ -th component as a function of wavelength ( $\lambda$ ). If multilayers can be produced with a reflectivity of for example 65% rather than 60%, the factor T would increase with over 75% in the case of a seven-mirror system. The fabrication of the multilayer mirrors should have a high



reproducibility, because of the stringent requirements for the reflectivity of the multilayer coatings, which is dependent on the d-spacing and interface roughness, and the costly mirror substrates. The need to obtain a constant quality for the multilayer mirrors, justifies the research to determine the tolerances of the fabrication parameters, part of which is described in this thesis. It is not sufficient to determine the optimal value for one parameter, but the entire parameter space has to be investigated to find a global optimum.

## 2. Current research topics

In this sub section some general current topics in the field of multilayer research are shortly reviewed. Although some of the research topics are of general interest in multilayer research, we limit ourselves to those which are of relevance to EUVL.

### 2.1 *Developments in characterization techniques*

In parallel to the increasing availability of x-ray sources, many techniques have become available to characterize multilayer mirrors, such as x-ray fluorescence (XRF) [16], x-ray photo-electron spectroscopy (XPS) and near-normal-incidence reflectivity measurements [17]. However, still one of the most powerful methods of analysis is small-angle-reflectivity measurements using Cu-K $_{\alpha}$  radiation. The measurements are nowadays a standard technique for the characterization of multilayer mirrors. Many groups reported about progress in the characterization methods used, including the development of Cu-K $_{\alpha}$  reflectometers for multilayer research [18,19,20]. Although in principle the analysis can be done, methods which are both fast, accurate, and comprehensive are not yet available.

Diffuse x-ray scattering measurements using Cu-K $_{\alpha}$  radiation at grazing incidence are also applied frequently to characterize multilayer mirrors. This technique has been developed to determine the height distribution of the interface roughness in the lateral and the normal direction with respect to the surface. The latter gives rise to constructive interference radiation scattered from each of the interfaces [21]. Nowadays, this technique is used to obtain understanding of the growth of a layer and the propagation of the roughness through the multilayer, see for example Refs [22,23,24] and Chapter 4 and 5.

### 2.2 *Improvement of multilayer quality*

For the production of multilayer structures several fabrication techniques are available, of which sputter deposition [25] and e-beam evaporation [26] are considered to be the most important. Both techniques enable production of multilayers with a high reflectivity up to 66% [27,28] at near-normal-incidence for radiation around 13 nm.

#### 2.2.1 *Decrease of the interface roughness*

With the given wavelength and material selection, the major factor which determines the final multilayer reflectivity is the interface roughness, which should be as low as possible. This can

be illustrated by the 63% reflectivity for a Mo/Si multilayer with an interface roughness of 0.3 nm rms, while 67% reflectivity will be obtained with an interface roughness of 0.2 nm rms. For the production of large multilayer mirrors for an optical system, the interface roughness has to be controlled over the entire area of the mirror substrates [29,30]. If multilayer mirrors are produced using sputter deposition the interface roughness is optimized by selecting the proper gas pressure and deposition speed [31]. Also ion assisted deposition is used [32]. The use of different sputter target configurations have been tested to obtain a better homogeneity of the interface roughness over the surface. In the case of multilayers produced with e-beam evaporation, the use of an increased substrate temperature [33,34,35] and ion bombardment [28,36,37] are applied.

### 2.2.2 Control of the d-spacing

Obviously, multilayer mirrors for an optical system have more severe requirements than those needed for special research topics. With a wavelength given and a limited width ( $\lambda/\Delta\lambda$ ) of the reflection peak, equal to the effective number of layers that contribute to the reflectivity signal, which is 40 in the case of Mo/Si multilayers used for 13.5 nm radiation, a multi-element optical system requires matching of the d-spacing of the individual components and across the surface. For the production of multilayer mirrors on spherical elements, the use of custom-shaped baffles in the particle stream is applied [38,39]. Up to now, the specification of a variation of the d-spacing of less than 0.5% can be met in practical circumstances [39]. Further improvement can be obtained by the use of variation of the rotation speed of the substrate during deposition [40].

### 2.2.3 Control of stress in multilayer mirrors

The last topic mentioned here is the study on the control of the amount of stress in multilayer mirrors [41,42]. The necessity for such research is found in the stringent requirements for the surface accuracy of the mirror substrates, which will be discussed in the next section. The second application where stress is an important issue, is the production of free-standing Mo/Si multilayers which are used as beamsplitters in interferometers for 13 nm radiation, which are developed for metrology purposes.

## 2.3 Fabrication of mirror substrates

Related to the coating process is the production of mirror substrates with a surface roughness of 0.1 nm and a surface figure accuracy of 0.2 nm. The roughness of the substrates is an important issue, because it is related to the performance of the multilayer mirrors [43]. The requirement for the substrate roughness is kept at a lower value than that of the multilayer coating, to avoid any loss of performance of the multilayer [44]. For most high-quality multilayer mirrors produced on Si wafers, the interface roughness is found to be 0.3 nm. In this thesis a value of 0.2 nm is reported.



The surface figure accuracy is determined by the requirement to obtain a diffraction limited image, for which the rms wavefront error at the image field may not exceed  $\lambda/14$  [45]. The total wavefront error are determined by the optical configuration and by the surface figure errors of the substrates. For most four-mirror imaging systems for EUVL, which are described in literature, the required surface figure accuracy is determined to be 0.2 nm. However, using the fabrication techniques presently available, the requirements for the surface figure and surface roughness cannot be met simultaneously. For this purpose new fabrication and characterization techniques have to be developed. Some studies are being performed in the design and construction of an at-wavelength interferometer [46,47]. Also new types of visible light interferometers are being developed [48], which up to now enable testing of single surfaces with an accuracy better than 0.5 nm rms.

### **3. This thesis**

#### **3.1 Design, construction and alignment of an EUVL system**

In order to obtain experience in specific issues of imaging using 13 nm radiation, an EUV imaging system has been designed, constructed, aligned, and used for first experiments. The entire system consists of a two-mirror imaging system, a reflection mask and an illuminator and is described in Chapter 2. Using this system, a number of research aspects have been investigated, such as imaging in EUV resist, alignment, transmission measurements, and the practical usage of a laser plasma source in the system.

#### **3.2 Characterization of multilayer mirrors**

Concerning small-angle-reflectivity measurements, the analyses are often based on curve fitting, which is not only time consuming, but also depends strongly on the skill of the operator. In Chapter 3 a newly developed method is discussed that allows determination of the multilayer parameters directly from the data of the small-angle-reflectivity measurement. This method does not only determine the d-spacing and the interface roughness, but the average layer thickness errors, and the density of both materials as well. Other advantages are that the method does not require any pre-assumptions, it is fast, and the results are operator-independent.

#### **3.3 Optimization of multilayer reflectivity**

Two additional techniques have been investigated for the fabrication of Mo/Si multilayer mirrors with e-beam evaporation. These techniques are based on increasing the mobility of the atoms during or just after deposition, in order to reduce the interface roughness. The optimization procedures described in this thesis differ from the optimizations performed earlier. Firstly, the d-spacing as well as the interface roughness have been determined, using both near-normal and small-angle reflectivity measurements. The optimal values and possible

changes of the multilayer parameters, have been explained in terms of fundamental processes such as diffusion and viscous flow. Secondly, complete multilayer mirrors have been produced instead of single layers. The latter are more easy to analyse but do not have to result in optimal parameters for the complete multilayer mirrors. Thirdly, instead of optimizing only one parameter, a number of parameters have been optimized simultaneously.

The first technique (Chapter 4) concerns the use of an increased substrate temperature, and has been investigated in a wide temperature range (300 - 550 K). An optimal deposition temperature of 488 K has been found, and a corresponding minimum in the interface roughness of 0.3 nm rms. Within this temperature range two processes are identified that determine the interface roughness: surface diffusion and intermixing. Besides changes in the interface roughness also changes in the d-spacings are observed as a function of time and temperature, which has not been investigated earlier. In this chapter a diffusion process is given which fully describes the observed phenomena.

In Chapter 5 a second additional technique, ion bombardment, is investigated to improve the multilayer quality, i.e. reduce the interface roughness. Directly after deposition of the Si layer, ion bombardment is used to remove an additional layer thickness while simultaneously the surface becomes smoother. In contrast to studies performed earlier, both the ion energy and the angle of incidence have been optimized for full multilayers rather than for single layers. The smoothening effect of ion bombardment is investigated with  $\text{Kr}^+$  ions by varying the ion energy between 300 eV and 2 keV and the angle of incidence between  $20^\circ$  and  $50^\circ$ . The results show that the reduction of the interface roughness is caused by viscous flow during ion bombardment. In contrast to earlier suggestions, the optimal ion beam parameters are achieved at much higher energy and angle of incidence.

Although both optimization techniques, ion bombardment and increased substrate temperature during deposition, result in an almost equal interface roughness, the reflectivity values at near-normal-incidence are significantly different. In Chapter 6 EXAFS measurements are performed to investigate the structure and chemical composition of the layers. Although the results show only minor differences in structures, they do show that in the temperature optimized samples the Si layers contain a large fraction of oxygen (~5%), while the Si layers treated with ion bombardment have an oxygen fraction of less than 0.5%. Contamination of the layers, especially with oxygen, is important to be investigated, because 13 nm radiation is highly absorbed in oxygen.

### **3.4 Fabrication of a reflection mask**

In Chapter 7 a newly developed fabrication procedure for EUVL reflection masks is described. The reflection masks are used as objects in EUVL imaging systems. A special absorber bilayer has been developed, consisting of a C layer (25 nm) and a W layer (40 nm). This combination of materials shows a high absorption of radiation in the W, the excellent etch



selectivity between W and C during patterning, and good prospects for repair of the absorber layer.

#### **4. Future work**

The next four topics that will be discussed are subjects that are suggested for further study and have emerged in part from the work presented in this thesis.

##### ***4.1 Production of defect free reflection masks***

In order to use multilayer mirrors as EUVL reflection masks, the reflectivity of the multilayer mirror should be constant over the entire multilayer surface, and no defects are allowed with sizes down to  $\sim 100$  nm in the case of a system with a demagnification factor of 5. These defects could be dust particles or local deviations of the reflectivity of the multilayer. The best result obtained so far is the fabrication of multilayers with a defect density of  $< 0.01$  cm<sup>-2</sup> [49], while a typical result is  $\sim 0.1$  cm<sup>2</sup> defects. It is noted that the inspection of these multilayers has been performed with a particle counter, which measures the total integrated scatter from a multilayer on top of a Si wafer using visible light. The disadvantage of this technique is that only the top surface is inspected, and that defects in the multilayer are not detected. Better methods to inspect these multilayers are x-ray imaging or x-ray microscopy [50]. The disadvantage is that both methods are very time consuming. In-situ cleaning of substrates with ion bombardment shows good results to reduce the defect density. This technique has to be developed further.

##### ***4.2 Chemical contamination***

A second topic that needs to be investigated is contamination of the multilayer, an effect which could result in increased absorption and therefore lower reflectivity. For 13 nm radiation especially the oxidation of the top layer is an important issue, as is concluded in Chapter 7. It has been suggested that Si is a better top layer than Mo, because of the thinner oxidized layer [51]. However, long term experiments with Mo/Si multilayers produced with e-beam evaporation are not yet performed and might reveal information on possible oxidation. Such investigations should include different top layer materials. Also the reduction of chemical contamination (e.g. oxygen) during deposition should be investigated, as is concluded in Chapter 6 from EXAFS measurements.

##### ***4.3 Other multilayer materials***

Also other multilayer materials for EUVL are under study, such as Mo/Be [52] and Ru/C [53,54]. Especially Mo/Be seems to be a promising candidate, because of the high theoretical reflectivity of 74%. The decrease of the wavelength to 11.5 nm results in a small increase of the resolution and penetration depth into the resist. Whether or not these Mo/Be multilayers

are preferred to Mo/Si multilayers, depends on results on the development of EUV resist for either of the two wavelengths.

#### 4.4 Scattering from multilayer optics

The last topic that is suggested is scattering, of 13.5 nm radiation from a multilayer mirror used at near-normal-incidence [55,56]. Although the amount of scattering from multilayer mirrors is minor, scattering could have an effect on the image formation in an EUVL system. Especially scattering inside the numerical aperture of the system can result in a reduction of the contrast in the image field, which then could lead to a reduction of the resolution. At present, however, no experimental set-ups to measure scattering of 13.5 nm radiation at near-normal-incidence are available.

### 5. References

1. F.E. Christensen, A. Hornstrup, P. Frederiksen, P. Grundsøe, S. Henrichsen, E. Jacobsen, P. Jonasson, M.M. Madsen, C. Nilson, H.W. Schnopper, N.J. Westergaard and P. Ørup, *J. X-ray Sci. Technol.* **2** (1990) 81-94
2. E. Spiller, *X-ray optics*, SPIE, 1996
3. The data indicated are from the table composed at the biennial conference on Physics of X-ray Multilayer Structures. This graph is updated in 1996. The data can be found at the internet: <http://www-cxro.lbl.gov/multilayer/survey.html>.
4. S. Harrell, T. Siedel and B. Fay, *Microelectron. Eng.* **30** (1996) 11-15
5. S. Wittekoek, *Porc. MNE* (1996) Glasgow, in print
6. N. Duddels, *OSA Proc. EUV Lithography*, **4** (1996) 173-177
7. H. Matsumura et al., *Jpn. J. Appl. Phys.* **26** (1987) 487
8. A.M. Hawryluk, and L.G. Seppala, *J. Vac. Sci. Technol. B* **6** (1988) 2162
9. T.E. Jewell, J.M. Rodgers, and K.P. Thompson, *J. Vac. Sci. Technol. B* **8** (1990) 1519-1523
10. D.A. Tichenor, G.D. Kubiak, M.E. Malinowski, R.H. Stulen, S.J. Haney, K.W. Berger, L.A. Brown, R.R. Freeman, W.M. Mansfield, O.R. Wood II, D.M. Tennant, J.E. Bjorkholm A. A. MacDowell, J. Bokor, T.E. Jewell, D.L. White, D.L. Windt and W.K. Waskiewics, *Opt. Lett.* **16** (1991) 1557-1559
11. K. Kurihara, H. Kinoshita, T. Mizota, T. Haga and Y. Torii, *J. Vac. Sci. Technol. B* **9** (1991) 3189-3192
12. F. Bijkerk, E. Louis, M.J. v d Wiel, E.C.I. Turcu, G.J. Tallents and D. Batani, *J. X-ray Sci. Technol.* **3** (1992) 133-151
13. D.M. Simanovskii, A.N. Gladshikh, L.A. Shmaenok, and S.V. Bobashev, *Phys. Rev. Lett.* **77** (1996) 849-852
14. N.M. Ceglio and A.M. Hawryluk, *J. X-ray Sci. Technol.* **3** (1992) 194-203
15. J.J.M. Braat, F. Bijkerk, and H.G.C. Werij, "Throughput of EUV lithographic systems", Confidential report (FOM-Institute for Plasma Physics Rijnhuizen, 23 October 1996)
16. D.K.G. de Boer, *Phys. Rev. B* **44** (1991) 498-511
17. J.H. Underwood and E.M. Gullikson, *Proc. 3rd International Conference Physics of X-ray multilayer structures* (1996) **4.3**
18. E. Spiller and A. E. Rosenbluth, *Proc. SPIE* **563** (1985) 221
19. A.D. Akhsakhalyan, A.A. Fraerman, N.I. Polushkin, Y.Y. Platonov and N.N. Salashchenko, *Thin Solid Films* **203** (1991) 317-326



20. J.P. Chauvineau, J. Corno, D. Decanini, L. Nevot and B. Pardo, Proc. SPIE **563** (1985) 245-252, F. Bridou, and B. Pardot, J. X-ray Sci. Technol. **4** (1994) 200-216, F. Bridou and B. Pardo, J. Phys III France **4** (1994) 1523-1531
21. D.E. Savage, J. Kleiner, N Schimke, Y.-H Phang, T. Jankowski, J. Jacobs, R. Kariotis and M.G. Lagally, J. Appl. Phys. **69** (1991) 1411-1424
22. D.G. Stearns, J. Appl. Phys. **71** (1992) 4288-4298
23. E. Spiller, D. Stearns, M. Kumrey, J. Appl. Phys. **74** (1993) 107-118
24. R. Schlattmann, Thesis Vrije Universiteit, Amsterdam (1995)
25. T.W. Barbee, Jr., Opt. Eng. **25** (1986) 893-915
26. E. Spiller, Proc. SPIE **563** (1985) 367-375
27. D.G. Stearns, R.S. Rosen, and S.P. Vernon, Appl. Opt. **32** (1993) 6952-6960
28. E. Louis, H.-J. Voorma, N.B. Koster, F. Bijkerk, Yu. Ya. Platonov, S. Yu. Zuev, S.S. Andreev, E.A. Shamov, and N.N. Salashchenko, Microelectron. Eng. **27** (1995) 235-238
29. D.L. Windt, W.K. Waskiewicz, G.D. Kubiak, T.W. Barbee Jr. and R.N. Watts, Proc. SPIE **1343** (1990) 274-279
30. J. Verhoeven, E. Puik and M.J. v d Wiel., Vacuum **39** (1989) 711-716
31. M. Niibe, M. Hayashida, T. Iizuka, A. Miyake, Y. Watanabe, R. Takahsi, Y. Fukuda, Proc. SPIE **1343** (1990) 2-12
32. S.P. Vernon, D.G. Stearns, and R.S. Rosen, ppl. Opt. **32** (1993) 6969-6974
33. A. Kloidt, H.J. Stock, U. Kleineberg, T.Dohring, M. Propper, K. Nolting, B. Heidemann, T. Tappe, B. Schiedeskamp and U. Heinzmann, Proc. SPIE **1743** (1990) 593-600
34. E. Louis, H.-J. Voorma, N.B. Koster, L. Shmaenok, F. Bijkerk, R. Schlattmann, J. Verhoeven, Yu. Ya. Platonov, G.E. van Dorssen and H. Padmore, Microelectron. Eng. **23** (1994) 215-218
35. H.-J. Voorma, E. Louis, F. Bijkerk, and M.J. van der Wiel, MRS sym. proc. **382** (1995) 375-380
36. J. Verhoeven, Lu. Chunguang, E.J. Puik, M.J. van der Wiel, Appl. Surf. Sci. **55** (1992) 97-103
37. R. Schlattmann, C. Lu, J Verhoeven, E.J. Puik, and M.J. van der Wiel, Physics of X-ray Multilayer Structures, OSA Technical Digest Series, **7** (1992) PD6-1
38. W.K Waskiewicz, D.L. Windt, J.E. Bjorkholm, L. Eichner, R.R. Freeman, T.E. Jewellm W.M. Mansfield, A.A. MacDowell, L.H. Szeto, D.M. Tennant, D.L. White, and O.R. Wood II, OSA Proc. Soft X-ray Projection Lithography, **12** (1991) 97-100
39. E. Louis, E. Spiller, S. Abdali, F.E. Christensen, H.-J. Voorma, N.B. Koster, P.K. Frederiksen, C.Tarrio, E.M. Gulikson, and F. Bijkerk, Proc. SPIE **2515** (1995) 194-203
40. S.P. Vernon, P.A. Kearney, F.W. Weber, and D.R. Kania, Proc. Physics of X-ray Multilayer Structures (1996) 8.3
41. T.D. Nguyen and J.H. Underwood, Mat. Res. Soc. Symp. Proc. **382** (1995) 297-302
42. A.J. Shell-Sorokin and R.M. Tromp, Phys. Rev. Lett. **64** (1990) 1039-1042
43. F. Zernike, OSA Proc. EUV Lithography, **4** (1996) 94-97
44. J.M. Elson and J.M. Bennet, J. Opt. Soc. Am. A **69** (1979) 31-47
45. M. Born and E. Wolf, *Principles of Optics*, Pergamon Press, Oxford, 1959
46. Z. Tan, A.A. MacDowell, B. La Fontaine, J. Russo, J.E. Bjorkholm, D. Tennant, D. Taylor, M. Himel, O.R. Wood II, W.K. Waskiewicz, D.L. Windt, D. White, S. Spector, A.K. Ray-Chaudhuri, and R.H. Stulen, OSA Proc. on EUV Lithography **23** (1994) 151-160
47. K.A. Goldberg, R. Beguiristain, J. Bokor, H. Medeck, K. Jackson, and D.T. Attwood, OSA Proc. on EUV Lithography **23** (1994) 134-141
48. G.E. Sommargren and L.G. Seppala, Appl. Opt. **32** (1993) 6938-6943
49. S. Vernon, OSA Proc. EUV Lithography **4** (1996) 44-48

50. K.B. Nguyen, D.T. Attwood, T. Mizota, T. Haga and H. Kinoshita, OSA Proc. EUV Lithography **23** (1994) 193-203
51. J.H. Underwood, E.M. Gullikson, and K. Nguyen, Appl. Opt. **32** (1993) 6985-6990
52. D.G. Stearns, K.M. Skulina, M. Wall, C.S. Alford, R.M. Bionta, D.M. Makowiecke, E.M. Gulikson, R. Soufli, J.B. Kortright and J.H. Underwood, MRS symp. Proc. **382** (1995) 329-337
53. E. Spiller, Appl. Phys. Lett. **54** (1989) 2293-2295
54. E. Louis, and E. Puik unpublished
55. J. B. Kortright, T.D. Nguyen, I.M. Tidswell, C.A. Lucas, Physics of X-ray Multilayer Structures, OSA Technical Digest Series, **7** (1992) 102-104
56. A.V. Vinogradov, I.A. Artyukov, S.S. Borisova, N.N. Zorev, I.V. Kozhevnikov, I.F. Mikhailov, S.I. Sagitov and A.I. Fedorenko, Proc. SPIE **1140** (1989) 490-499

All multilayer mirrors discussed in this thesis have been prepared with electron-beam evaporation in the set-up at the POM-Institute for Plasma Physics Rijnhuizen. The special features of the set-up include the suitability to deposit large multilayer mirrors on curved substrates, the presence of an in-situ soft x-ray reflectometer, and auxiliary equipment to apply ion-bombardment and substrate heating.

The deposition system consists of two high-vacuum chambers, as is displayed in Figure 2. The lower chamber is the evaporation chamber, which contains the electron gun (maximum power 6 kW) and the materials to be evaporated. The pressure in the lower system during operation is  $1 \times 10^{-7}$  mbar. The upper chamber contains a substrate holder, an ion gun, and the in-situ reflectometer and operates at UVV conditions ( $5 \times 10^{-9}$  mbar). In between them



Figure 2. Front and side view of the deposition facility, in which in a) the situation during deposition is drawn and in b) the situation during ion bombardment.



1991; *J. Microsc.* **163**, 117–122.

20. G. Binnig, H. Rohrer, C. Gerber and E. Schweizer, *Phys. Rev. Lett.* **59** (1987) 5569–5571.

21. G. Binnig, H. Rohrer, C. Gerber and E. Schweizer, *Phys. Rev. Lett.* **59** (1987) 5572–5574.

22. G. Binnig, H. Rohrer, C. Gerber and E. Schweizer, *Phys. Rev. Lett.* **59** (1987) 5575–5577.

23. G. Binnig, H. Rohrer, C. Gerber and E. Schweizer, *Phys. Rev. Lett.* **59** (1987) 5578–5580.

24. G. Binnig, H. Rohrer, C. Gerber and E. Schweizer, *Phys. Rev. Lett.* **59** (1987) 5581–5583.

25. G. Binnig, H. Rohrer, C. Gerber and E. Schweizer, *Phys. Rev. Lett.* **59** (1987) 5584–5586.

26. G. Binnig, H. Rohrer, C. Gerber and E. Schweizer, *Phys. Rev. Lett.* **59** (1987) 5587–5589.

27. G. Binnig, H. Rohrer, C. Gerber and E. Schweizer, *Phys. Rev. Lett.* **59** (1987) 5590–5592.

28. G. Binnig, H. Rohrer, C. Gerber and E. Schweizer, *Phys. Rev. Lett.* **59** (1987) 5593–5595.

29. G. Binnig, H. Rohrer, C. Gerber and E. Schweizer, *Phys. Rev. Lett.* **59** (1987) 5596–5598.

30. G. Binnig, H. Rohrer, C. Gerber and E. Schweizer, *Phys. Rev. Lett.* **59** (1987) 5599–5601.

31. G. Binnig, H. Rohrer, C. Gerber and E. Schweizer, *Phys. Rev. Lett.* **59** (1987) 5602–5604.

32. G. Binnig, H. Rohrer, C. Gerber and E. Schweizer, *Phys. Rev. Lett.* **59** (1987) 5605–5607.

33. G. Binnig, H. Rohrer, C. Gerber and E. Schweizer, *Phys. Rev. Lett.* **59** (1987) 5608–5610.

34. G. Binnig, H. Rohrer, C. Gerber and E. Schweizer, *Phys. Rev. Lett.* **59** (1987) 5611–5613.

35. G. Binnig, H. Rohrer, C. Gerber and E. Schweizer, *Phys. Rev. Lett.* **59** (1987) 5614–5616.

36. G. Binnig, H. Rohrer, C. Gerber and E. Schweizer, *Phys. Rev. Lett.* **59** (1987) 5617–5619.

37. G. Binnig, H. Rohrer, C. Gerber and E. Schweizer, *Phys. Rev. Lett.* **59** (1987) 5620–5622.

38. G. Binnig, H. Rohrer, C. Gerber and E. Schweizer, *Phys. Rev. Lett.* **59** (1987) 5623–5625.

39. G. Binnig, H. Rohrer, C. Gerber and E. Schweizer, *Phys. Rev. Lett.* **59** (1987) 5626–5628.

40. G. Binnig, H. Rohrer, C. Gerber and E. Schweizer, *Phys. Rev. Lett.* **59** (1987) 5629–5631.

41. T.D. Nguyen and J.H. Underwood, *Mis. Res. Soc. Symp. Proc.* **38D** (1995) 297–302.

42. A.J. Shefi-Sherkan and R.M. Tromp, *Phys. Rev. Lett.* **64** (1990) 1039–1042.

43. F. Zanetti, *OSA Proc. EIV Librography*, **4** (1996) 94–97.

44. J.M. Blain and J.M. Beatty, *J. Opt. Soc. Am. A* **69** (1979) 31–47.

45. M. Born and E. Wolf, *Principles of Optics*, Pergamon Press, Oxford, 1959.

46. Z. Liu, A.Y. MacDowell, B. La Fontaine, J. Rames, J.E. Bjorkholm, D. Tomack, D. Vignesi, G. Wong, O.B. Wood II, W.K. Waskewicz, D.L. White, D. White, S. Spruce, A.K. Ray-Chaudhury, G. Binnig, N.A. Gadberg, R. Bergmann, J. Bokor, H. Mauch, K. Jackson, and D.T. Atkinson, *Phys. Rev. Lett.* **75** (1995) 134–137.

47. N.A. Gadberg, R. Bergmann, J. Bokor, H. Mauch, K. Jackson, and D.T. Atkinson, *Phys. Rev. Lett.* **75** (1995) 134–137.

48. G.E. Rammussen and L.D. English, *Appl. Opt.* **23** (1993) 6928–6943.

49. S. Venner, *OSA Proc. EIV Librography*, **4** (1996) 44–48.

# 1b

## Coating facility

All multilayer mirrors discussed in this thesis have been produced with electron-beam evaporation in the set-up at the FOM-Institute for Plasma Physics Rijnhuizen. The special features of the set-up include the suitability to deposit large multilayer mirrors on curved substrates, the presence of an in-situ soft x-ray reflectometer, and auxiliary equipment to apply ion-bombardment and substrate heating.

The deposition system consists of two high-vacuum chambers, as is displayed in Figure 2. The lower chamber is the evaporation chamber, which contains the electron gun (maximum power 6 kW) and the materials to be evaporated. The pressure in the lower system during operation is  $1 \times 10^{-7}$  mbar. The upper chamber contains a substrate holder, an ion gun, and the in-situ reflectometer and operates at UHV conditions ( $5 \times 10^{-9}$  mbar). In between these

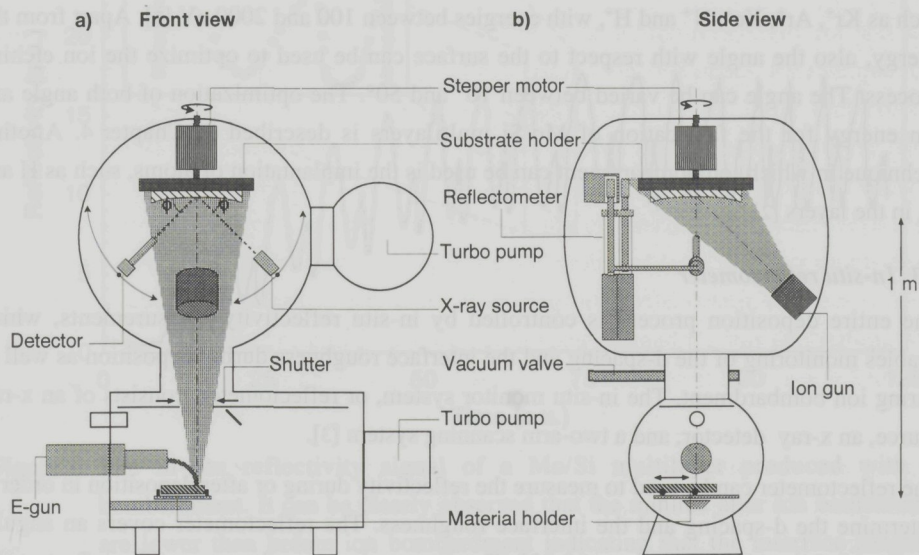


Figure 2 Front and side view of the deposition facility, in which in a) the situation during deposition is drawn and in b) the situation during ion bombardment.

chambers a shutter is positioned in order to block the deposition beam during start-up and stabilization of the evaporation process. The operational pressure is obtained after 6 to 10 hours heating at 120 °C. This is primarily needed to reduce the residual water pressure, which can cause contamination of the layers during deposition.

### **1.1 Substrate holder**

A special substrate holder in the upper system allows rotation of the substrate or heating. The increased substrate temperature is used to decrease the interface roughness during deposition. This technique is investigated in detail in Chapter 4. The substrate holder can also be used to study thermal properties of completed multilayers in vacuum. The holder is heated with quartz lamps and the temperature is measured in the holder with a Chromel-Alumel thermocouple with an accuracy of  $\pm 2$  °C.

When the substrate holder is not heated, it can be rotated with a maximum speed of 60 rpm, which improves the homogeneity of the d-spacing. The overall geometry allows deposition on large mirrors with diameters up to 400 mm; e.g. for space research and EUVL. The inhomogeneity of the deposition process, caused by alignment of the deposition and ion beam or the beam profiles, over the surface can be corrected with masks in the deposition beam.

### **1.2 Ion gun**

The technique of using ion bombardment to reduce the interface roughness of the multilayers is discussed in detail in Chapter 5. Ion bombardment can be performed using different ions, such as Kr<sup>+</sup>, Ar<sup>+</sup>, Xe<sup>+</sup>, N<sup>+</sup> and H<sup>+</sup>, with energies between 100 and 2000 eV [1]. Apart from the energy, also the angle with respect to the surface can be used to optimize the ion etching process. The angle can be varied between 10° and 50°. The optimization of both angle and ion energy for the fabrication of Mo/Si multilayers is described in Chapter 4. Another technique in which ion bombardment can be used is the implantation of atoms, such as H and N, in the layers [2].

### **1.3 In-situ reflectometer**

The entire deposition process is controlled by in-situ reflectivity measurements, which enables monitoring of the d-spacing and the interface roughness during deposition as well as during ion bombardment. The in-situ monitor system, or reflectometer, consists of an x-ray source, an x-ray detector, and a two-arm scanning system [3].

The reflectometer can be used to measure the reflectivity during or after deposition in order to determine the d-spacing and the interface roughness. The reflectometer covers an angular range of 0-65° with an accuracy of 0.02°. The distance between the parts of the reflectometer and the centre of rotation on the sample holder is 300 mm, which leaves sufficient space for large multilayer mirrors.



### 1.3.1 X-ray source and detector

The x-ray source that is used in our deposition system is a conventional electron impact x-ray source. Its BN anode provides B-K (6.67 nm) and N-K (3.16 nm) radiation. Also other anode materials can be used, such as C. Calculations and experiments show that for the monitoring of the deposition process of Mo/Si multilayers, the N-K emission line is preferred, because it results in a more optimal thickness ratio compared to other emission lines. Since, the intensities of both the N-K and B-K lines from this type of x-ray source are almost equal, emission of the B-K line has to be suppressed using a 600 nm thick Ti filter. It has a transmission for the N-K line of 31% and only 1% for the B-K line. The reflectivity of the sample is measured with a channeltron detector, which is positioned directly behind the Ti filter.

### 1.3.2 In-situ signal

Two of the main multilayer parameters, the interface roughness and the d-spacing, can be monitored during deposition with the in-situ reflectivity signal. The in-situ reflectivity signal reaches a maximum when the high-Z material, i.e. Mo, has an optical thickness of  $\lambda/4\sin\theta$ , and reaches a minimum when the low-Z material, i.e. Si, has a corresponding optical

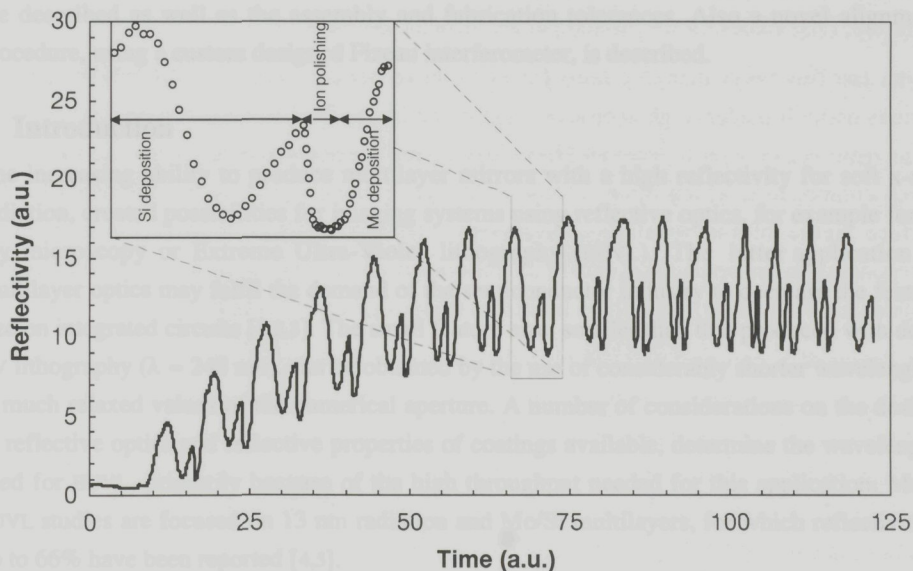


Figure 3 The in-situ reflectivity signal of a Mo/Si multilayer produced with ion bombardment. It can be clearly observed that the minima after ion bombardment are lower than before ion bombardment indicating that the interface roughness reduces. The inset shows the in-situ reflectivity during the deposition of one period. The initial increase in the inset of the reflectivity during the deposition of the Si layer is due to a optical phase effect.

thickness. An example of an in-situ reflectivity signal of a Mo/Si multilayer is displayed in Figure 3. The amplitude is defined as the increase during deposition of the high-Z material, normalized to the reflectivity before the deposition of that layer. The amplitude is mainly determined by the interface roughness of the layer deposited. The maximum of the in-situ signal during one period is the value obtained after deposition of the high-Z material. The maximum is determined by the total quality of the multilayer. The d-spacing is determined by the angle and the wavelength of the x-ray source, neglecting any layer thickness errors.

## 2. References

1. E. Puik, Thesis Vrije Universiteit, Amsterdam (1990)
2. R. Schlatmann, A. Keppel, Y. Xue, and J. Verhoeven, Appl. Phys. Lett. **63** (1993) 3297
3. N.B. Koster, H.-J. Voorma, E. Louis, F. Bijkerk, NEVAC nov/dec (1996) in print (in Dutch)

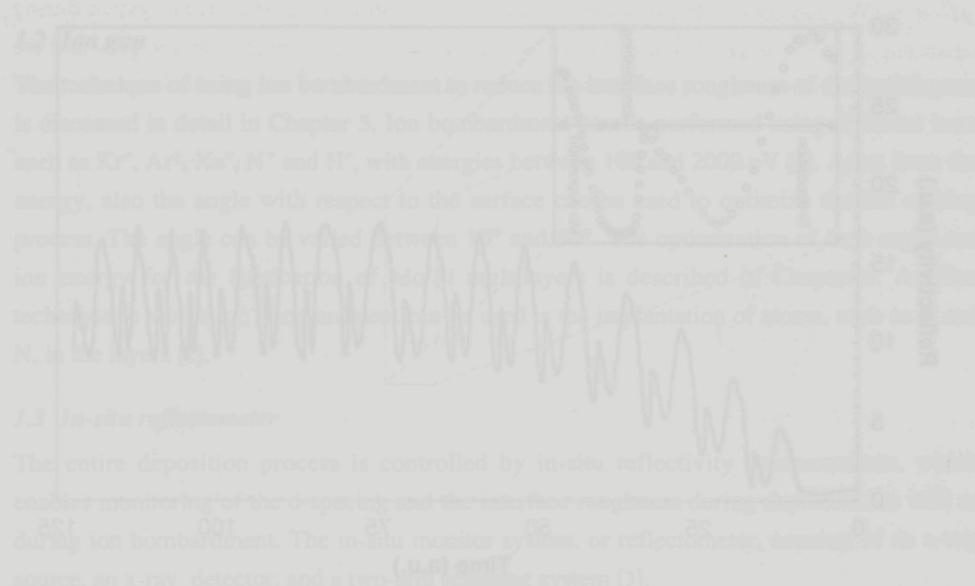


Figure 3. In-situ reflectivity signal of a Mo/Si multilayer produced with ion bombardment. The signal shows a series of sharp peaks and troughs, characteristic of a multilayer structure. The peaks occur at approximately 10, 20, 30, 40, 50, 60, 70, 80, 90, 100, and 110 seconds. The troughs occur at approximately 5, 15, 25, 35, 45, 55, 65, 75, 85, 95, and 105 seconds. The overall trend shows a gradual increase in the baseline reflectivity over time, with the peaks becoming more pronounced as the deposition progresses.

## Design, construction and alignment of a compact four-mirror projection system for 13 nm radiation

### 1. Abstract

In order to allow assessment of different research aspects of Extreme Ultra-Violet Lithography (EUVL), a compact projection system has been designed, constructed and aligned. The design consists of a two-mirror imaging system and a spherical reflection mask and illuminator. The system, designed for a wavelength of 13 nm, has an intrinsic resolution of 76 nm over a circular image field with a diameter of 4 mm. The design and construction are described as well as the assembly and fabrication tolerances. Also a novel alignment procedure, using a custom designed Fizeau interferometer, is described.

### 2. Introduction

The increasing ability to produce multilayer mirrors with a high reflectivity for soft x-ray radiation, created possibilities for imaging systems using reflective optics, for example for x-ray microscopy or Extreme Ultra-Violet lithography (EUVL). The latter application of multilayer optics may fulfil the demand of the semiconductor industry to decrease the feature size on integrated circuits [1,2,3]. The small feature size, smaller than that produced with deep UV lithography ( $\lambda = 248$  nm), can be obtained by the use of considerably shorter wavelengths at much relaxed values of the numerical aperture. A number of considerations on the design of reflective optics and reflective properties of coatings available, determine the wavelength used for EUVL, primarily because of the high throughput needed for this application. Most EUVL studies are focused on 13 nm radiation and Mo/Si multilayers, for which reflectivities up to 66% have been reported [4,5].

Requirements for EUVL systems, formulated in the National Technology Roadmap for Semiconductors [6], include a resolution of less than 100 nm over a large flat image field, a depth of focus (DOF) of at least 1.0  $\mu\text{m}$ , and a high intensity at the image field (5-30 mW/cm<sup>2</sup>). Deep UV lithography at 193 nm, is expected to yield feature sizes down to 130 nm [7]. Therefore, the starting point for EUVL is generally considered to be at around



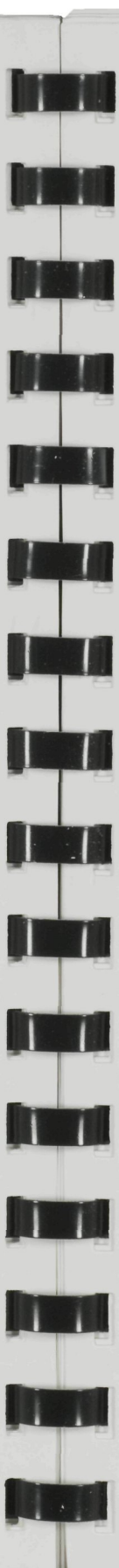
100 nm. Systems designed recently are expected to use a step-and-scan mechanism to obtain a large image field. Scan field sizes up to  $1 \times 25$  mm have been reported [8]. The required DOF is mainly determined by the topology of the resist on the structured wafer and the wafer flatness. The DOF is required to be at least  $1 \mu\text{m}$ , which enables imaging without the use of additional planarization layers.

In contrast to transmission masks, reflection masks possess high stability, which enables an improved positioning and handling accuracy. We have shown that reflection masks can be produced successfully on both flat and curved multilayer substrates [9]. In practice, a modified version of e-beam pattern generators is required to write curved masks, which may turn out to be impractical for serial mask production.

Finally, throughput is a critical issue, although more important for an industrial stepper than for the feasibility system discussed here. It is difficult to estimate future production rates of EUVL systems, but it is unlikely that the wafer throughput will decline compared to the current production rate in optical lithography (about sixty 6" wafer exposures per hour). The throughput of an EUVL system is dependent on the so-called front-end of the system (EUV source), the optical system (mirror reflectivity, the geometry of the imaging and illuminating optics, and filters), and resist sensitivity. Many of these subjects are still under study, and therefore, final values for the throughput are difficult to assess.

In the last few years many systems for EUVL have been proposed [8,10,11,12], which use various normal-incidence geometries to realize the image field size, resolution, and depth of focus required. In order to meet all EUVL imaging requirements, these systems can have up to seven components, which often include aspherical elements [8]. The requirements for the surface figure of the substrates, alignment, and mounting scale with the number of components in an optical system. Practical construction of two- or three-mirror imaging systems for EUVL is performed by a limited number of groups [13,14,15].

We designed a compact and simplified two-mirror imaging system [16] to be able to investigate various aspects of the feasibility of EUVL, such as the alignment, the throughput, and the stability of the optical system. Also the production and optimization of multilayer coatings on large curved substrates, including the lateral control and the matching of the spacings of all components are investigated [4]. A fabrication procedure for reflection masks has been developed [9], and has been applied successfully on both flat and curved multilayer mask substrates. Experience has been obtained in the implementation of a laser plasma source, the suppression of contamination of the optical elements by residual debris from the laser plasma, and filtering of the broadband XUV and the scattered laser light. Some aspects are still under study, such as the image formation in an EUV resist, including the effect of scattering from the multilayers on the resolution. So far, 200 nm structures have been observed.



The four-mirror system (including mask and illuminator) selected employs only spherical components of which the design, construction and alignment are described in this chapter. This type of optics has advantages with respect to e.g. the alignment, the requirements for the surface figure of the substrates, and the throughput. It is noted that similar systems can also be used as imaging systems for x-ray microscopy or as a focusing unit for other applications, such as x-ray photo-electron spectroscopy (XPS) or x-ray fluorescence (XRF).

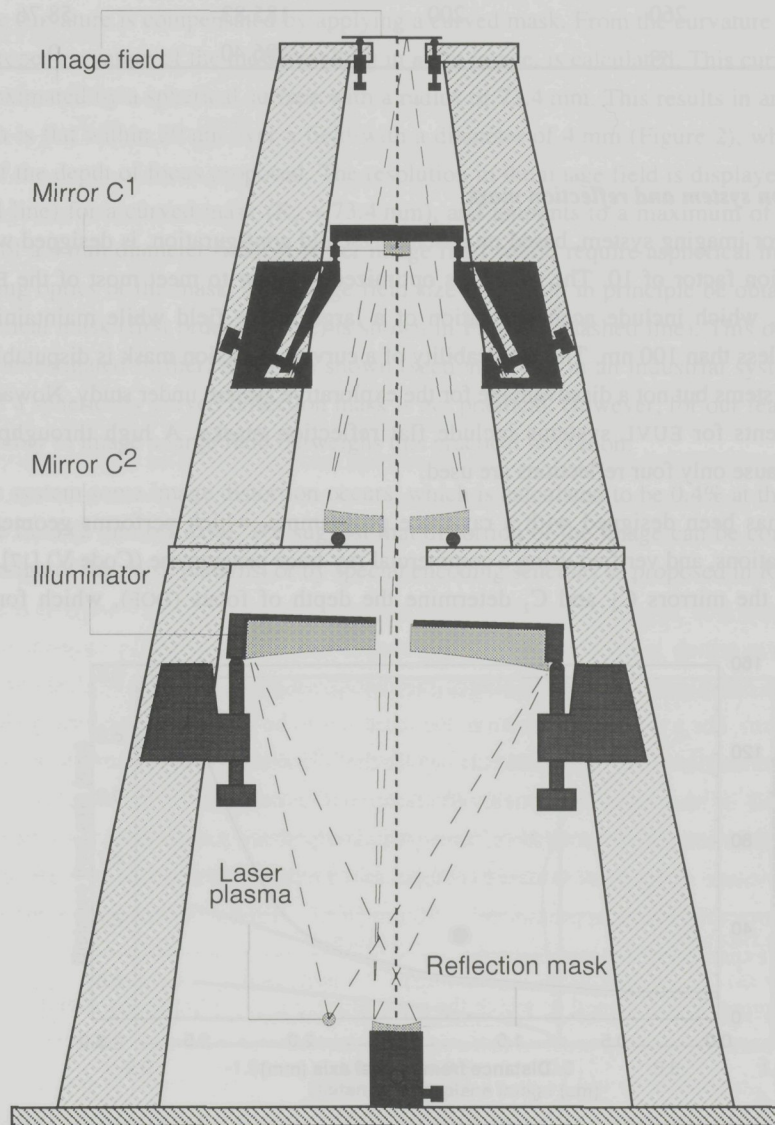


Figure 1: Schematic layout of the optical system. The mounting consists of three vertical stands (at  $120^\circ$  angle with respect to each other) of which two are shown.



Table I: Data of the optical system

mirror	radius of curvature (mm)	diameter (mm)	distance to $C_2$ (mm)	tilt to optical axis ( $\mu\text{rad}$ )
$C_1$	100	22	216.07	0
$C_2$	316	120	0.00	0
Mask	73.4	40	482.53	0
Illuminator	260	200	185.83	58.76
Wafer	$\infty$	10	396.40	0

### 3. Design

#### 3.1 Projection system and reflection mask

The two-mirror imaging system, based on a Schwarzschild configuration, is designed with a demagnification factor of 10. The system is optimized in order to meet most of the EUVL requirements, which include accommodation of a large image field while maintaining a resolution of less than 100 nm. The applicability of a curved reflection mask is disputable for production systems but not a disadvantage for the explorative system under study. Nowadays, the requirements for EUVL systems include flat reflection masks. A high throughput is obtained, because only four reflections are used.

The system has been designed with a ray-trace programme, which performs geometrical optical calculations, and verified using a commercial ray-trace programme (Code V) [17]. The diameters of the mirrors  $C_1$  and  $C_2$  determine the depth of focus (DOF), which for this

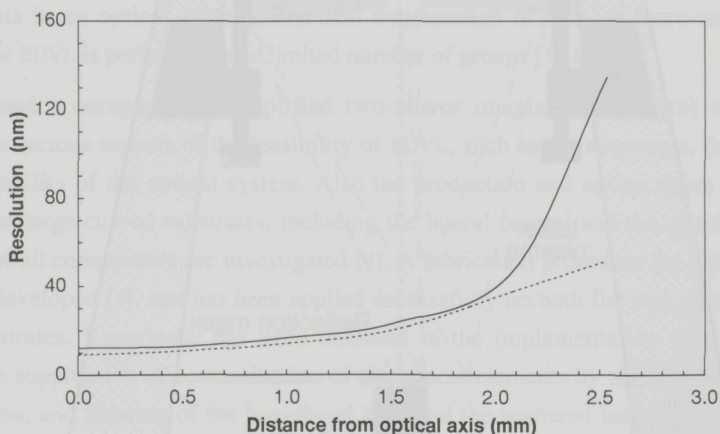


Figure 2: Curvature of the image field resulting from a flat mask ( $R_3 = \infty$ , represented by the solid line) and from a mask with a radius of curvature of 73.4 mm (dashed line).



configuration is selected to be  $\pm 0.5 \mu\text{m}$ . The complete design procedure results in a nearly concentric two-mirror system with a central obstruction,  $\varepsilon = 0.3$ , as is shown in Figure 1. The dimensions of the system are listed in Table I. The mirrors  $C_1$  and  $C_2$  are positioned  $70 \mu\text{m}$  off the concentric position in order to obtain a maximal image field and a resolution of below  $100 \text{ nm}$ .

Imaging a flat object (mask radius  $R_3 = \infty$ ) with this two-mirror system results in a curved image field, which is shown in Figure 2 as a solid line. In order to obtain a flat image, the image curvature is compensated by applying a curved mask. From the curvature of the image, the proper curvature of the mask resulting in a flat image, is calculated. This curvature is then approximated by a spherical surface with a radius of  $73.4 \text{ mm}$ . This results in an image field, which is flat within  $50 \text{ nm}$  over a field with a diameter of  $4 \text{ mm}$  (Figure 2), which is within  $5\%$  of the depth of focus proposed. The resolution in the image field is displayed in Figure 3 (solid line) for a curved mask ( $R_3 = 73.4 \text{ mm}$ ), and amounts to a maximum of  $50 \text{ nm}$  at the edge of a  $4 \text{ mm}$  diameter field. A larger image field would require aspherical mirrors for the imaging optics or the mask. The image field size that could in principle be obtained with an aspherical mask (first order asphere) is shown in Figure 3 (dashed line). This option has not been investigated further. It will be shown (section 4) that in an industrial system, even the use of a spherically curved reflection mask is not practical. However, for our feasibility study the ability to image a large field outweighs this practical limitation.

In the system some image distortion occurs, which is calculated to be  $0.4\%$  at the edge of the image field ( $2 \text{ mm}$  off axis). We suggest that distortion of the image can be compensated in the design of the mask patterns, or by special encoding schemes as proposed in Ref. [18].

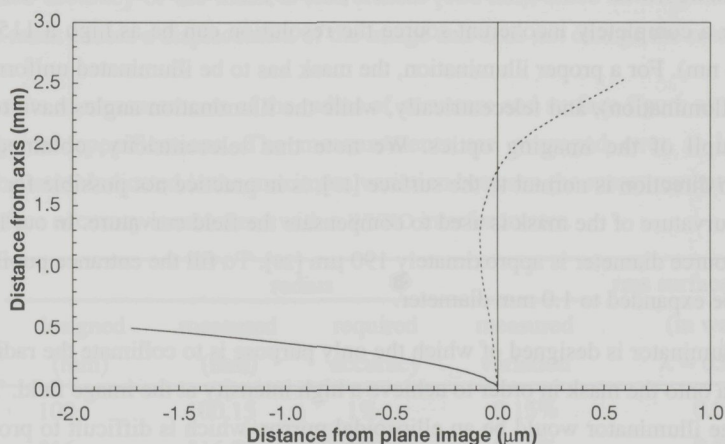


Figure 3: Geometrical resolution at the image field versus distance from the optical axis. The solid line corresponds to a spherical mask, the dashed line to an aspherical mask.

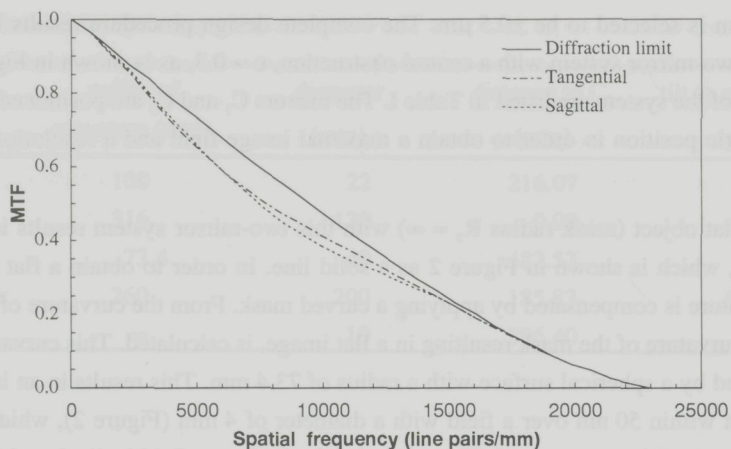


Figure 4: Modulation transfer function for  $\lambda = 13$  nm at 2 mm off axis in the image field.

The ray-trace programme is used to minimize optical aberrations like coma, spherical aberration, astigmatism, image distortion and field curvature [17]. It is found that the geometrical resolution is limited by coma to 50 nm. In order to determine the resolution of the system more accurately, the 13 nm wavelength is taken into account. For this purpose, the modulation transfer function (MTF) is calculated for 13 nm radiation (Figure 4). The MTF exceeds 0.5 at 6620 line pairs per mm, which corresponds to a resolution of 76 nm provided that fabrication and assembly tolerances are met.

### 3.2 Illuminator

If a laser plasma EUV source is used, the resolution improves, since the MTF analysis assumes an illumination which is coherent rather than partially coherent, as in the case of a laser-plasma. For a completely incoherent source the resolution can be as high as 1150 line pairs per mm (43 nm). For a proper illumination, the mask has to be illuminated uniformly (Köhler or critical illumination), and telecentrically, while the illumination angles have to match the entrance pupil of the imaging optics. We note that telecentricity, obtained when the illumination direction is normal to the surface [19], is in practice not possible for a system in which the curvature of the mask is used to compensate the field curvature. In our laser plasma set-up the source diameter is approximately 190  $\mu\text{m}$  [20]. To fill the entrance pupil, the source size could be expanded to 1.0 mm diameter.

A simple illuminator is designed of which the only purpose is to collimate the radiation of the laser plasma onto the mask in order to achieve a high intensity at the image field. The optimal design of the illuminator would be an ellipsoidal mirror, which is difficult to produce and to coat with a multilayer structure. Therefore, a spherical figure is selected for the illuminator with a diameter of 200 mm and a radius of curvature of 260 mm. The size of the illuminator



enables a large distance between the illuminator and the laser-plasma source, while a large collection angle for the radiation from the source is maintained. The distance between the source and the illuminator facilitates protection of the illuminator from residual debris from the laser plasma by using a buffer gas [21]. However, the disadvantage of this illumination scheme is the astigmatism present in the illumination. This is considered a minor disadvantage when small fields are imaged. An image field with a 4 mm diameter requires a different illumination scheme, for instance as proposed in Refs 22 and 23.

## 4. Tolerances

### 4.1 Surface figure

Concerning the surface figure of the substrates, requirements apply to two issues: the actual radius of curvature and the local deviation from this ideal curvature, referred to as surface accuracy. The actual radius of curvature is determined by measuring the interference fringes between the substrate and a reference substrate. The results of these measurements are listed in Table II. It is concluded that the substrates of mirror  $C_1$ ,  $C_2$  and the illuminator meet the requirements. The radii of curvature of the mask substrates are too large, indicating that the calculated image field size will not be obtained.

According to the Strehl definition, the requirement for the maximum wavefront error for the entire system is  $\lambda/14$  [24]. This indicates that the requirements for the individual substrates are determined from the rms wavefront error caused by the system. This wavefront error amounts to  $0.048\lambda$ , and the corresponding accuracy of each surface is calculated to be  $0.037\lambda$  at  $\lambda = 13$  nm. This indicates that for the characterization of the substrates of mirror  $C_1$  and  $C_2$  a resolution of approximately  $\lambda/500$  is required when using visible light. It is noted that the required surface accuracy of the mask is less critical (100 nm), since an irregularity in the surface of the mask causes a displacement of the image and does not change the resolution.

Table II: Results of measurements of the radius of curvature and surface figure as well as the required specifications. The measurements are averaged over at least three substrates. Indicated is the maximum variation between the measurements. The rms surface accuracy is measured with a WYKO interferometer.

	radius				rms surface accuracy (in waves) $\lambda = 632$ nm
	designed (mm)	measured (mm)	required accuracy	measured variation	
$C_1$	100	100.15	1%	0.15%	0.015
$C_2$	316	316.78	1%	0.10%	0.017
Mask	73.4	73.93	0.02%	0.06%	-
Illuminator	260	258.19	5%	0.06%	-



All substrates of the imaging optics are tested using a WYKO 600 interferometer. The results of these measurements are listed in Table II and show that the rms surface accuracy of the substrates is between 0.01 and 0.02 waves (wv) at  $\lambda = 632$  nm, which is limited by the reference optics in the interferometer used. The actual surface accuracy of the substrates might therefore be better than the values found here. In order to test the mirror substrates including multilayer coatings accurately, the substrates have to be tested using an EUV interferometer or visible light interferometer with a resolution of at least  $\lambda/500$  [25]. Systems for EUV interferometry have been constructed and are being tested [26, 27].

#### 4.2 Surface roughness

The surface roughness is divided into two spatial frequency ranges, namely the mid frequency range ( $10^{-6}$  -  $10^{-4}$  nm $^{-1}$ ), which results in scattering inside the numerical aperture of the optical system, and the high frequency range ( $10^{-4}$  -  $10^{-2}$  nm $^{-1}$ ) which gives rise to scattering outside the numerical aperture. The roughness in the mid frequency range reduces the contrast in the image field and, by consequence, the resolution. The value of the specular reflectivity is determined by losses due to scattering in both the mid and high frequency range.

One method to investigate the roughness of a substrate is to measure the near-normal-incidence reflectivity of a multilayer deposited on that substrate and to compare these values with the reflectivity of a multilayer on a reference sample (e.g. a Si(100) wafer), produced in the same deposition run. This test is performed on one of the curved substrates (mirror  $C_1$ ). The fabrication and the near normal incidence reflectivity measurements of these samples are described in detail in elsewhere [4]. The values of the near normal incidence reflectivity at different positions of the substrate are shown in Figure 5. Analysis of these measurements

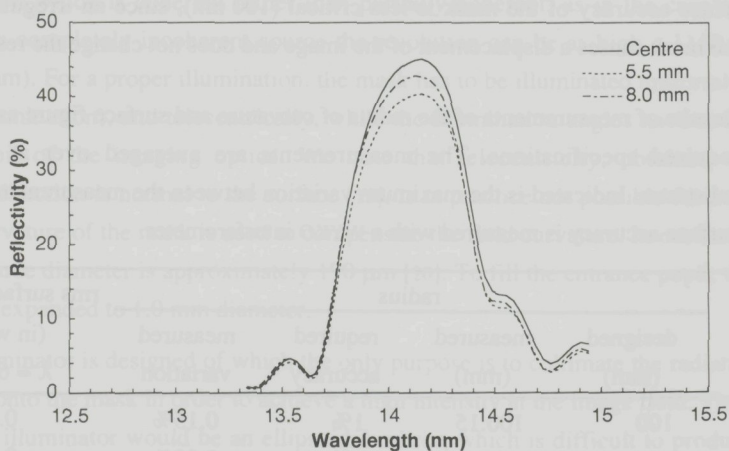


Figure 5: Near-normal reflectivity of a 40-period Mo/Si multilayer structure measured at  $87^\circ$  with respect to the surface on different positions on mirror  $C_1$ .

shows that the rms roughness is 1.2 nm at the centre and 1.5 nm at 5.5 mm off centre. Apparently, the deviations in the reflectivity are caused by local differences in the substrate roughness. The quartz substrate shows a higher roughness (between 1.2 nm and 1.5 nm) than the Si wafer (0.3 nm), which is believed to be the reason for the overall lower reflectivity (48% versus 63% for the Si wafer [4])

### 4.3 Alignment tolerances

The tolerances are calculated in two steps. Firstly, the maximum displacement of each element is calculated separately, while keeping the other elements positioned perfectly. The acceptable limit for misalignment of each component is then determined while setting the resolution at 100 nm within the DOF at the image plane. Secondly, the final tolerances of each component are chosen to be 10% of the maximum displacement determined this way, because all optical elements could be misaligned simultaneously. This results in more stringent requirements for the mounting, but alignment is not found to be impractical. The type of mounting consists of mechanical systems, because for these requirements piezo or feedback systems are not needed.

The tilt of  $C_1$  and  $C_2$  is critical in this system. The tolerances for  $C_1$  and  $C_2$  are found to be 1.5 and 0.5  $\mu\text{rad}$ , respectively. A tilt of the mask of 8.5  $\mu\text{rad}$  is acceptable, since an 85  $\mu\text{rad}$  tilt of the mask in an otherwise perfectly aligned system still results in an image which is within the DOF. A change in the object distance, i.e. the distance between the mask and mirror  $C_1$ , changes the demagnification factor, but has a negligible effect on the resolution. The change of the demagnification factor (0.15%/mm) of this system determines the position accuracy of the mask. It is calculated that the positioning accuracy of the mask along the optical axis is  $\pm 1.3 \mu\text{m}$  in order to meet the overlay accuracy of 30 nm [6]. The distance between mirrors  $C_1$  and  $C_2$  is not critical, and may vary 1.0  $\mu\text{m}$  without changing the resolution in the image field. The tolerances for the inter-component distances ( $Z$ ), the tilt of the mirrors ( $\theta$ ) and the position of the mirrors on the optical axis are calculated and listed in Table III.

Table III: Tolerances of the optical system (resolution of 100 nm) in which R represents maximum lateral deviation in the horizontal plane,  $\theta$  and Z are mentioned in the text.

mirror	$\theta$ ( $\mu\text{rad}$ )	R ( $\mu\text{m}$ )	Z ( $\mu\text{m}$ )
$C_1$	$\pm 1.5$	$\pm 1.0$	1.0
$C_2$	$\pm 0.5$	-	-
Mask	$\pm 8.5$	$\pm 1.0$	6.0
Illuminator	$\pm 20$	$\pm 5.0$	-
Wafer	$\pm 5$	$\pm 0.02$	-



## 5. Construction and alignment

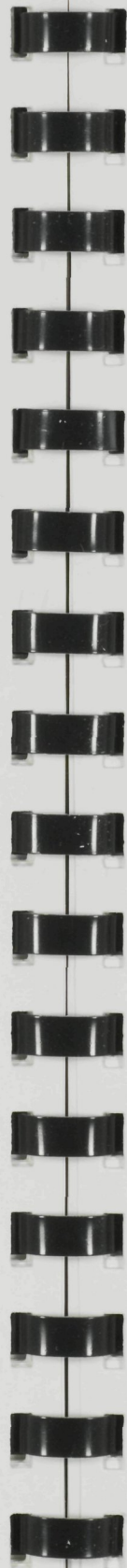
### 5.1 Construction of the mirror system

For the design of the micro mechanical mountings of the system, the temperature stability and the alignment accuracy have to be taken into account. Mirror  $C_2$  has the tightest tolerances (Table III), and therefore the position of this mirror serves as a reference point, i.e. has a fixed position. The range of displacements and the resolution of each mounting is listed in Table IV. For the positioning of mirror  $C_1$  with respect to  $C_2$ , a special construction is developed. Three mechanical mountings are used to mount mirror  $C_1$ . Each mounting consists of a single side notch hinge and a lever (Figure 1), which is used to reduce the displacement of the micrometer screw with a factor of 10 and therefore, enables an accuracy of 150 nm in all directions. In order to make an image at the wafer plane, the mask is translated along the optical axis rather than the wafer, which simplifies focusing. A translation of the mask does not affect the resolution, but will have an effect on the demagnification factor. The mounting of the mirrors can be performed with mechanical constructions, while the very stringent requirement of the selected 10% of the maximum deviation of each component is obtained.

The entire system is designed in such a way that it is insensitive for small temperature variations and alignment changes resulting. The entire construction is made of Superior Invar [28] with a linear expansion coefficient ( $\alpha$ ) of  $6 \times 10^{-7} \text{ K}^{-1}$ , which is close to the value of quartz ( $\alpha = 5.4 \times 10^{-7} \text{ K}^{-1}$ ). To compensate for the small difference in these expansion coefficients, the positioning balls of mirror  $C_2$  (Figure 1) are made of  $\text{Si}_3\text{N}_4$  ( $\alpha = 1.5 \times 10^{-6} \text{ K}^{-1}$ ). It is calculated that the alignment of the system is correct for temperature changes within  $\pm 2.5^\circ\text{C}$  from room temperature ( $20^\circ\text{C}$ ), which is easily obtained at our set-up. The temperature range is limited by the DOF.

Table IV: The range and accuracies of the mounting mechanisms of the optical element (symbols as in Table III)

mirror	$\theta$		R		Z	
	range (mrad)	resolution ( $\mu\text{rad}$ )	range (mm)	resolution ( $\mu\text{m}$ )	range (mm)	resolution ( $\mu\text{m}$ )
$C_1$	10	0.15	1	0.15	6	0.15
Mask	10	8.5	40	0.6	50	1
Illuminator	100	20	-	-	30	1
Wafer	250	1	-	-	8	0.2





## 5.2 Alignment

For the alignment of the system a custom made Fizeau interferometer [29] is constructed. The interferometer, which uses a He/Ne laser, enables alignment of mirror  $C_1$  with respect to mirror  $C_2$  with an accuracy of 300 nm in all directions. The positioning accuracy is within the alignment tolerances listed in Table IV. The alignment procedure is depicted in Figure 6. All components are positioned with respect to mirror  $C_2$ . The positions of the centres of curvature of mirrors  $C_1$  and  $C_2$  determine the optical axis of the system. The alignment of the mask and the illuminator to the optical axis is performed optically, by inspection of an image of the mask with a microscope. Final alignment and focusing of the mask is performed by inspection of images produced by EUV radiation.

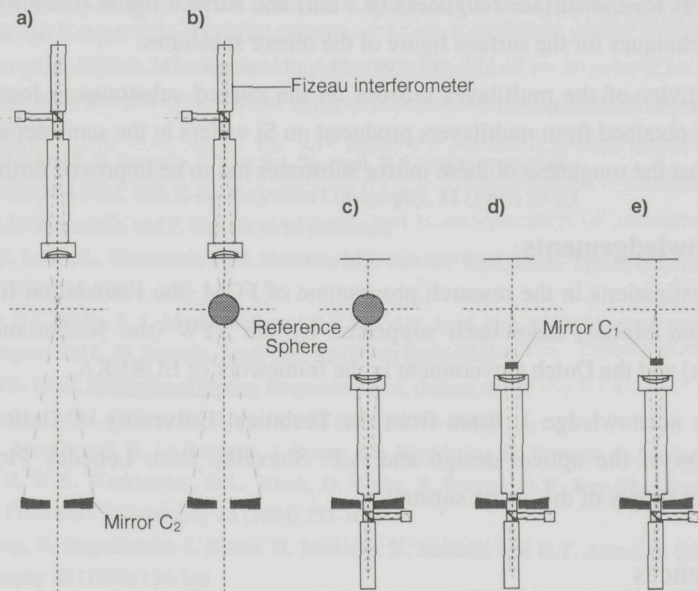


Figure 6: Procedure to align the two-mirror imaging optics. a) Firstly, mirror  $C_2$  is positioned in the mounting construction. Secondly, the interferometer is aligned with respect to  $C_2$ . b) A reference sphere is positioned at the centre of curvature of  $C_2$ . c) The interferometer is aligned to the other side of the reference sphere through  $C_2$ . d) The centre of curvature of mirror  $C_1$  is positioned at the focus of the interferometer, which is at the centre of curvature of the reference sphere. e) Mirror  $C_1$  is translated  $70 \mu\text{m}$  as described in section 3.1.

## 6. Conclusions

To be able to investigate various aspects of the feasibility of EUVL, a compact four-mirror system has been designed, constructed, and aligned. The system consists of a two-mirror imaging optics with a demagnification factor of 10, a spherical reflection mask, and a spherical illuminator. The intrinsic resolution is calculated to be 76 nm at a wavelength of 13 nm over a flat circular image field of 4 mm diameter. Taking into account reasonable requirements on fabrication, assembly and alignment tolerances, a resolution of 100 nm can be obtained using mechanical mountings for positioning of the optical elements. Preliminary experiments using 14.1 nm radiation show that the system is capable of imaging down to at least 200 nm. However, inspection of the patterns and/or resist process optimization so far limits the results obtained.

Second-generation designs consist of three- or four-mirror imaging systems, enabling the use of flat reflection masks, and an illumination scheme that is telecentric and enables Köhler illumination. At present the practical limitations for the use of an EUVL system are the requirements for the surface roughness (0.1 nm) and surface figure (0.2 nm), as well as the analysis techniques for the surface figure of the mirror substrates.

The reflectivity of the multilayer mirrors on the curved substrates is less than the 63% reflectivity obtained from multilayers produced on Si wafers in the same deposition run. This indicates that the roughness of these mirror substrates has to be improved further.

## 7. Acknowledgements

These investigations in the research programme of FOM (the Foundation for Fundamental Research on Matter) have been supported by the STW (the Netherlands Technology Foundation) and the Dutch Government in the framework of EUREKA.

We kindly acknowledge J. Braat from the Technical University of Delft for his critical examination of the optical design and A.P. Shevelko from Lebedev Physical Institute Moscow for supply of the quartz substrates.

## 8. References

1. D.A. Tichenor, A.K. Ray-Chaudhuri, G.D. Kubiak, K.B. Nguyen, S.J. Haney, K.W. Berger, R.P. Nissen, Y.E. Perras, P.S. Jin, L.I. Weingarten, P.N. Keifer, R.H. Stulen, R.N. Shagam, W.C. Sweatt, T.G. Smith, O.R. Wood II, T.E. Jewell, and F. Zernike, *OSA Proc. Extreme Ultraviolet lithography* **4** (1996) 2-6
2. M. Ito, S. Katagiri, H. Yamanashi, E. Seya, T. Ogawa, H. Oizumi, and T. Tersasawa, , *OSA Proc. Extreme Ultraviolet lithography* **4** (1996) 9-12
3. F. Bijkerk, *OSA Proc. Extreme Ultraviolet lithography* **4** (1996) 13-15
4. E. Louis, H.-J. Voorma, N.B. Koster, F. Bijkerk, Yu.Ya. Platonov, S.Yu. Zuev, S.S. Andreev, E.A. Shamov, and N.N. Salashchenko, *Microelectron. Eng.* **27** (1995) 235-238
5. D.G. Stearns, R.S. Rosen, and S.P. Vernon, *Appl. Opt.* **32** (1993) 6952-6960



6. The National Technology Roadmap for Semiconductors, Semiconductor Industry Association, San Jose (1994)
7. S. Harrell, T. Siedel and B. Fay, *Microelectron. Eng.* **30** (1996) 11-15
8. T.E. Jewell, J.M. Rogers, and K.P. Thompson, *J. Vac. Sci. Technol. B.* **8** (1990) 1519-1523
9. H.-J. Voorma, E. Louis, N. Koster, F. Bijkerk, T. Zijlstra, L.E.M. de Groot, B.A.C. Rousseeuw, J. Romijn, and E.W.J.M. van der Drift, submitted to *J. Vac. Sci. Technol. B.*
10. A.M. Hawryluk and L.G. Seppala, *J. Vac. Sci. Technol. B* **6** (1989) 2162-2166
11. J.E. Bjorkholm, J. Bokor, L. Eichner, R.R. Freeman, J. Grevus, T.E. Jewell, W.M. Mansfield, A.A. MacDowell, E.L. Raab, W.T. Silvast, L.H. Szeto, D.M. Tennant, W.K. Waskiewics, D.L. White, D.L. Windt, O.R. Wood II, and J.H. Bruning, *J. Vac. Sci. Technol. B* **8** (1990) 1509-1513
12. K. Kurihara, H. Kinoshita, T. Mizota, T. Haga and Y. Torii, *J. Vac. Sci. Technol. B* **9** (1991) 3189-3192
13. D.A. Tichenor, G.D. Kubiak, M.E. Malinowski, R.H. Stulen, S.J. Haney, K.W. Berger, L.A. Brown, W.C. Sweatt, J.E. Bjorkholm, R.R. Freeman, M.D. Himel, A.A. MacDowell, D.M. Tennant, O.R. Wood II, T.E. Jewell, W.M. Mansfield, W.K. Waskiewics, D.L. White, D.L. Windt, *Appl. Opt.* **32** (1993) 7068-7071
14. H. Kinoshita, K. Kurihara, T. Mizota, T. Haga, H. Takenaka, and Y. Torii, *Appl. Opt.* **32** (1993) 7079-7083
15. H. Nagata, M. Ohtani, K. Murakami, K. Mshima, Y. Maejima, T. Tanaka, T. Watanabe, Y. Yamashita, and N. Atoda, *Jpn. J. Appl. Phys.* **33** (1994) 360-363
16. H.-J. Voorma and F. Bijkerk, *Microelectron. Eng.* **17** (1992) 145 -148
17. Optical design software system, developed by Optical Research Associated, 550 N. Rosemaed Blvd, Pasadena, Ca 91107
18. A.M. Hawryluk and L.G. Seppala, *J. Vac. Sci. Technol. B* **6** (1989) 2162-2166
19. D.S. Goodman, *OSA Proc. Soft X-ray Projection Lithography*, **12** (1991) 27-29
20. S. Shevelko, L. Shmaenok, and F. Bijkerk to be published
21. F. Bijkerk, E. Louis, L. Shmaenok, H.-J. Voorma, M.J. van der Wiel, I.C.E. Turcu, G.J. Tallents, *Proc. SPIE* **1848** (1992) 516-520
22. J.B. Murphy, D.L. White, A.A. MacDowell, and O.R. Wood II, *Appl. Opt.* **32** (1993) 6920-6929
23. G.E. Sommargren and L. G. Seppala, *Appl. Opt.* **32** (1993) 6938-6943
24. M. Born and E. Wolf, *Principles of Optics*, Pergamon Press, Oxford, 1959
25. G.E. Sommargren and L.G. Seppala, *Appl. Opt.* **32** (1993) 6938-6944
26. Z. Tan, A.A. MacDowell, B. La Fontaine, J. Russo, J.E. Bjorkholm, D. Tennant, D. Taylor, M. Himel, O.R. Wood II, W.K. Waskiewicz, D.L. Windt, D. White, S. Spector, A.K. Ray-Chaudhuri, and R.H. Stulen, *OSA Proc. EUV Lithography* **23** (1994) 151-160
27. K.A. Goldberg, R. Beguiristain, J. Bokor, H. Medeck, K. Jackson, and D.T. Attwood, *OSA Proc. on EUV Lithography* **23** (1994) 134-141
28. Superior invar is a 36%Ni Fe alloy produced by Métalimphy, Imphy S.A, cedex 3 -92072 Paris La Défence
29. P.R. Yoder Jr. and W.W. Hollis, *J. Opt. Soc. Am.* **47** (1957) 858-861





## Characterization of multilayers using a new FFT analysis method of grazing-incidence x-ray reflectivity

### 1. Abstract

We discuss a new method to characterize multilayer structures with grazing-incidence reflectivity measurements using hard x-ray radiation, such as  $\text{Cu-K}_\alpha$  or  $\text{Mo-K}_\alpha$  radiation. The method is based on the analysis of the reverse Fourier transforms of the reflectivity at the Bragg peaks in  $q$ -space, the reflectivity data being obtained from an angular scan ( $\theta-2\theta$ ). This method is faster than curve fitting of the reflectivity data, results in an accurate value of the density and thickness of both materials, and needs no pre-assumptions about the material composition and the parameters of the multilayer. The method makes a distinction between interface roughness and layer thickness errors, and is independent of measurement of the critical angle. A minor disadvantage is that only an average value of the layer thickness is determined, rather than the individual layer thicknesses.

As an example our method is used to analyse small-angle reflectivity measurements of Mo/Si and Co/C multilayers. The parameters thus obtained are used to model a structure, which is subsequently used to predict the near-normal incidence reflectivity at soft x-ray wavelengths. The accuracy thus found corresponds to a relative error of 5%. The densities of a Mo/Si multilayer are determined independently with critical angle measurements to verify the values obtained from the grazing-incidence reflectivity measurements.

The results of the analysis of the Co/C multilayer are compared to values obtained using a conventional method based on the kinematical theory. However, the conventional method requires additional data of soft x-ray reflectivity measurements. The new method yields the same values for the multilayer parameters but does not require the extra soft x-ray measurements.

### 2. Introduction

The use of grazing-incidence reflectivity measurements with  $\text{Cu-K}_\alpha$  radiation is the most common method to characterize multilayer structures. Firstly, because of the high reflectivity

and the short wavelength (0.154 nm) compared to the multilayer period (in general from 1 to 10 nm), it is possible to measure many Bragg peaks in a  $\theta$ - $2\theta$  angular scan. This contributes to the accuracy of the parameters that are determined. Secondly, because of the relatively high penetration depth at large grazing-angles, the entire multilayer stack is measured [1]. Apart from these arguments there are also some practical reasons for the use of grazing-incidence reflectivity. The measurements involved are relatively simple and fast, do not need vacuum conditions, and can be done on standard laboratory equipment.

We developed a new method to analyse grazing-incidence reflectivity measurements, because existing methods either need some pre-assumptions, are laborious or need an experienced analyst. The new method is referred to as Bragg Maximum Reverse Fourier Transforms (BMFT). First we will describe the conventional methods including advantages and disadvantages. Then we describe the BMFT analysis. Finally we will compare our results of multilayer analysis to the results obtained from a conventional method.

### *2.1.1 Conventional methods of analysis*

In principle, there are two basic techniques to determine the multilayer parameters from grazing-incidence reflectivity measurements: using curve fitting of the modelled reflectivity or using the measured reflectivity, from which the multilayer parameters can be obtained using the dynamical theory. The first method is based on the summation of the individual reflections and transmissions of each interface, calculated with the Fresnel equations for single thin films. Most thin film analysis programs for x-rays either use this equation recursively [2,3,4] or in a matrix method [5,6]. The other technique is based on the dynamical theory, in which equations of the incident and scattered waves are used to calculate the multilayer parameters directly from the measured reflectivity.

In curve fitting, the most commonly used method to analyse hard x-ray reflectivity measurements, the calculated reflectivity of a modelled structure is fitted to the measured data, yielding values for the layer thicknesses, the material densities and the interface roughness. More advanced mathematical methods have been developed to improve this type of analysis. For example, improvements have been published recently, using an FFT of the reflectivity to determine the thickness of each layer and the average layer thickness errors [7,8].

The curve fitting method is useful when multilayer structures with a limited number of layer pairs are to be analysed. However, for most applications [9,10,11] multilayer mirrors with at least forty periods are needed. Curve fitting becomes a laborious task when all the individual layer thicknesses have to be fitted to the reflectivity signal, even if they are determined from an FFT. The general disadvantage of curve fitting is that it can result in values of local minima in the curve fitting procedure, which do not have to be the optimal values. For this reason start values of the interface roughness and densities close to the actual values are needed to obtain



reliable results. Although the layer thicknesses are determined from the FFT, the values of the interface roughness and densities are still obtained by fitting the calculated reflectivity to the measured signal.

For multilayers with a large number of periods ( $\geq 40$ ), a more suitable method has been developed. It is based on the dynamical [12], or kinematical theory, the latter of which is also referred to as vector theory [1,13]. Imperfect boundaries of the multilayer structures are incorporated into these calculations by describing the reduction of the reflected amplitude at the boundary by a Debye-Waller factor [14]. The layer thickness errors and the interface roughness are directly determined from the measured  $\theta$ - $2\theta$  scan. An example of the analysis method based on the kinematical theory, which includes the reflectivity in between the Bragg maxima, is the method described in Refs 1, 15, and 16. This method is used for comparison in section 4.2 and is in this paper referred to as "classical" method.

A disadvantage of the classical method, as all other methods based on the kinematical theory, is that some uncertainty is introduced by the need to determine the reflectivity in between the Bragg maxima. At these points in the reflectivity curves the data is difficult to extract, because it is influenced by the side fringes of the Bragg maxima and by statistical and detector noise. Furthermore, the interface roughness and the densities are still determined by fitting the calculated reflectivity to the measurement. Therefore, the method is still laborious. A fitting procedure can result in non-unique values for the reasons given above.

### 2.1.2 The BMFT analysis

In the BMFT analysis discussed here, which is also based on the kinematical theory, the average electron density profile of the multilayer is determined. From this, the multilayer parameters, such as interface roughness, thickness ratio, layer thickness errors and densities are determined. The average refractive index and the d-spacing are obtained from the angular positions of the Bragg maxima.

The advantage of the BMFT method is that no start values for the multilayer parameters are needed, because the parameters are directly determined from the analytical equations. Therefore, the method is fast and needs no curve fitting. The formulas for thickness errors in our paper are statistical values, i.e. they give only average thickness errors and no individual layer thicknesses. However, this is not a serious disadvantage when comparing different multilayers, as for instance in process optimization procedures. The judgement about the quality of the multilayer will not be influenced by the fact that the individual layer thicknesses are not known, because only general quantities, such as the interface roughness and the average layer thickness errors, are used for comparison. Another limitation of the statistical approach might be that an individual multilayer may not be described by the statistical expectation values, indicating that the parameters cannot be described statistically. This is for

instance the case when a multilayer does not have a normal distribution of layer thickness errors.

### 3. Theory of BMFT analysis

We start with the treatment of the analysis, involving firstly the determination of the d-spacing, and secondly, the determination of the thickness ratio ( $\Gamma$ ) of the high-Z material versus the period thickness, the root mean square value of the interface roughness ( $\sigma$ ), the layer thickness errors ( $\zeta$ ), and the density of both materials ( $\rho_H, \rho_L$ ). The indices H and L refer to respectively the high-Z (usually a metal) and low-Z material (spacer material).

#### 3.1.1 The d-spacing and average refractive index decrement

To determine the d-spacing ( $\Lambda$ ) and the refractive index decrement ( $\delta$ ), the extended Bragg law is used:

$$\sin^2 \theta_m = \frac{m\lambda \sin \theta_m}{2\Lambda} + \delta \quad (1)$$

Where  $m$ : order of the Bragg maximum

$\lambda$ : wavelength

Although this expression was first used for single thin films [17,18] it is also appropriate for multilayers, because at the Bragg maxima all boundaries add in phase to the total reflectivity. However, Eq. (1) is deduced from a first-order approximation of the Bragg law for crystals, in which the higher-order terms of  $\delta$  and the absorption ( $\beta$ ) are neglected. This approximation can only be used when  $\sin^2 \theta_m \gg \delta$ , meaning that in a practical measurement a correction of the position and height of the first-order Bragg maximum would be needed when  $\Lambda$  is larger than  $\sim 5$  nm. At the higher-order Bragg maxima this correction is negligible. Therefore, we prefer not to use the first order Bragg maxima for the determination of  $\delta$  and  $\Lambda$ .

Using the measured positions of the Bragg maxima ( $\theta_m$ ), a linear least-squares fit is made to Eq. (1), yielding the values for  $\delta$  and  $\Lambda$ . In order to solve Eq. (1), in principle only two maxima are required to resolve the two unknown parameters,  $\Lambda$  and  $\delta$ . However, for a reliable solution at least three Bragg maxima are preferred. It is noted that for most practical multilayer structures at least four maxima can be measured. Excluding the first order Bragg maximum, as argued before, we use the second and higher order Bragg maxima for the determination of  $\delta$  and  $\Lambda$ .

The above described method to calculate  $\delta$  is more accurate than determination of  $\delta$  from the minimum of the derivative of the reflectivity near the critical angle. This minimum is difficult to determine for the short wavelength used and for  $\Lambda$  larger than 5 nm, since this combination of wavelength and d-spacing causes interference of the reflection near the critical angle and the side maxima of the first order Bragg maximum.



### 3.1.2 Dielectric function

The reflectivity of a multilayer is dependent on the value of the refractive index ( $n$ ) and therefore on the dielectric constant ( $\epsilon$ )

$$\bar{n} = \sqrt{\epsilon} = 1 - \delta - i\beta \quad (2)$$

The imaginary part of Eq. (2), with the average absorption index ( $\beta$ ), can be neglected because the value of  $\beta$  is small ( $\approx 10^{-6}$ ) compared to  $1 - \delta$  ( $\approx 1$ ) for the Cu-K $_{\alpha}$  radiation most commonly used. With Eqs. (1) and (2), only the average value of  $\epsilon$  through the stack can be determined. However, for a full analysis of the multilayer structure, this is not sufficient. The dielectric constant has to be resolved as a function of depth ( $z$ ) into the multilayer. This dielectric function,  $\epsilon(z)$ , is also referred to as density profile. We will show that from the dielectric function the material densities, the interface roughness, the layer thickness errors and  $\Gamma$  can be obtained.

For the analysis of x-ray reflectivity measurements it is more convenient to introduce the reciprocal or  $q$ -space,  $q$  representing the change in momentum of a photon at specular reflection. In this space the factor  $q_m = 2\pi m/\Lambda$  is used to indicate the position of the  $m$ -th order Bragg maximum.

For a practical multilayer, in which the effect of the interface roughness is included, the dielectric function has a shape as given by the dashed line in Figure 1 (the solid line represents the ideal case). The dielectric function depends periodically on the depth ( $z$ ). The real part can be decomposed into its Fourier components [19]

$$\epsilon(z) = a_0 + \sum_{m=1}^{\infty} a_m \cos(q_m z + \Phi_m(z)) \quad (3)$$

where  $a_m$ : the harmonic amplitude obtained from the  $m$ -th order Bragg maximum  
 $a_0$ :  $(1 - \delta)^2$   
 $\Phi_m$ : the phase difference due to layer thickness errors

The dielectric function can be determined if the harmonic amplitudes can be calculated and if  $\Phi_m$  can be neglected. This type of phase differences is usually small, as will be discussed in the paragraph about layer thickness errors. The harmonic amplitudes ( $a_m$ ) can be determined from the reflectivity data around the Bragg peaks of the order  $m$  ( $R_m$ ), using a reverse Fourier transformation [20]. We will first introduce a co-ordinate translation for each Bragg peak from  $q_z$  to  $Q_z$ :

$$Q_z = q_z - q_m = \frac{2\pi}{\lambda} \left( 2 \sin \theta - \frac{\delta}{\sin^2 \theta} \right) - q_m \quad (4)$$

These translations for each Bragg peak result in a simplified equation from which the harmonic amplitudes can be obtained separately.



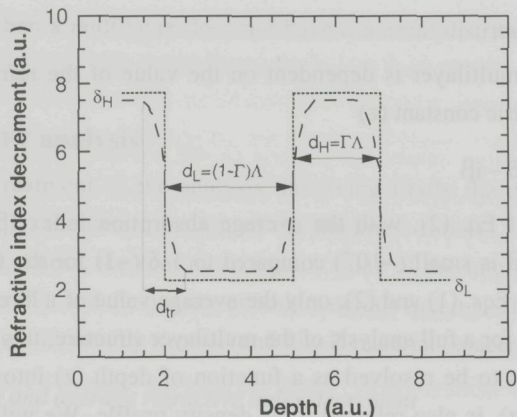


Figure 1: An example of the refractive index decrement as a function of depth ( $z$ ) into the multilayer of an ideal multilayer (dotted line) and a real multilayer (dashed line), with  $d_L$  indicating the thickness of the low-Z material,  $d_H$  the thickness of the high-Z material and  $d_{tr}$  the thickness of the transition layer.

The reverse Fourier transform,  $I_m(\alpha)$ , of the reflectivity around a Bragg peak is then given by:

$$I_m(\alpha) = \int_{Q_{z,2}}^{Q_{z,1}} R_m(Q_z) e^{-iQ_z \alpha} dQ_z = I_{re,m}(\alpha) + iI_{im,m}(\alpha) \quad (5)$$

Where  $R_m$ : reflectivity at the  $m$ -th order Bragg peak

$Q_{z,1}$ ,  $Q_{z,2}$  the integration limits of  $R_m$

$\alpha$ : Fourier transform of  $Q_z$  (with dimension length)

The real and imaginary parts of Eq. (5) can be calculated separately. The maximum interval for  $Q_{z,1}$  and  $Q_{z,2}$  is the range between the half orders below and above the peak position. However, the main contributions to this integral are from the points close to the Bragg maximum. We determine the integral by increasing the range of  $Q_{z,1}$  and  $Q_{z,2}$  until this increase adds only 0.0001% to the value of the integral. The harmonic amplitudes,  $a_m$ , are determined from the real part of the integral ( $I_{re}(\alpha)$ ) of Eq. (5) according to a method described by Nagakubo [21]. Equation (5) can be solved at  $\alpha = 0$ , while taking into account that  $Q_z \gg 1/L$ , in which  $L$  is the total thickness of the stack, i.e. the number of periods multiplied by  $\Lambda$ . This results in:

$$I_{re}(0) \approx \frac{2\pi L a_m^2 k^4}{q_m^2} \quad (6)$$

in which  $k$  is the wavenumber ( $2\pi/\lambda$ ). Because  $I_{re,m}(0)$  is determined from the Fourier transform in Eq. (5), the harmonic amplitudes can now be calculated:

$$a_m \approx \sqrt{\left(\frac{q_m}{k^2}\right)^2 \left(\frac{I_{re,m}(0)}{2\pi L}\right)} \quad \text{for } m \geq 1 \quad (7)$$

### 3.1.3 Interface roughness and $\Gamma$ value

In general the harmonic amplitudes of a periodic function, such as the dielectric function, is described by the following Equation:

$$a_m = \frac{\Delta\varepsilon \sin(m\pi\Gamma)}{m\pi} \exp\left(\frac{q_m^2 \sigma^2}{2}\right) \quad (8)$$

$$\text{where } \Delta\varepsilon = \varepsilon_H - \varepsilon_L \quad (9)$$

We note that for an ideal dielectric function the harmonic amplitudes are determined by the first part of Eq. (8). However, we have to take into account the interface roughness, which is caused by a transition layer ( $d_t$ ), a layer with a certain thickness in which the high-Z and low-Z material are mixed (Figure 1). Therefore, the exponential factor of Eq. (8), known as the Debye-Waller factor, is included. To determine the interface roughness, the  $\Gamma$  value, and  $\Delta\varepsilon$ , we rewrite Eq. (8) as a linear function of  $m^2$ :

$$m^2 \frac{2\pi^2 \sigma^2}{\Lambda^2} = \ln\left(\pi m \left| \frac{a_m}{\sin(m\pi\Gamma)} \right| \right) + \ln(\Delta\varepsilon) \quad (10)$$

$\Gamma$  is then determined by assuming a linear dependence on  $m^2$  of the second term of Eq. (10). In the equation the value of  $\Delta\varepsilon$  is primarily determined by the first-order harmonic amplitude ( $a_1$ ). Since the first-order Bragg maximum is not taken into account, in practice  $\Delta\varepsilon$  is determined by the higher order harmonic amplitudes. Finally,  $\Delta\varepsilon$  and  $\sigma$  can be calculated using Eq. (8), since  $\Gamma$  is known from Eq. (10) and  $a_m$  from Eq. (7).

Diffuse scattering from the interfaces of a good multilayer is very small [22] and usually does not disturb the method described above. In principle, diffuse scattering can be taken into account by a renormalization of the intensity using the Debye-Waller factor for correlated and uncorrelated roughness, as has been suggested by Savage [23].

### 3.1.4 Layer thickness errors

The next parameters that will be determined are the average layer thickness errors or average period deviations. These can be determined using Eq. (5). Differentiating the imaginary part and double differentiating the real part of Eq. (5), we find a relation between Eq. (6) on the one hand and the integral of the period deviations and period deviations squared on the other hand. Because the period deviations are caused by a deviation from the average at the interface, these integrals can be rewritten as the sum of all period deviations and the sum of the squared period deviations, shown in Eq. (11) and (12). Using the real and imaginary part



of Eq. (5), the sum of all period deviations and the sum of the squared period deviations can then be calculated:

$$\sum_i \zeta_i = \frac{L\Lambda}{q_m I_{re,m}(0)} \left( \frac{dI_{im,m}(\alpha)}{d\alpha} \right)_{\alpha=0} \quad (11)$$

$$\sum_i \zeta_i^2 = \frac{L\Lambda^2}{q_m^2 I_{re,m}(0)} \left( \frac{d^2 I_{re,m}(\alpha)}{d^2 \alpha} \right)_{\alpha=0} \quad (12)$$

$\zeta_i$ : the deviation of the thickness of the  $i$ -th layer from  $\Lambda$ .

The determination of the thickness fluctuations is valid if the thicknesses are distributed normally around an average thickness and if the interface roughness is constant for all layers. This is discussed in section 4.

### 3.1.5 Density of both materials

In order to determine the densities of both materials, the values of  $\epsilon_L$  and  $\epsilon_H$  have to be calculated. These are the extrema of the index modulation before taking into account the mixing caused by the interface roughness. The value of  $\epsilon$  is known from  $\delta$  in Eq. (1) and  $\Delta\epsilon$  is determined with Eq. (8). The dielectric constants of both materials can then be found using:

$$\epsilon = \Gamma\epsilon_H + (1 - \Gamma)\epsilon_L = \Gamma\Delta\epsilon - \epsilon_L \quad (13)$$

The  $\delta_L$  and  $\delta_H$  (the refractive index decrement for the low-Z and high-Z material respectively) can be determined from the dielectric constants in Eq. (12) in combination with Eq. (2). Similarly to Eq. (13), and neglecting the higher-order terms, we find the average refractive index decrement ( $\delta$ ) of the multilayer, which depends on the material refractive indices and  $\Gamma$  [24].

$$\delta = \Gamma\delta_H + (1 - \Gamma)\delta_L \quad (14)$$

The densities of both materials can now be calculated using Eq. (14) and Eq. (15).

$$\delta_{H,L} = \lambda^2 \frac{\rho_{H,L}}{A_{H,L}} \frac{1}{C} \quad (15)$$

where  $C = \frac{2\pi}{r_0 N_A} \approx 3.7026 \cdot 10^{-11} \text{ mol} \cdot \text{cm}^{-1}$

- $N_A$ : Avogadro's number
- $r_0$ : classical electron radius
- $\rho_{H,L}$ : density of the high-Z or low-Z material
- $A_{H,L}$ : atomic weight of the high-Z or low-Z material



### 3.1.6 Verification of the density values

With the above-described method the densities can be determined. These determine the refractive index of the multilayer materials and therefore, the reflectivity of the multilayers. Because of the importance of the densities, a second method is used to verify the values of the density obtained from the BMFT. This method is based on the determination of  $\delta$  from critical angle measurements using wavelengths between 0.55 nm and 0.67 nm according to the method of Parrat [2]. This method is preferred to determine  $\delta$  since for these wavelengths the absorption coefficient cannot be neglected, in contrast to measurements using Cu-K $_{\alpha}$  radiation. The refractive index decrement is determined as a function of the wavelength using Eqs. (14) and (15):

$$\delta C = (\lambda^2 f_{i,H}) \Gamma \left( \frac{\rho_H}{A_H} \right) + (\lambda^2 f_{i,L}) (1 - \Gamma) \left( \frac{\rho_L}{A_L} \right) \quad (16)$$

in which  $f_i$  is the atomic scattering factor [24].

With the calculated values of  $\delta$  and the scattering factors ( $f_{i,L}$ ,  $f_{i,H}$ ) a linear-least squares fit to Eq. (16) can be made, yielding the values for  $\rho_H$  and  $\rho_L$ .

The method of Parrat is correct when the multilayer consists of only the high-Z and the low-Z materials, without contamination by other materials. This is generally the case for the pure deposition materials and controlled vacuum conditions in multilayer deposition systems.

## 4. Experimental

### 4.1 Fabrication of multilayers analysed

As an example the BMFT analysis of two multilayer systems is described in more detail. These multilayer coatings have been produced using e-beam evaporation. The deposition system has been described elsewhere [25]. During deposition the layer thickness is monitored in-situ by measuring the oscillations in the reflectivity of N-K radiation (3.16 nm) with growing thickness.

The 32-period Mo/Si multilayers analysed in this work are produced with the in-situ monitor at 13.5° angle of incidence with respect to the substrate, resulting in a  $\Lambda$  of 7.0 nm. Ion etching of the Si layers, using 300 eV Kr $^+$  ions at 45° angle of incidence, is applied to reduce the interface roughness [26]. The last layer deposited is a Si layer because Si has proven to be a better top surface than Mo [27]. Forty-period multilayer mirrors produced using the same process parameters are known to show a final reflectivity of 64% for 13.6 nm radiation at near-normal incidence [28].

The second type of multilayer analysed are Co/C multilayers with 70 periods and  $\Lambda$  of 4.0 nm. The multilayers are produced with the in-situ monitor at 23.5° with respect to the surface. For

these multilayers the Co layers are etched with  $Kr^+$  ions of 500 eV at  $20^\circ$  angle of incidence [29].

#### 4.2 Reflectivity measurement set-ups

Small-angle reflectivity measurements ( $\theta$ - $2\theta$  scans) with  $Cu-K_\alpha$  radiation are used to characterize the multilayer structures. An angular resolution of better than  $0.01^\circ$  was obtained with a Ge- or a Si-crystal monochromator in combination with two slits [20, 30]. In order to verify the densities, the critical angle is measured at various wavelengths. These measurements have been performed at an undulator beamline using a double crystal monochromator at station 3.4 of the Daresbury SRS [31]. For our measurements wavelengths between 0.55 nm and 0.67 nm were used. The near-normal incidence reflectivity of the multilayers at a wavelength of 13.55 nm were measured using a conventional electron impact x-ray source [32], and angular scans. The reflectivity has an absolute accuracy of 5%, while the accuracy of the wavelength is  $\pm 5\%$ .

### 5. Results

#### 5.1 Application to a Mo/Si multilayer

The values of the Mo/Si multilayer parameters obtained from the BMFT analysis are listed in Table I. The value for the interface roughness is found to be 0.44 nm, the layer thickness error amounts to 0.2 nm, and the d-spacing is 6.9 nm. The values of the densities of Si ( $2.5 \text{ g/cm}^3$ ) and Mo ( $9.3 \text{ g/cm}^3$ ) in Table I differ from the values for bulk material of Si ( $2.3 \text{ g/cm}^3$ ) and Mo ( $10.2 \text{ g/cm}^3$ ). Firstly, this is caused by the deposition process, which normally results in a lower density than that of bulk materials. Secondly, the densities can change by diffusion or intermixing of Si atoms into the Mo layer and vice versa. The average refractive index decrement in Eq. (1) determines the average of the calculated dielectric constant. Its inaccuracy is caused by the instrumental resolution, and amounts to  $\pm 3\%$ , and also determines the error in the densities.

##### 5.1.1 Calculation of density profile

The BMFT analysis results in calculated harmonic amplitudes, which are now used for the calculation of the density profile (Table II). However, to determine the density profile a correction of the first-order harmonic amplitude is required. This is due to the limited

Table I: The calculated parameters of the multilayers

Sample	Method	$\Lambda$ (nm)	$\Gamma$	$\sigma$ (nm)	$\zeta$ (nm)	$\rho_L$ ( $\text{g/cm}^3$ )	$\rho_H$ ( $\text{g/cm}^3$ )
Mo/Si	BMFT	6.9	0.374	0.44	0.2	2.5	9.3
Co/C	BMFT	3.9	0.406	0.33	0.2	3.3	6.8
Co/C	CLASSICAL	3.9	0.405	0.34	0.17	-	-



penetration depth of the Cu-K $\alpha$  radiation, which is less than the 32-periods of the multilayer, at the angle of the first Bragg maximum [33]. Therefore, the value of  $a_1$  has to be corrected by reducing the value of  $L$ , in Eq. (7), to the penetration depth. We note that the values for the interface roughness and layer thickness errors are not influenced by the limited penetration depth, because they are determined from the harmonic amplitudes obtained from the second and higher-order Bragg peaks.

We proceed to determine whether the number of harmonics in Table II is sufficient to accurately characterize the dielectric function. In a practical multilayer the thickness of the transition layer is described by the density profile. In the dielectric function, Eq. (3), the thickness of the transition layer is determined by the number of harmonics. In the investigated Mo/Si multilayer the thickness of the transition layer (0.98 nm) corresponds to two times the calculated interface roughness (0.44 nm), i.e. two times the standard deviation assuming a Gaussian distribution of the mixed materials at the interface. Therefore, we conclude that the number of harmonics that are listed in Table II is sufficient to characterize this multilayer structure.

Table II: The calculated harmonic amplitudes for the Mo/Si and the Co/C samples.

Sample	$a_0$	$a_1$	$a_2$	$a_3$	$a_4$
Mo/Si	0.999973	$4.3 \times 10^{-5}$	$2.1 \times 10^{-6}$	$1.1 \times 10^{-6}$	$6.7 \times 10^{-7}$
Co/C	0.999987	$3.1 \times 10^{-5}$	$8.9 \times 10^{-6}$	$2.9 \times 10^{-6}$	$9.5 \times 10^{-7}$

### 5.1.2 Simulation of small-angle reflectivity

The parameters obtained from the BMFT analysis are used to simulate the small-angle reflectivity. The simulated and measured data are displayed in Figure 3. The differences in reflectivity observed in Figure 3 are caused by the fact that not all the individual thicknesses of the stack are known.



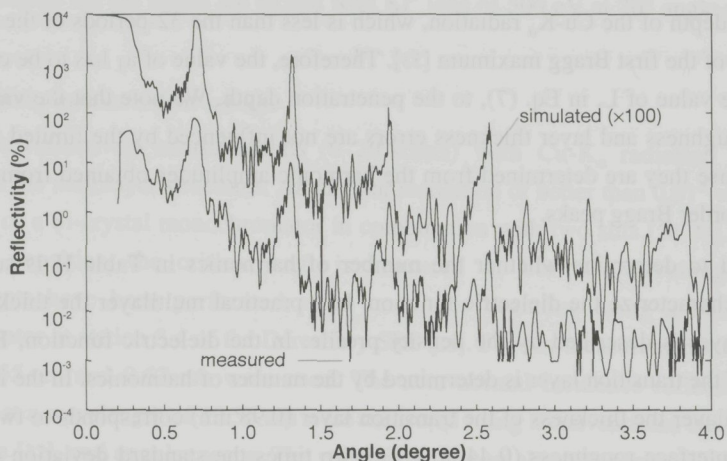


Figure 3: Comparison between measured and simulated  $\text{Cu-K}\alpha$  reflectivity of the Mo/Si multilayer.

### 5.1.3 Simulation of soft x-ray reflectivity

With the values of the parameters ( $\Lambda$ ,  $\Gamma$ ,  $\sigma$ ,  $\rho_L$ ,  $\rho_H$ ) obtained, a prediction can be made for the near-normal incidence reflectivity. In Figure 2 the calculated near-normal incidence reflectivity is compared to the measured value. The deviation of the calculated reflectivity from the measured signal is less than 5%, indicating the accuracy of the BMFT analysis. The value of the layer thickness errors (0.2 nm) results in an inaccuracy of 1% in the value and

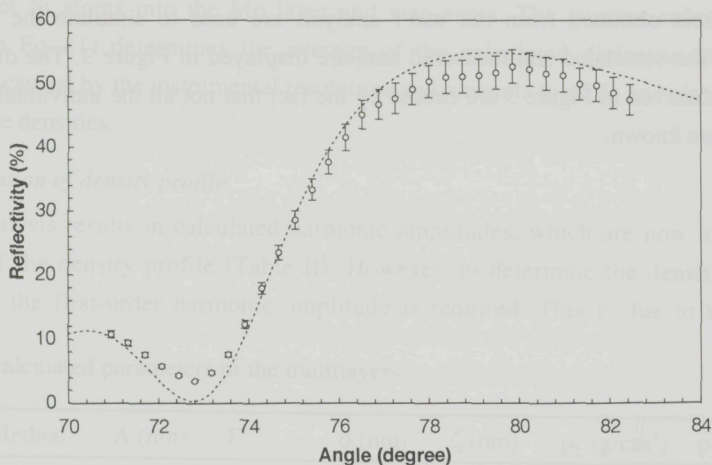


Figure 2: The measured ( $\circ$ ) and calculated (dashed line) near-normal incidence reflectivity for the Mo/Si multilayer at  $\lambda = 13.55$  nm.

position of the maximum reflectivity, depending on the actual set of layer thicknesses. We conclude that the analysis of the hard x-ray measurement results in good values for the densities.

#### 5.1.4 Verification of the density

The densities obtained from the BMFT analysis are compared with results from the critical angle measurements at soft x-ray wavelengths between 0.55 and 0.67 nm (Table III). For these wavelengths Parrats method is used. The critical angle for the hard x-ray radiation is calculated using  $\delta$  determined from Eq. (1). With Eq. (16) the densities of both materials are calculated, resulting in a value of  $2.7 \text{ g/cm}^3$  for Si, and  $10.1 \text{ g/cm}^3$  for Mo. These measurements result in a higher value of the Si density because the position of the critical angle at these wavelengths is more sensitive to a fraction of Mo in the Si layer, than at the  $\text{Cu-K}_\alpha$  wavelength. In the next two paragraphs we discuss the influence of these density values on the calculation of respectively the small-angle and near-normal incidence reflectivity.

For the small-angle reflectivity measurements no improvement in the calculated reflectivity is found when taking into account the density values obtained from the critical angle measurements. Therefore, we conclude that the density, determined by the BMFT method is as accurate as can be expected from the small-angle reflectivity measurements.

However, a slight improvement of the prediction of the near-normal incidence reflectivity can be obtained, if the densities are determined with soft x-ray critical angle measurements ( $\lambda = 0.55\text{-}0.67 \text{ nm}$ ). Using the latter values the calculated reflectivity fits the measurement.

Table III: The measured critical angles for various wavelengths for the Mo/Si multilayer.

Wavelength (nm)	0.154	0.551	0.620	0.660
Critical angle	0.298°	0.920°	1.040°	1.080°

#### 5.2 Application to a Co/C multilayer

The second type of multilayer investigated in order to illustrate our method is a 70-period Co/C multilayer. This multilayer is part of a series of multilayers produced to be used as a tuneable monochromator in front of a Wolter-type x-ray telescope [29]. This set-up will be used in the Spectrum Röntgen Gamma satellite [11, 34]. In the grazing-incidence reflectivity measurement (Figure 4), four Bragg peaks of the multilayer have been measured. The multilayer is analysed both with the BMFT and the classical method. First we show results of the BMFT analysis. In this case no correction is needed for the value of  $a_1$  of this multilayer, since at the first-order Bragg maximum ( $1.15^\circ$ ) the penetration depth is more than the thickness of the multilayer (70 periods and  $\Lambda = 3.9 \text{ nm}$ ). The values of the parameters determined from the BMFT analysis are listed in Table II. The calculated harmonic amplitudes



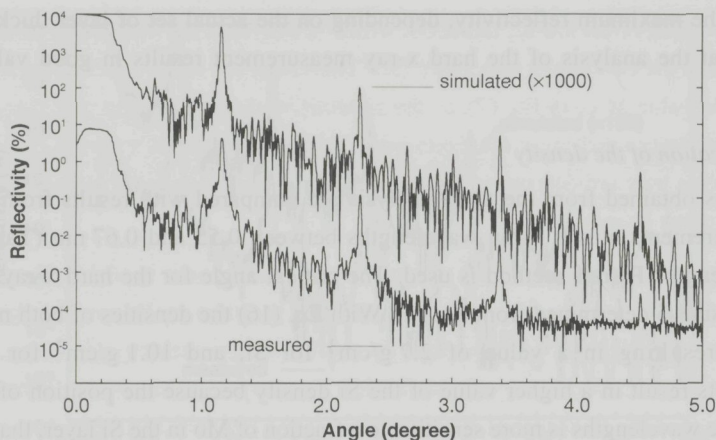


Figure 4: Comparison between measured and simulated  $\text{Cu-K}\alpha$  reflectivity of the  $\text{Co/C}$  multilayer. The peak at  $4.7^\circ$  originates from the  $\text{Si}(111)$  substrate.

(Table II) of the  $\text{Co/C}$  sample are used to calculate the density of the carbon and the cobalt layer, which results in density values of respectively  $3.3 \text{ g/cm}^3$  and  $6.8 \text{ g/cm}^3$ . These values are then used to simulate the small-angle reflectivity measurement (Figure 4) and the soft x-ray reflectivity between 4.4 and 7.1 nm. Similar to the case of the  $\text{Mo/Si}$  multilayer the relative error of the simulated soft x-ray reflectivity amounts less than 5%.

### 5.2.1 Comparison with a classical analysis method

If we compare the bfmt values of the d-spacing, the interface roughness and layer thickness errors with the values obtained from an analysis according to a classical method, we conclude that almost identical values are obtained (last row in Table I). We will briefly discuss the classical method used. A detailed description is published elsewhere [1, 15, 16]. The value of  $\Lambda$  is determined in an almost similar way as has been described for the BMFT analysis. For a multilayer the ratio of the reflectivity at the Bragg maxima to the reflectivity in-between the maxima is determined by the layer thickness errors and  $\Gamma$ . In the classical method the layer thickness errors are determined by fitting the calculated reflectivity, using  $\Gamma$  as the fit parameter, to the heights of the measured Bragg maxima, so that the value of the layer thickness errors is the same for each Bragg maximum. One can calculate the interface roughness, used in the Debye-Waller factor, from the reflectivity at the half orders. This is the reflectivity in between the Bragg maxima corresponding to positions in Eq. (1) for  $m = 1/2, 3/2, 5/2$  etc. However, to obtain the Debye-Waller factor, the optical constants of the multilayer are set to tabulated values [24], which are in some cases slightly corrected based on the operators personal experience. Finally, the optical constants can be obtained from fitting the simulated soft x-ray reflectivity to the measured soft x-ray reflectivity, using the measured values of the interface roughness and layer thickness errors.

The results of this analysis, a d-spacing of 3.9 nm and a  $\Gamma$  factor of 0.405 are similar to the values found using the BMFT analysis. There is a small difference in the interface roughness and layer thickness errors. These two are generally difficult to distinguish, because both influence the reflectivity of the maxima and between these maxima. From near-normal incidence reflectivity measurements, these parameters can be distinguished, because then the layer thickness errors also influence the position of the Bragg maxima. This position cannot only be obtained from the value of the d-spacing, but is dependent on the actual stack of layer thicknesses. Interface roughness would only decrease the height of the maximum.

### 5.3 Verification of assumptions in theory

Firstly, we verify the assumptions made about the interface roughness and layer thickness errors. We have assumed that the interface roughness is constant for all layers. The in-situ reflection signal enables us to monitor the change of the interface roughness: when the interface roughness would increase, the amplitude of the in-situ reflection would decrease. The measured in-situ reflection of a Mo/Si multilayer is displayed in Figure 5, in which the dashed line is a simulation of the in-situ reflection of a Mo/Si multilayer with a constant interface roughness of 0.44 nm (this value is listed in Table I). Because the amplitude of the measured in-situ signal is constant we conclude that the interface roughness is constant throughout the stack. The minor differences between these two curves are caused by small layer thickness errors.

The second assumption we made is that the layer thickness errors are distributed normally. This is checked by the value of the summations of thickness deviations, Eq. (11), which for a normal distribution has to be small. In the multilayer systems investigated here, we conclude

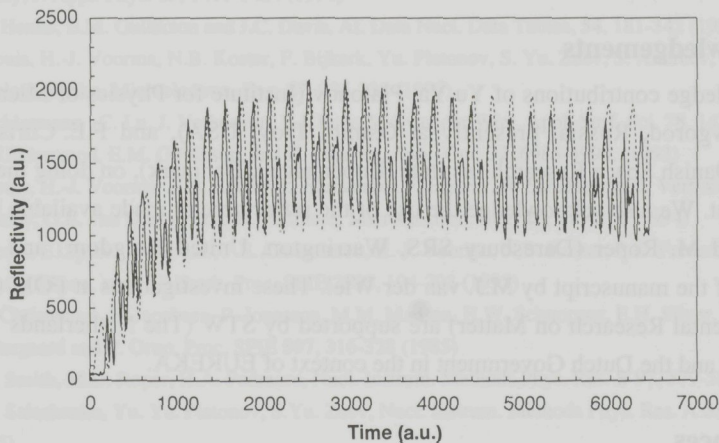


Figure 5: Comparison between a measured (solid line) and simulated (dashed line) in-situ reflection signal of a Mo/Si multilayer versus time. The simulated reflectivity is calculated using a constant interface roughness of 0.44 nm.



that the layer thickness errors are indeed distributed normally. This can be understood, because the determination of the deposition and etch end-points from extrema in the in-situ reflection are primarily affected by statistical noise in the intensity of the x-ray source.

## 6. Conclusions

We have developed a new analysis method of grazing-incidence reflectivity measurements of multilayer mirrors. We conclude that using the BMFT analysis the important multilayer parameters, such as the d-spacing, the interface roughness, the layer thickness errors, and the densities can be determined accurately. We demonstrated that, using the values obtained from the BMFT analysis the small-angle reflectivity can be simulated and the near-normal incidence reflectivity of the multilayer can be predicted accurately. Besides having a good accuracy, the BMFT analysis requires no fitting, is fast, and does not require corrections to input data based on personal experience. We have applied the BMFT analysis to two multilayer systems, namely Mo/Si and Co/C multilayers. The BMFT method is compared with a classical method used for analysis of the same grazing-incidence reflectivity measurement. Both methods appeared to yield nearly identical results, but the BMFT lacks the necessity for additional soft x-ray reflectivity measurements, which are needed for the classical method.

A separate issue has been the determination of the densities of materials deposited. We have compared the densities from the BMFT analysis with an independent method to determine the densities based on measurement of the critical angles for soft x-ray radiation. We found that the predicted near-normal incidence reflectivity is more accurate if the densities obtained from soft x-ray critical angle measurements (0.55-0.67 nm) are included, but the 5% error obtained using the BMFT analysis only is considered to be acceptable for most analysis purposes.

## 7. Acknowledgements

We acknowledge contributions of Yu.Ya. Platonov (Institute for Physics of Microstructures, Nizhny Novgorod, Russia, presently at Osmic, Troy, USA), and F.E. Christensen and S. Abdali (Danish Space Research Institute, Copenhagen, Denmark), on doing the reflectivity measurement. We also acknowledge the use of the reflectometer made available by G.E. van Dorssen and M. Roper (Daresbury SRS, Warrington, United Kingdom) and the critical reviewing of the manuscript by M.J. van der Wiel. These investigations at FOM (Foundation for Fundamental Research on Matter) are supported by STW (The Netherlands Technology Foundation) and the Dutch Government in the context of EUREKA.

## 8. References

1. E. Spiller, A. Rosenbluth, Proc. SPIE **563**, 221-236 (1985)
2. P. Rouard, Ann. Phys. (France) **5**, 596-639 (1937)
3. L.G. Parrat, Phys. Rev. **95**, 359-368 (1954)

4. J.H. Underwood and T.W. Barbee, Jr., *Appl. Opt.* **20**, 3027-3034 (1981)
5. F. Abelés, *Ann. Phys. (France)* **5**, 596-639 (1950)
6. M. Born and E. Wolf, *Principles of Optics*, 5th ed., Pergamon Press, Oxford 1975
7. F. Bridou, B. Pardo, *J. Phys. (France)* **4**, 1523-1531 (1994)
8. F. Bridou, B. Pardo, *J. of X-ray Sci. and Technol. (USA)* **4**, 200-216 (1994)
9. E. Louis, F. Bijkerk, L.A. Shmaenok, H.-J. Voorma, M.J. van der Wiel, R. Schlatmann, J. Verhoeven, E.W.J.M van der Drift, J. Romijn, B.A.C. Rousseeuw, F. Voß, R. Désor and B. Nikolaus, *Microelectron. Eng.* **21**, 67-70 (1993)
10. A.P. Zwicker, S.P. Regan, M. Finkenthal, H.W. Moos, E.B. Saloman, R. Watts and J.R. Roberts, *Appl. Opt.* **29**, 3694-3698 (1990)
11. F.E. Christensen, S. Abdali, P.K. Frederiksen, A. Hornstrup, I. Rasmussen, N.J. Westergaard, H.W. Schnopper, E. Louis, H.-J. Voorma, N.B. Koster, H. Wiebicke, I. Halm, U. Geppert, E. Silver, M. Legros, K. Borozdin, K.D. Joensen, P. Gorestein, J. Wood and G. Gutman, *J. Phys. (France)* **4**, 124-126 (1994)
12. B. Vidal and P. Vincent, *Appl. Opt.* **23**, 1794-1801 (1984)
13. A.A. Frearman, S.V. Gaponov, V.M. Genkin, N.N. Salashchenko, *Nucl. Instrum. Methods Phys. Res. A* **261**, 91-98 (1987)
14. R.W. James, *The Optical Principles of the Diffraction of X-rays*, OX BOW Press, p 24, (1982)
15. E. Spiller, *Revue Phys. Appl.* **23**, 1687-1700 (1988)
16. E. Spiller, D.G. Stearns, M. Kumrey, *J. Appl. Phys.* **74**, 107-118 (1993)
17. H. Kiessig, *Ann. Phys. (Germany)* **5**, 769-788 (1981)
18. B.L. Henke, J.Y. Uejio, H.T. Yamada and R.T. Tackaberry, *Opt. Eng.* **25**, 937-947 (1986)
19. J.B. Shellan, P. Agmon, P. Yeh and A. Yariv, *J. Opt. Soc. Am.* **68**, 18-27 (1978)
20. A.D. Akhsakhalyan, A.A. Fraerman, N.I. Polushkin, Yu. Ya. Platonov and N.N. Salashchenko, *Thin Solid Films* **203**, 317-326 (1991)
21. T.M. Nagakubo, T. Yamamoto, and M. Naol, *J. Appl. Phys.* **64**, 5751-5756 (1988)
22. R. Schlatmann, J.D. Schindler and J. Verhoeven, *Physics of X-ray Multilayer Structures*, O.S.A. Technical Digest Series **6**, 122-124 (1994)
23. D.E. Savage, J. Kleiner, N. Schimke, Y.-H. Phang, T. Jankowski, J. Jacobs, R. Kariotis, and M.G. Lagally, *J. Appl. Phys.* **69**, 1411-1424 (1991)
24. B.L. Henke, E.M. Gullikson and J.C. Davis, *At. Data Nucl. Data Tables*, **54**, 181-342 (1993)
25. E. Louis, H.-J. Voorma, N.B. Koster, F. Bijkerk, Yu. Platonov, S. Yu. Zuev, S. Andreev, E. Shamov, and N. Salashchenko, *Microelectron. Eng.* **27**, 235-238 (1995)
26. R. Schlatmann, C. Lu, J. Verhoeven, E.J. Puik, M.J. van der Wiel, *Appl. Surf. Sci.* **78**, 147-157 (1994)
27. J.H. Underwood, E.M. Gullikson, and K. Nguyen, *Appl. Opt.* **32**, 6985-6990, (1993)
28. E. Louis, H.-J. Voorma, N.B. Koster, L. Shmaenok, F. Bijkerk, R. Schlatmann, J. Verhoeven, Yu. Ya. Platonov, G.E. van Dorssen and H. Padmore, *Microelectron. Eng.* **23**, 215-218 (1994)
29. E. Louis, E. Spiller, S. Abdali, F.E. Christensen, H.-J. Voorma, N.B. Koster, P.K. Frederiksen, C. Tarrío, E.M. Gullikson, and F. Bijkerk, *Proc. SPIE* **2515**, 194-203 (1995)
30. F.E. Christensen, E. Jacobsen, P. Jonasson, M.M. Madsen, H.W. Schnopper, E.H. Silver, N.J. Westergaard and P. Orup, *Proc. SPIE* **597**, 316-328 (1985)
31. A.D. Smith, M.D. Roper, H.A. Padmore, *Nucl. Instrum. Methods Phys. Res. B* **97**, 579-584 (1995)
32. N.N. Salashchenko, Yu. Ya. Platonov, S.Yu. Zuev, *Nucl. Instrum. Methods Phys. Res. A* **359**, 114-120 (1995)
33. S. Pizzini, K.J. Roberts, G.N. Greaves, N.T. Barrett, I.D. Dring and R.J. Oldman, *Proc. 2nd Workshop on Synchrotron Light: Applications and Related Techniques*, Campinas (1989)
34. F.E. Christensen, B.P. Byrnak, A. Honstrup, Z. Shou-hua, H.W. Schnopper, *Proc. SPIE*, **1744** (1990) 181



1. ...  
2. ...  
3. ...  
4. ...  
5. ...  
6. ...  
7. ...  
8. ...  
9. ...  
10. ...  
11. ...  
12. ...  
13. ...  
14. ...  
15. ...  
16. ...  
17. ...  
18. ...  
19. ...  
20. ...  
21. ...  
22. ...  
23. ...  
24. ...  
25. ...  
26. ...  
27. ...  
28. ...  
29. ...  
30. ...  
31. ...  
32. ...  
33. ...  
34. ...  
35. ...  
36. ...  
37. ...  
38. ...  
39. ...  
40. ...  
41. ...  
42. ...  
43. ...  
44. ...  
45. ...  
46. ...  
47. ...  
48. ...  
49. ...  
50. ...  
51. ...  
52. ...  
53. ...  
54. ...  
55. ...  
56. ...  
57. ...  
58. ...  
59. ...  
60. ...  
61. ...  
62. ...  
63. ...  
64. ...  
65. ...  
66. ...  
67. ...  
68. ...  
69. ...  
70. ...  
71. ...  
72. ...  
73. ...  
74. ...  
75. ...  
76. ...  
77. ...  
78. ...  
79. ...  
80. ...  
81. ...  
82. ...  
83. ...  
84. ...  
85. ...  
86. ...  
87. ...  
88. ...  
89. ...  
90. ...  
91. ...  
92. ...  
93. ...  
94. ...  
95. ...  
96. ...  
97. ...  
98. ...  
99. ...  
100. ...

## Temperature induced diffusion in Mo/Si multilayer mirrors

### 1. Abstract

To optimize the growth process of Mo/Si multilayers, the effect of an elevated substrate temperature during deposition has been studied in the temperature range between 300 K and 550 K. Multilayer properties, such as interface roughness, d-spacing, and structure of the layers, have been investigated during deposition and cool-down, after cool-down, and during heating. A number of techniques have been used: small-angle, near-normal incidence, and in-situ reflectivity measurements. It is found that the increased substrate temperature changes the interface roughness to a minimum value for samples produced at 488 K. Also a change of the d-spacing as a function of time and temperature is observed and explained by annihilation of free volume of the Si layer. The atomic structures of the layers deposited at different temperatures have been analysed with high resolution electron microscopy (TEM), which shows that both materials are amorphous for the entire temperature range investigated. At the extremes of the temperature range investigated irregular layer structures, such as ripples and V-shaped structures have been observed by TEM.

### 2. Introduction

For the production of multilayer structures the use of an elevated temperature has proven to be an advantageous technique to change the multilayer properties [1,2,3,4]. Several studies have been performed using heating of the multilayer after deposition or using an elevated temperature during deposition. Post-deposition heating has been used to achieve small corrections of the d-spacing [5], to investigate the temperature stability of the multilayer [6,7], or to investigate the structural modifications of both materials [8,9]. The elevated substrate temperature during deposition has been used to optimize the performance of Mo/Si multilayers as x-ray reflectors, by decreasing the interface roughness [10,11,12,13]. A distinction between these two techniques has to be made. During heating of a multilayer, diffusion between the layers (intermixing) and diffusion in the layers occur simultaneously,



which in most cases results in an increase of the interface roughness [5,6,9]. It will be shown that under optimized conditions the overall multilayer performance can be improved.

For some applications of multilayers the use of an enhanced substrate temperature is preferred over other additional techniques such as ion polishing, because the multilayers are more stable under intense irradiation compared to those produced at room temperature [14]. This might be important for instance for the collimating optics of a laser-plasma x-ray source as used in Extreme Ultra-Violet lithography (EUVL). For this application the optimal temperature has to be below 500 K, because higher temperatures affect the surface accuracy of most substrate materials [15]. Control of the d-spacing and interface roughness is mandatory for multilayer mirrors used in an optical system. For these multilayers the d-spacing is an even more critical parameter than the interface roughness. A change in the d-spacing of a multilayer in a multi-element optical system reduces the total throughput much more than the same relative change of the interface roughness. Despite this, the effect of an enhanced substrate temperature during deposition on the d-spacing has not been investigated.

This study is performed to investigate all multilayer parameters, including the d-spacing, as a function of deposition temperature and time. To this purpose, multilayers are investigated during deposition and cool-down, after cool-down, and during heating to their initial deposition temperature. The structures of the layers are analysed by TEM to verify the results obtained from the reflectivity measurements. A full description of the processes is presented in terms of diffusion, which completely explains the changes in the d-spacing as well as the interface roughness observed experimentally.

### 3. Experimental

#### 3.1 Coating procedure

The multilayers have been produced in an e-beam coating facility consisting of two vacuum chambers of which the lower chamber contains the multilayer materials and the e-beam evaporator and the upper chamber contains a sample holder and an in-situ reflectometer. The base pressure in both chambers is better than  $1 \times 10^{-6}$  Pa. The coating facility has been described in detail in reference 16.

During the production of the Mo/Si multilayers, we monitor the layer thickness deposited by measuring the reflectivity of N-K radiation ( $\lambda = 3.16$  nm) at an angle of  $13^\circ$  with respect to the substrate. This setting should correspond to a d-spacing of 7.8 nm.

The in-situ system is based on interference of the reflected x-ray radiation, which is observed as oscillations in the in-situ signal. This is mainly caused by the last layer deposited. For the fabrication of multilayers, the use of an in-situ reflectivity system for the control of the deposition process has particular advantages. Firstly, it enables the control of the layer

thickness during deposition, with an error of less than 1%. Secondly, the in-situ reflectivity system enables one to monitor the roughness throughout the stack, because the amplitude of the signal decreases with increasing roughness [17]. The maximum height of the reflectivity signal during deposition of one period is dependent on the d-spacing of the multilayer, the layer thickness variations, and the average interface roughness. The amount of layer thickness variations is mainly determined by the noise level of the source, which is in this case approximately 1% of the in-situ reflectivity signal. This indicates that variations of the layer thicknesses are negligible, and therefore do not affect the quality of the multilayers.

For this study a special sample holder has been constructed, containing three temperature-isolated parts, each internally heated by a quartz lamp. The temperature of each part is measured with a Chromel-Alumel thermocouple with an accuracy of  $\pm 2$  K. Nine samples are produced simultaneously at three different temperatures, in order to exclude any, although minor, run-to-run variations of the deposition process and a difference in materials sticking probability. As will be shown later, the d-spacing is a function of the deposition temperature. To obtain a stable substrate temperature during deposition, heating of the holder starts several hours before the deposition. After deposition the samples are cooled to room temperature in vacuum ( $1 \times 10^{-6}$  Pa.).

The homogeneity of the deposition process over the area of the sample holder, containing the nine samples, is measured separately. The differences in the d-spacing over the entire area are found to be  $\pm 0.5\%$ . The run-to-run reproducibility is within  $\pm 0.5\%$  [18]. The deposition rate is another parameter that might influence the multilayer quality. Therefore, the deposition rate is controlled with a quartz oscillator and kept constant at  $0.050 \pm 0.005$  nm/s for both the Mo and the Si layer during all depositions.

### 3.2 Multilayer samples

To investigate the temperature dependence of the diffusion processes accurately, we investigate an extended temperature range. However, at the higher and lower ends of the temperature range the increasing interface roughness limits the number of periods that can be deposited. Therefore, we produce three sets of Mo/Si multilayer samples of which the number of periods increases as the temperature range decreases. The first set contains 12-period multilayers produced at 21 different temperatures between 300 K and 550 K. The second set contains 24-period multilayers produced at six different temperatures between 438 K and 511 K. In this intermediate range the multilayers can be produced without a drastic increase of the interface roughness. The third set consists of three 32-period multilayers produced at 454 K, 488 K and 502 K using the same settings as the 12- and 24-period multilayers. Separate tests with the 32-period multilayers have been performed after cool-down in order to investigate the effect of heating from room temperature to the initial deposition temperature.



### 3.3 X-ray measurements

We measure the reflectivity of the 32-period samples using reflectivity scans ( $\theta$ - $2\theta$ ) and rocking scans ( $\omega$ -scans) with N-K radiation, while keeping the substrate temperature constant. The rocking scans are performed in order to check the alignment of the reflectometer. The reflectivity scans, with angles between  $11^\circ$  and  $16^\circ$ , are performed to measure the angular dependence of the reflectivity, from which a change in d-spacing can be determined. The angular resolution of the in-situ reflectometer is  $0.1^\circ$ .

During the cool-down period we measure the angular dependence of the reflectivity at a number of substrate temperatures. The first measurement is performed at the deposition temperature, ten minutes after deposition of the last layer. After a few measurements we switch off the quartz lamps to cool the substrate holder. The time needed for a complete cool-down to room temperature ranged from several to 14 hours depending on the initial substrate temperature.

After cool-down some of the samples are heated, with a heat rate similar to cooling, again to their original deposition temperature, while the angular dependence of the reflectivity is measured as a function of temperature. These samples are only used to investigate the effect of heating on the d-spacing and the interface roughness.

Small-angle reflectivity measurements ( $\theta$ - $2\theta$  scans) with Cu- $K\alpha$  radiation are used to characterize the multilayer structures in detail after deposition. A Ge crystal monochromator is used in combination with two slits, resulting in an angular resolution of better than  $0.01^\circ$  [19]. The analysis of the small-angle reflectivity measurements is based on a fast Fourier transformation of the reflectivity around the Bragg peaks [20, 21]. From this, the average interface roughness ( $\sigma_{rms}$ ), the thickness ratio ( $\Gamma$ ), and the layer thickness errors ( $\zeta$ ) are determined ( $\Gamma$  is defined as the ratio of the thickness of the high-Z material to the d-spacing).

Mo/Si multilayers are mainly investigated for the use in Extreme UV lithography, an application for which the reflectivity at near normal incidence is of paramount importance. Therefore, we also measured the near-normal incidence reflectivity. The angular dependence of the reflectivity of the 12-period multilayers is measured using a conventional electron impact x-ray source using the Si-L line (13.55 nm) (the Institute for Physics of Microstructures) [22]. The 24- and 32-period multilayers are measured at wavelengths between 12.4 nm and 16 nm using an undulator beam line with a plane grating monochromator (user station 5U1 of the Daresbury synchrotron of the SRC) [23]. Both reflectivity measurements have a relative error of 1% from sample to sample and an error of  $\pm 2.5\%$  of the absolute reflectivity value.

### 3.4 High resolution transmission electron microscopy (TEM)

TEM analysis is performed to investigate the structure of both materials, and to obtain a qualitative analysis of the change in the interface roughness. For these measurements ultra thin cross sections of the multilayers are prepared by a two-step process of mechanical polishing [24] followed by ion milling. The ion milling is performed using 5.0-3.5 kV Ar ions at respectively 20° and 12° angle of incidence with respect to the substrate. The measurements are performed with a Philips CM30T using an accelerator voltage of 300 kV. The pictures show bright field images and are taken with the interfaces in the edge on position.

## 4. Results and discussion

### 4.1 Interface roughness

A first assessment of the useful temperature range for the production of Mo/Si multilayers is given by the quality of the in-situ reflectivity signal. As an example three in-situ reflectivity signals of 12-period multilayers, produced at 311 K, 488 K, and 538 K, are shown in Figure 1. The main difference between these reflectivity signals is the amplitude, which decreases after a few periods for the multilayers produced at 311 K and 538 K. This indicates that the search for optimum conditions narrows down to the range between 311 K and 538 K.

A quantitative investigation of the interface roughness as a function of temperature, is obtained from the analysis of small-angle reflectivity measurements. The results, shown in Figure 2, demonstrate that the roughness of the 12-period multilayers is minimal ( $0.33 \text{ nm}$ ) at a substrate temperature of  $488 \pm 2 \text{ K}$ . This temperature dependence of the interface roughness suggests that at least two processes determine the interface roughness. The first process

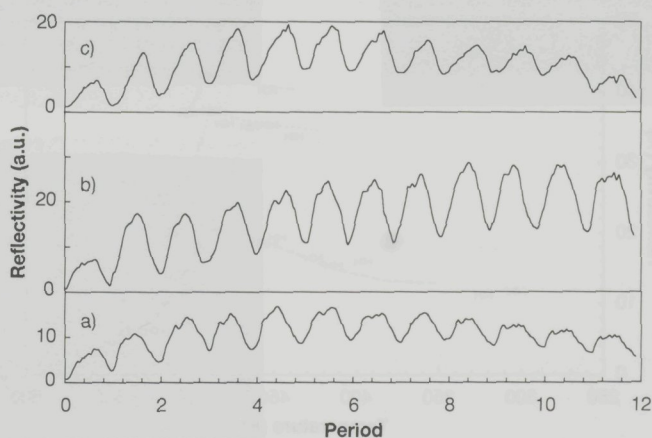


Figure 1: In-situ reflectivity as function of the deposition time of multilayers produced at a) 311 K, b) 488 K, and c) 538 K.



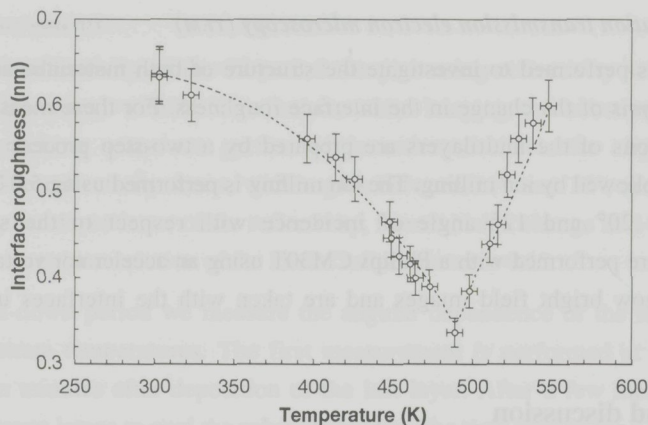


Figure 2: Measured interface roughness as a function of temperature. The line represents an arbitrary fit through the data.

dominates at temperatures below 488 K, and consists of surface diffusion induced smoothening. The second process dominates above 488 K and causes roughening. In section 4.1 this will be explained in detail.

The roughness increases towards the limits of the temperature range and the near-normal incidence reflectivity shows a maximum at 488 K (Figure 3). This maximum coincides with the minimum of the interface roughness in Figure 2. However, the reflectivity is not only dependent on the interface roughness, but also on the structure, the density, or contamination of the layers. In previous work we have reported a 5% content of oxygen in the Si layer for multilayers produced at elevated substrate temperatures [25]. The theoretical reflectivity of a

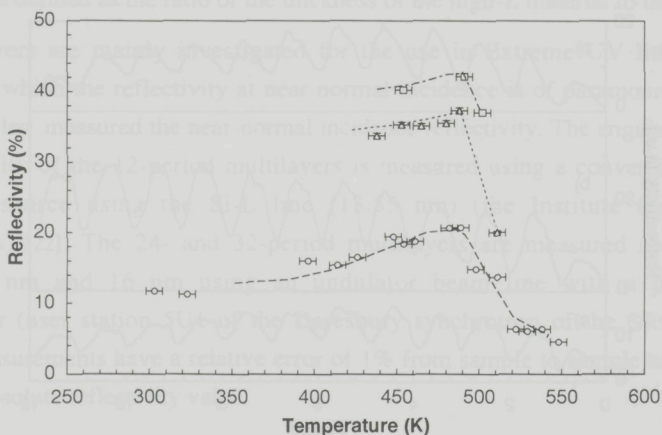


Figure 3: Near-normal incidence reflectivity of the 12- (○), 24- (△), and 32-period (□) multilayers for 13.5 nm radiation. The lines are used to guide the eye.

12-period multilayer with a d-spacing of approximately 7.4 nm is 19%, taking into account the 5% oxygen and a roughness of 0.33 nm. This reflectivity is consistent with the 19% measured for the sample produced at 488K. For the samples deposited at low (< 388 K) and high (> 511 K) temperatures, the measured reflectivity is lower than the theoretical value. We suggest that in this case at least one of the materials of the multilayers has a morphology, which differs from the multilayers produced at the optimal temperature. Hence, the influence of the roughness on the reflectivity cannot be described with the Debye-Waller factor, for which a Gaussian distribution of the atoms at the interface is presumed.

In order to investigate the material structure, three samples produced at three different temperatures (388 K, 478 K, and 511 K) have been analysed with TEM (Figure 4a, b and c). In the pictures the light areas represent Si and the dark areas Mo. The thickness of the Mo layer is not represented correctly because of an interference effect. Between these samples large differences are observed in the interface roughness. We distinguish three types of interface roughness: ripples, V-shaped structures, and intermixing. The ripples are caused by columnar growth, which occurs in amorphous materials with a high melting point and a high covalence, such as Mo and Si [26]. For the sample deposited at 388 K, the ripples are copied from one layer to the next layer, indicating a strong correlation of the roughness between the layers. The ripples decrease with increasing temperature. The typical V-shaped structures, are only

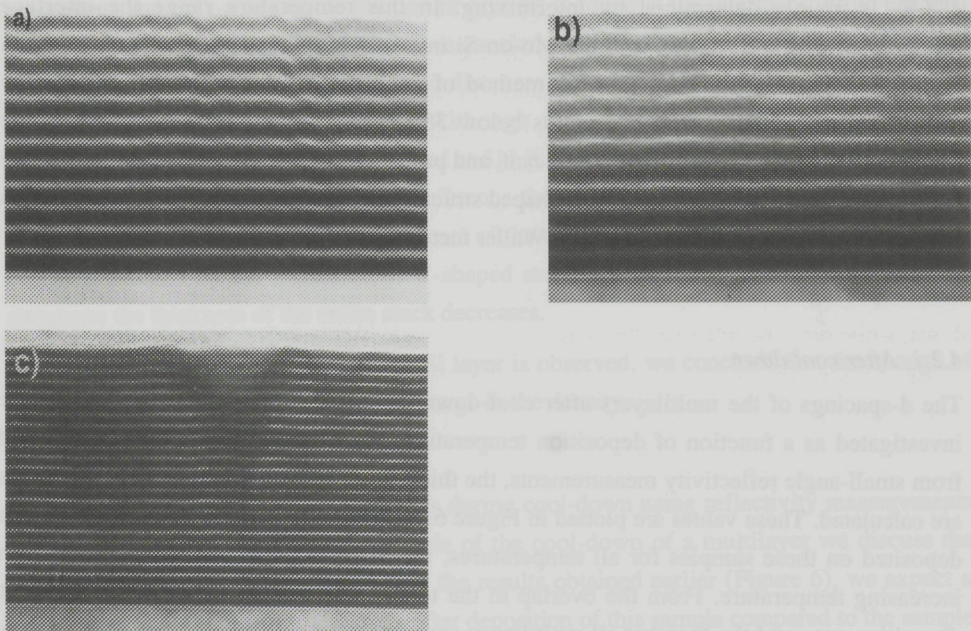


Figure 4: TEM pictures of Mo/Si multilayers produced at different temperatures: a) 388 K, b) 478 K c) 511 K.



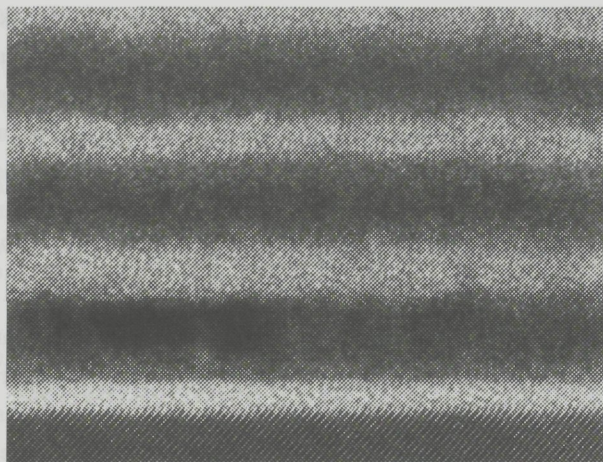


Figure 5: An enlargement of the TEM picture from the multilayer in Figure 4b, in which the equal roughness of the Si-on-Mo and the Mo-on-Si interface is observed.

observed in the samples deposited at 511 K (Figure 4c). This phenomenon is also observed after heating of a multilayer [26], in which it is demonstrated that the sizes of these V-shaped structures increase with temperature, and finally results in voids. From the TEM analysis we conclude that the interface roughness, for the samples deposited around the optimum at 488 K, is mainly determined by intermixing. In this temperature range the interface roughnesses of the Si-on-Mo and the Mo-on-Si interface are equal, as can be observed in Figure 5. This also indicates that the method of analysis of the small angle reflectivity measurements is valid. At temperatures below 388 K and above 511 K the effect of the ripples and V-shaped structures is significant, and probably increases towards the limits of the temperature range investigated. The V-shaped structures and ripples also limit the description of the interface roughness by the Debye-Waller factor.

## 4.2 D-spacing

### 4.2.1 After cool-down

The d-spacings of the multilayers after cool-down, i.e. several hours after deposition, are investigated as a function of deposition temperature. From the d-spacing and  $\Gamma$ , obtained from small-angle reflectivity measurements, the thicknesses of both the Si and the Mo layers are calculated. These values are plotted in Figure 6. Although the same amount of material is deposited on these samples for all temperatures, the Si layer thickness is decreasing with increasing temperature. From the overlap in the temperature ranges between the different deposition runs and the fact that all multilayers are monitored at different temperatures, it is concluded that the sticking probability of the materials is the same for the entire temperature

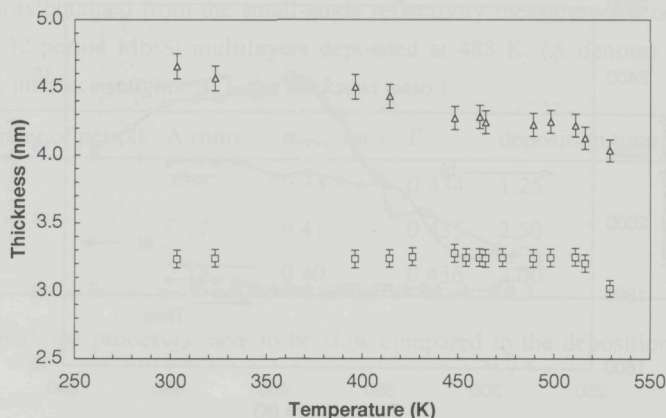


Figure 6: Thickness of the Mo ( $\square$ ) and Si ( $\Delta$ ) layer as a function of temperature

range. Therefore, a difference should be observed in either the density of the multilayers or the structure, or both.

A small decrease of the thickness of the Mo layer is observed in the multilayer deposited above 515 K. We have investigated whether this could be caused by crystallization and/or the formation of Mo/Si compounds, because these generally have a smaller volume than the amorphous materials. TEM analysis (Figure 4) shows that all the layers are mainly amorphous and only a negligible fraction of crystals is found at the interfaces. From electron diffraction measurements using the TEM, we conclude that these crystals are neither Mo nor Si crystals, but possibly a silicide. The bond distances (0.213, 0.217, and 0.227) coincide with the distances for  $\text{MoSi}_2$  and  $\text{Mo}_5\text{Si}_3$ . Although the fraction of crystals increases with temperature, even for the sample deposited at 511 K, the total fraction is found to be less than 1%. Therefore, crystallization will not influence the reflectivity nor the layer thicknesses of the multilayers. We suggest that the decrease of the effective Mo layer thickness above 515 K can be explained by the formation of V-shaped structures as shown in Figure 4c. In these structures the thickness of the entire stack decreases.

Since no change in the structure of the Si layer is observed, we conclude that the change of the Si layer thickness must be due to a change in the density.

#### 4.2.2 During cool-down

We monitor the d-spacing of the samples during cool-down using reflectivity measurements with N-K radiation. As a typical example of the cool-down of a multilayer we discuss the sample deposited at 488 K. Considering the results obtained earlier (Figure 6), we expect a 10% decrease of the Si-layer thickness after deposition of this sample compared to the sample produced at room temperature. The result of the N-K reflectivity measurements for the sample produced at 488 K is shown in Figure 7. The graph shows the reflectivity and the



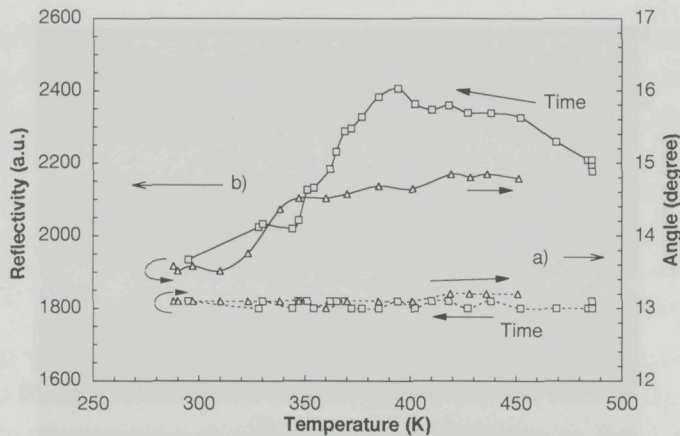


Figure 7: Reflectivity measurements during cool-down and heating. Both curves are obtained from angular scans with N-K radiation as a function of temperature during cool-down ( $\Delta$ ) and heating ( $\square$ ) afterwards. a) Angle where maximum reflectivity is obtained. b) Reflectivity of the multilayer.

angle where maximum reflectivity is obtained during cool-down and heating of the multilayer. From Figure 7 we conclude that the d-spacing does not change during this period, because the maximum reflectivity is obtained at a constant angle, independent of the temperature. However, the value of the reflectivity decreases during cool-down at constant d-spacing, while during heating the reflectivity increases to the value measured just after deposition, i.e. before cool-down again at constant d-spacing. This indicates that the changes in the reflectivity are not caused by a change of the interface roughness, because diffusion processes are not reversible. The decrease of reflectivity with temperature is explained by the presence of oxygen, probably caused by water absorption of the surface. The analyses of the reflectivity data show that 5 atom layers of oxygen are sufficient to explain the decrease in reflectivity. This process is reversed when the temperature is increased again.

The small angle reflectivity measurements show that the d-spacing has changed after cool-down, while we conclude from the N-K reflectivity measurements that the d-spacing does not change during cool-down. This implies that the d-spacing changes even before cool down, namely during the deposition process.

#### 4.2.3 During deposition

The use of an in-situ reflectivity signal is the most appropriate technique to investigate the change of the Si-layer thickness during deposition. However, as explained earlier, the in-situ reflectivity signal can be influenced by the average interface roughness as well as the d-spacing of the stack. The thickness of the stack investigated is limited by the penetration depth of the N-K radiation. Only the upper 80 nm ( $\sim 10$  periods) of these Mo/Si multilayers will be probed. In order to investigate the diffusion processes in a multilayer with the in-situ

Table I: Results obtained from the small-angle reflectivity measurements of the 12-, 24-, and 32-period Mo/Si multilayers deposited at 488 K. ( $\Lambda$  denotes the d-spacing,  $\sigma_{\text{rms}}$  interface roughness,  $\Gamma$  the thickness ratio.)

number of period	$\Lambda$ (nm)	$\sigma_{\text{rms}}$ (nm)	$\Gamma$	deposition time (h)
12	7.46	0.34	0.434	1.25
24	7.22	0.41	0.435	2.50
32	7.15	0.40	0.436	3.00

reflectivity signal, the processes have to be slow compared to the deposition time for one layer (70 s).

A possible change of the in-situ reflectivity signal by roughness can be excluded based on the following argument. As an example, the in-situ reflectivity of the 32-period multilayer deposited at 488 K is analysed, and displayed in Figure 8. From this data, the amplitude of the in-situ reflectivity for each layer is calculated, and also shown in Figure 8. The amplitude of the in-situ signal is constant for each period after the first 12 periods, indicating a constant roughness throughout the stack [27]. The 12-, 24- and 32-period multilayers produced at 488 K are also analysed with small-angle reflectivity measurements. These results are listed in Table I and show that the 24- and 32-period Mo/Si multilayers have equal interface roughnesses (0.4 nm). This is the second indication that the roughness is constant throughout the stack [28]. Therefore, the decrease of the in-situ reflectivity after the 12<sup>th</sup> period can only be caused by a change of the Si layer thickness just after deposition. In section 5.2 we continue the discussion of the time dependence of the change of the d-spacing in terms of diffusion.

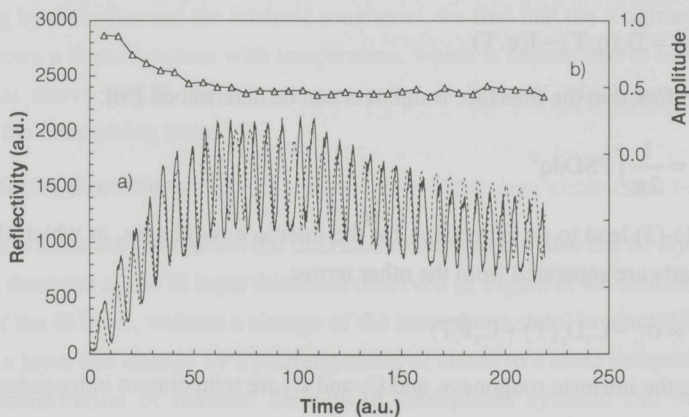


Figure 8: a): Measured (solid line) and simulated (dotted line) in-situ reflectivity for a 32-period multilayer deposited at 488 K. b): Calculated amplitudes ( $\Delta$ ) for each period.



## 5. Diffusion processes

In temperature dependent deposition processes, diffusion is likely to play a major role. As will be demonstrated, all phenomena described so far can be explained by diffusion.

### 5.1 Type of diffusion

In order to explain the change of the interface roughness in terms of diffusion, a growth model is adopted [29]. In the growth model the power spectral density function (PSD) of the interface is described by spatial frequency ( $q$ ) and temperature ( $T$ ) dependent smoothing ( $D_s(q,T)$ ) and roughening terms ( $I(q,T)$ ), and the power spectral density of the substrate ( $PSD_{SUB}$ ). In this case we are interested in the temperature dependence of the total interface roughness and not in the spatial frequency dependence of the interface roughness of each layer in the multilayer. The factor  $D_s(q,T)$  consist of a viscous flow and a diffusion term, which both have the same temperature dependence. The difference between these two terms is the spatial frequency dependence. It is noted that determination of the spatial frequency dependence of both  $D_s(q,T)$  and  $I(q,T)$  in Eq. (2), would result in information on the lateral distribution of the interface roughness. In general the term  $D_s(q,T)$  consists of a diffusion term, which affects the large spatial frequency region, and a viscous flow term, which dominates in the small spatial frequency region. The PSD of one layer is given by:

$$PSD(q) = PSD_{sub}(q) \exp[-b(q)t] + \alpha \frac{[1 - \exp\{-b(q)t\}]}{b(q)} \quad (1)$$

where  $t$ : the diffusion time (s)

$\alpha$ : a Poisson like term, which describes the increase of the interface roughness by a random arrival of atoms during deposition

The function  $b(q)$  corresponds to the rate of relaxation of a layer, and is given by:

$$b(q) = D_s(q,T) - I(q,T) \quad (2)$$

From the PSD function the interface roughness can be determined [30]:

$$\sigma^2 = \frac{1}{2\pi} \int PSD dq^2 \quad (3)$$

Equations (1)-(3) lead to an expression for the interface roughness, in which the temperature dependent parts are separated from the other terms:

$$\sigma^2 \propto \sigma_i^2 - C_1 D_s(T) + C_2 I(T) \quad (4)$$

in which  $\sigma_i$  is the intrinsic roughness, and  $C_1$  and  $C_2$  are temperature independent constants.

The first term in Eq. (4) is the intrinsic roughness of a layer caused by the growth of the layer with a certain thickness. The intrinsic roughness is determined by the random arrival of atoms

at an interface during deposition, and is for these layer thicknesses determined to be 0.67 nm. The second term is the change in roughness caused by diffusion. The third term is the change in roughness caused by intermixing. We already concluded from Figure 2, that at temperatures below 488 K the diffusion dominates, while above 488 K intermixing is the dominating process.

Since all materials are amorphous, the diffusion coefficient is described by an Arrhenius-type behaviour. Analogously to Ref. 29,  $D_s(T)$  is determined to be:

$$D_s(T) = \frac{1}{2kT} \exp\left(\frac{-E_g}{kT}\right) \quad (5)$$

where  $k_B$ : Boltzmann constant (eV/K)  
 $E_g$ : activation energy (eV)

For temperatures below 488 K the effect of intermixing is negligible. Below 488 K the change of the interface roughness ( $\Delta\sigma_{rms}$ ) can be written as a function of temperature, using the exponential term of Eqs (4) and (5), which results in:

$$\Delta\sigma_{rms}^2 = |\sigma_i^2 - \sigma_{rms}^2(T)| \sim \frac{1}{k_B T} \exp\left(\frac{-E_g}{k_B T}\right) \quad (6)$$

in which  $\sigma_i$  is the intrinsic roughness, which is determined to be 0.67 nm.

A least squares fit to Eq. (6) is made, using the experimental data of Figure 2. The activation energy ( $E_g$ ) found in this way amounts to  $0.18 \pm 0.02$  eV for the temperature range from 300 K to 488 K. The value for the activation energy indicates that surface diffusion is the dominant type of diffusion. Our results confirm the results described in Ref. 12, which is restricted to near normal incidence reflectivity measurements. Taking into account the effect of smoothening by diffusion and the intrinsic roughness, we find that the roughness caused by intermixing shows a linear increase with temperature, which is determined to be 0.007 nm/K. It is noted that above 488 K the temperature range is limited, which introduces some uncertainty of the intermixing term.

## 5.2 Annihilation of free volume

Surface diffusion does not only affect the interface roughness but also the Si layer thickness. To explain the decrease of the Si layer thickness observed in Figure 6, we assume a change of the structure of the Si layer, without a change of the amorphous state. In amorphous materials the volume of a layer can change by a rearrangement of atoms to a more compact amorphous structure by annihilation of defects. Defects in amorphous systems can be calculated analogously to the general theory of substitutional diffusion in crystalline solids by a random walk theory. This is described in the free volume model, which we use to interpret the volume change of the Si layer [31].



The free volume of a layer is determined from the diffusion coefficient for amorphous solids. This diffusion coefficient is given by [32]:

$$D(T) = a\lambda_d^2 c_f(T) k_{d,0} \exp\left(\frac{-E_d}{k_B T}\right) \quad (7)$$

where  $a$ : geometrical constant (normally taken equal to 1/6 [32])  
 $\lambda_d$ : diffusional jump distance  
 $c_f$ : the fraction of flow defect concentration  
 $k_{d,0}$ : attempt frequency for diffusion defects  
 $E_d$ : activation energy for the movement of diffusion defects.

The fraction of flow defect concentration ( $c_f$ ) is related to the fractional free volume ( $v_f$ ) according to:

$$c_f = \exp\left(\frac{-\gamma v}{v_f(T)}\right) \quad (8)$$

where  $\gamma$ : geometrical factor ( $\gamma v = 0.1$ ) [33]  
 $v$ : critical free volume (per average atomic volume) needed for a jump  
 $v_f$ : average free volume (per average atomic volume).

Equations (7) and (8) show that diffusion affects the free volume of a layer, and therefore, changes the volume of that layer. Such a volume change results in a change of the d-spacing of the multilayer, because it is rigidly fixed to the substrate and therefore, does not allow lateral contraction or expansion.

### 5.2.1 Free volume, temperature dependence

Using the experimental data of Figure 6, the change in the free volume of the Si layer as a function of temperature can be determined using:

$$\frac{\Delta d}{d} = \frac{d(T_0) - d(T)}{d(T_0)} = \Delta v_f = v_f(T_0) - v_f(T) \quad (9)$$

The change in free volume is determined from Eq. (9) combined with Eqs (7) and (8):

$$\Delta v_f = v_f(T_0) + \gamma v \left( \frac{k_B T}{E_g - E_d} \right) \quad (10)$$

Equation (10) shows that the change in free volume is linearly proportional to the temperature. Using the measured thicknesses of the Si layer (Figure 6), a linear least squares fit of Eq. (10) is made, yielding a value for the free volume at room temperature of  $0.16 \pm 0.02$ . The free volume decreases with increasing temperature to 0.02 at a temperature of 550 K. Apparently, the Si structure deposited at room temperature has many vacancies.

From the fit also the value for the difference in the energies ( $E_g - E_d$ ) is obtained, which amounts to 0.03 eV. With  $E_g$  being determined from the roughness measurements, the value of  $E_d$  is found to be 0.25 eV for temperatures below 488 K. As expected from Eq. (7), the activation energy for the motion of diffusion defects is almost similar to the value found for the activation energy of the diffusion coefficient for individual atoms. Surface diffusion is the dominant process for the change of the d-spacing as has been concluded in section 4.2.1. We summarize that surface diffusion causes the change in d-spacing, because of the annihilation of free volume in the Si layers.

### 5.2.2 Free volume, time dependence

In this section the time scale of the annihilation of defects is investigated. We determine the moment the thickness of the Si layer changes and calculate the decrease of the free volume as a function of time. This is used to calculate the in-situ reflectivity signal and to compare this with the measured in-situ reflectivity. The diffusion coefficient changes if the free volume changes. Since the free volume is time dependent, this can be used to implicitly rewrite the diffusion coefficient into a time dependent diffusion coefficient:

$$D(t)^{-1} = D(t_0)^{-1} + At \quad (11)$$

where  $A$ : only dependent on the temperature.  
 $t_0$ : taken 0 at the moment just after deposition.

The relation between the change in free volume and time is found using Eqs. (7), (8), and (11):

$$\frac{\Delta d}{d} = v_f(t_0) - v_f(t) = v_f(t_0) \times \left\{ 1 - \left( 1 + \frac{v_f(t_0)}{v_f} \ln[1 + AD(t_0)t] \right)^{-1} \right\} \quad (12)$$

Equation (12) is used to fit the calculated in-situ reflectivity signal to the measured one (Figure 8) using  $v_f(t_0)$  and  $AD(t_0)$  as fitting parameters. This results in a value of  $0.020 \text{ s}^{-1} \pm 0.005 \text{ s}^{-1}$  for  $AD(t_0)$  and  $0.17 \pm 0.02$  for  $v_f(t_0)$ . The latter value coincides with the value of 0.16 for the free volume at room temperature found in the previous section. This indicates that the structure at room temperature hardly changes by diffusion.

In Figure 8 the measured in-situ reflectivity of the 32-period multilayer is plotted together with the calculated in-situ reflectivity signal using the time dependence of the thickness of the Si layers described above. As can be concluded from Figure 8 the time dependence of the d-spacing of Eq. (12) fits the measured in-situ reflectivity signal. The small deviations between the calculated and the measured in-situ reflectivity are caused by small layer thickness errors, a small variation of the deposition speed, and the time needed for changing the materials during deposition.



The value for  $AD(t_0)$  determines the time scale of the diffusion process. The relative change of the Si layer thickness as a function of time is calculated using Eq. (12), using the values found earlier for  $AD(t_0)$  and  $v_r$ . For the multilayer deposited at 488 K we find that the decrease in the Si layer thickness occurs within  $1000 \pm 100$  seconds. This decrease can be measured using the in-situ reflectivity signal, given the deposition speed of 0.05 nm/s. After 1000 seconds less than five periods are deposited, while the penetration depth is almost ten periods. The fact that the deposition time for a single layer (70 s) is relatively short as compared to the relaxation time, confirms the assumption that the Si layer does not change during deposition.

A qualitative comparison can be made between the samples treated with post deposition heating and those deposited at an elevated substrate temperature. The value for  $AD(t_0)$  ( $0.02 \text{ s}^{-1}$ ) found in this study is twice the value ( $0.01 \text{ s}^{-1}$ ) that has been found for isothermal annealing at 488 K of a Mo/Si multilayer with a d-spacing of 0.8 nm made with sputter deposition [34]. This indicates that the time needed for the change in the d-spacing of the Mo/Si multilayers investigated in this paper is shorter than the time needed for the given sample made with sputter deposition. The difference in relaxation speed is explained by the lower free volume ( $< 0.02$ ) found for layers made with sputter deposition.

### 5.3 Model

Combining the results obtained above, we formulate a phenomenological model of the growth mechanisms of Mo/Si multilayers produced at elevated substrate temperatures. The growth model is depicted in Figure 9.

Both materials are amorphous in the entire temperature range. The Si layers deposited at room temperature have an open structure. Deposition of Mo on a Si layer at room temperature results in a high interface roughness, because the Mo atoms are embedded into the open Si structure. TEM analyses of samples produced at 388 K show that the structure has many ripples, which are copied from one layer to another. The interface roughness is mainly determined by these ripples. At room temperature diffusion is negligible, and therefore, the d-spacing does not change during or after deposition. This is confirmed by the fact that the free volume as deposited (0.17, calculated from the in-situ reflectivity signal) is almost equal to the free volume at room temperature (0.16) calculated from the changes in Si layer thickness as a function of temperature.

Increasing the temperature to the optimal value of 488 K, one finds that the layers become smoother and the d-spacing decreases. At a temperature of 488 K the layers are relatively smooth before the next layer is deposited. Surface diffusion changes the interface roughness as well as the d-spacing. In the range around the optimal temperature, between 388 K and 511 K, the interface roughness is determined by intermixing, while the roughness at the Si-

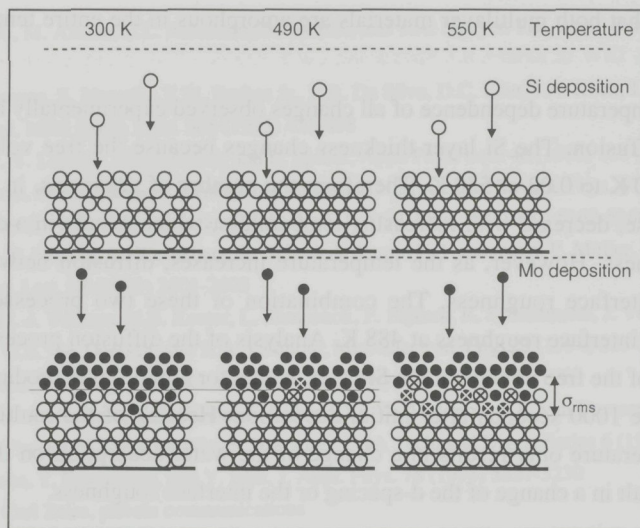


Figure 9: Schematic representation of the proposed mechanism of growth and the effect on the interface roughness as a function of temperature. Si atoms are indicated with white dots, Mo atoms with black dots, and diffused atoms are marked with a cross. Although for clarity a regular structure is drawn, it is noted that both materials are in practice in an amorphous state.

on-Mo interface and the Mo-on-Si interface is equal. The decrease of thicknesses of the Si layers with increasing temperature is caused by annihilation of free volume.

Around 511 K the roughness is mainly determined by V-shaped structures and intermixing. The Si layer decreases further, and above 515 K the Mo layer also decreases. From TEM analysis we conclude that the latter is caused by the formation of the V-shaped structures, and the entire thickness of the structure decreases.

## 6. Conclusions

In order to optimize the performance of Mo/Si multilayers as soft x-ray reflectors, the use of an elevated substrate temperature during deposition has been studied extensively in the temperature range between 300 K and 550 K. Both the interface roughness and the Si layer thickness, and thus the d-spacing of the multilayer, are influenced by the substrate temperature. A minimum in the interface roughness of 0.33 nm has been found at 488 K, which would result in a 63% reflectivity for a 40-period multilayer mirror, extrapolating the experimental result of the 12-period sample. The Si layer thickness has been found to decrease continuously with increasing temperature. A decrease of 10% has been measured for the sample deposited at 488 K compared to samples deposited at room temperature. TEM



analysis shows that both multilayer materials are amorphous in the entire temperature range investigated.

The time and temperature dependence of all changes observed experimentally have been fully described by diffusion. The Si layer thickness changes because the free volume decreases from 0.16 at 300 K to 0.02 at 550 K. Therefore, the number of vacancies, in which the Mo atoms can diffuse, decrease with increasing temperature, which results in a decrease of the interface roughness. However, as the temperature increases, diffusion between the layers increases the interface roughness. The combination of these two processes results in a minimum in the interface roughness at 488 K. Analysis of the diffusion process also yields a relaxation time of the free volume of the Si layer, which for a multilayer produced at 488 K is determined to be 1000 seconds after initial deposition. Heating of the multilayers to their deposition temperature only results in a change of the water absorption on the top surface, and does not result in a change of the d-spacing or the interface roughness.

It has been shown that high reflectivity Mo/Si multilayers can be produced using a substrate temperature of 488 K. This temperature is not expected to affect the surface accuracy of the substrates, but more research is needed. Nevertheless, further investigation is needed to assess the long term stability of multilayers produced with this method, when exposed to intense x-ray sources, such as a laser plasma source, a high brightness synchrotron, or an undulator.

## 7. Acknowledgements

We acknowledge the contribution of Yu.Ya. Platonov (Institute for Physics of Microstructures, Nizhny Novgorod, Russia, presently at Osmic, Troy, USA) on doing the reflectivity measurement. F. Tichelaar, B. Sprong (the National Centre for HREM at the Delft University of Technology, The Netherlands), and R. Koper (the FOM-Institute for Atomic and Molecular Physics, Amsterdam, The Netherlands) are acknowledged for the investigations by electron microscopy and TEM sample preparation. We also acknowledge the use of the reflectometer made available by G.E. van Dorssen and M. Roper (Daresbury SRS, Warrington, United Kingdom). This research within the framework of FOM (the Foundation for Fundamental Research on Matter) is supported by STW (the Netherlands Technology Foundation) and the Dutch Government in the context of EUREKA.

## 8. References

1. V. Dupuis, M.F. Ravet, C. Tête, M. Piecuch, Y. Lepêtre, R. Rivoira, and E. Ziegler, *J. Appl. Phys.* **68** (1990) 5146-5154
2. A.F. Jankowski, L.R. Schrawyer, and M.A. Wall, *J. Appl. Phys.* **68** (1990) 5162-5168
3. E.J. Puik, S.W.M. van de Ven, W.J.J. Wolfis, G.E. van Dorssen, and M.J. van der Wiel, *Proc. SPIE* **1547** (1991) 221-227
4. H. Takenaka, T. Kawamuro, and Y. Ishii, *J. Appl. Phys.* **78** (1995) 5227-5230

5. Y. IJdiyaou, M. Azizan, E.L. Ameziane, M. Brunel, and T.A. Nguyen Tan, *Appl. Surf. Sci.* **55** (1992) 165-171
6. B.J. Macgowan, S. Mrowka, T.W. Barbee Jr., L.B. Da Silva, D.C. Eder, J.A. Koch, J.A. Turner, and J.H. Underwood, *MRS Symp. Proc.* **306** (1993) 432-438
7. E. Ziegler, Y. Lepetre, I.K. Schuller, and E. Spiller, *Appl. Phys. Lett.* **48** (1986) 1354-1356
8. D.G. Stearns, M.B. Stearns, Y. Cheng, J.H. Stith, and N.M. Ceglio, *J. Appl. Phys.* **67** (1990) 2415-2427
9. A.F. Jankowski, L.R. Schrawyer, and M.A. Wall, *J. Appl. Phys.* **68** (1990) 5162-5168
10. A. Kloidt, K. Nolting, U. Kleineberg, B. Schmiedeskamp, U. Heinzmann, P. Müller, and M. Kühne, *Appl. Phys. Lett.* **58** (1991) 2601-2603
11. E. Louis, H.-J. Voorma, N.B. Koster, L. Shmaenok, F. Bijkerk, R. Schlattmann, J. Verhoeven, Yu. Ya. Platonov, G.E. van Dorssen, and H.A. Padmore, *Microelectron. Eng.* **23** (1994) 215-219
12. M.B. Stearns, C. Chang, and D.G. Stearns, *J. Appl. Phys.* **71** (1992) 187-198
13. E. Louis, H.-J. Voorma, N.B. Koster, F. Bijkerk, Yu. Ya. Platonov, G.E. van Dorssen, and H.A. Padmore, *Physics of X-ray Multilayer Structures*, OSA Technical Digest Series **6** (1994) 35-38
14. H. Takenaka, T. Kawamuro, and Y. Ishii, *J. Appl. Phys.* **78** (1995) 5227-5230
15. G. Ittner, Carl Zeiss, private communications
16. N.B. Koster, H.-J. Voorma, and E. Louis, *Nevac* in print (1996) (in Dutch)
17. The amplitude is defined as the increase of the reflectivity during deposition of a high-Z material, normalized to the reflectivity before the deposition of that layer.
18. Nowadays, a 0.1% reproducibility is obtained because of hardware improvements in the in-situ reflectometer.
19. A.D. Akhsakhalyan, A.A. Fraerman, N.I. Polushkin, Y.Y. Platonov, and N.N. Salashchenko, *Thin Solid Films* **203** (1991) 317
20. H.-J. Voorma, E. Louis, N.B. Koster, F. Bijkerk, and M.J. v.d. Wiel, *Physics of X-ray Multilayer Structures*, OSA Technical Digest Series **6** (1994) 134-137
21. H.-J. Voorma, E. Louis, N.B. Koster, F. Bijkerk, and E. Spiller Submitted to *J. Appl. Phys.*
22. N.N. Salashchenko, Yu. Ya. Platonov, and S.Yu. Zuev, *Nucl. Instrum. Methods Phys. Res. A* **359** (1995) 114-120
23. M.D. Roper, G. v.d. Laan, J.V. Flaherty, and H.A. Padmore, *Rev. Sci. Instrum.* **63** (1992) 1482
24. R. Koper from the Surface Preparation Laboratory at the FOM-institute for Atomic and Molecular Physics in Amsterdam.
25. H.-J. Voorma, G.E. van Drossen, E. Louis, N.B. Koster, A.D. Smith, M.D. Roper, and F. Bijkerk, *Appl. Surf. Science* **93** (1996) 221-230
26. M. Niibe, M. Haysashida, T. Iizuka, A. Miyake, Y. Watanabe, R. Takahshi, and Y. Fukuda, *Proc. SPIE* **1343** (1990) 2-13
27. The increase of the amplitude of the in-situ reflectivity during the first 12 periods of the multilayer is caused by an increasing number of layers that contribute to the reflectivity.
28. The results in Table I show an insignificant increase of the interface roughness of the 24- and 32-period samples compared to the 12-period sample, but this will hardly influence the amplitude of the in-situ reflection between the 12<sup>th</sup> and 24<sup>th</sup> period.
29. E. Chason and T.M. Mayer, *Appl. Phys. Lett.* **62** (1993) 363-365 and E. Chason, T.M. Mayer, B.K. Kellerman, D.T. McIlroy and A.J. Howard, *Phys. Rev. Lett.* **72** (1994) 3040-3043
30. D.G. Stearns, *Appl. Phys. Lett.* **62** (1993) 1745-1747
31. F. Spaepen, in: *Physics of Defects*, edited by R. Balien, M. Kléman, J.-P. Poirer, Les Houches Lectures XXXV (North-Holland, Amsterdam, 1981), 136
32. F. Spaepen, *Acta Metall.* **25** (1977) 407



- 33. G.J. Leusink and A. van den Beukel, *Acta. Metall.* **36** (1988) 3019
- 34. O.B. Loopstra, Th.H. de Keijser, E.J. Mittemeyer, and S. Radelaar, *Vide Couches Minces (France)* **236** (1987) 71-73

## Angular and energy dependence of ion bombardment of Mo/Si multilayers

### 1. Abstract

The process of ion bombardment is investigated for the fabrication of Mo/Si multilayer x-ray mirrors using e-beam evaporation. The ion treatment is applied immediately after deposition of each of the Si layers to smoothen the layers by removing an additional thickness of the Si layer. In this study the parameters of Kr<sup>+</sup> ion bombardment have been optimized within the energy range 300 eV to 2 keV and an angular range between 20° and 50°. The optimization is performed by varying the angle from 20° to 50° and the ion energy from 300 eV to 2 keV. The optical performance of the Mo/Si multilayers is determined by absolute measurements of the near-normal-incidence reflectivity at 14.4 nm wavelength. The multilayer structures are analysed further with small-angle reflectivity measurements using both specular reflectivity and diffuse x-ray scattering. The optimal smoothening parameters are obtained by determining the effect of ion bombardment on the interface roughness of the Si layer. The optimal conditions are found to be 2 keV at 50° angle of incidence with respect to the surface. These settings result in 47% reflectivity at 85° ( $\lambda = 14.4$  nm) for a 16-period Mo/Si multilayer mirror, corresponding to an interface roughness of 0.21 nm rms. Analysis shows that the interface roughness is determined by ion induced viscous flow, an effect which increases with ion energy as well as angle of incidence. In order to determine the effect of intermixing of the Si and Mo atoms, the penetration depth of the Kr<sup>+</sup> ions is calculated as a function of ion energy and angle of incidence. Furthermore, the angular dependence of the etch yield, obtained from the in-situ reflectivity measurements, is investigated in order to determine the optimal ion beam parameters for the production of multilayer mirrors on curved substrates.

### 2. Introduction

Roughness of the interfaces determines to a considerable extent the reflectivity of multilayer soft x-ray mirrors. If the mirrors are produced with e-beam evaporation, additional techniques, such as ion bombardment, can be used to reduce the interface roughness. The



ability to use these techniques rather independently of the primary deposition process, is considered to be an advantage over other deposition techniques such as sputter deposition. Optimization of the deposition process as well as modification of the interface roughness by ion bombardment can be performed independently. A similar combination of two separate processes for deposition and modification of the interfaces is applied in dual ion-beam deposition [1,2].

Multilayer mirrors produced with e-beam deposition in combination with ion bombardment show a reduced interface roughness [3,4]. During the last few years several ions have been investigated ( $\text{Ar}^+$ ,  $\text{Kr}^+$ ) [5,6]. Other ions, such as  $\text{H}^+$  and  $\text{N}^+$ , have been used to modify the chemical composition of the layers [7].

For the fabrication of Mo/Si multilayers  $\text{Kr}^+$  has been found to result in a better reduction of the interface roughness compared to  $\text{Ar}^+$  [6]. An optimal ion energy of 300 eV has been found by studying the deposition and ion beam modification of single Mo and Si films [8]. In this study, however, relatively thick layers (over 10 nm) were used compared to the usual layer thickness in a Mo/Si multilayer (below 5 nm). The use of such thick layers is not preferred in the optimization process because the morphology of the layers can change with the thickness deposited. Such a morphology, which changes with increasing thickness has been reported for Cu as early as 1954 [9] and later for many other materials, such as Mo [10] and Si [11]. In the study performed earlier [8] the angle of incidence has not been optimized.

In order to explain the interface roughness of a layer the growth of a layer is modelled. In other studies on layer growth, the roughening term was found to consist of stochastic roughening by the deposition of atoms [3]. The smoothening effects were identified as diffusion and viscous flow [12]. Also, studies have been performed for the modification of bulk materials with ion bombardment, such as  $\text{SiO}_2$ , in which it was found that roughening is caused by the removal of atoms [13,14].

In this work the angular as well as the energy dependence of ion bombardment is studied systematically over a wide range, in order to optimize the ion beam parameters with layer thicknesses suitable for practical application, first of all to the reflection of 13 nm radiation at near-normal-incidence. Besides the smoothening and roughening processes, several other processes might influence the interface roughness of the multilayers. Therefore, the etch yield and the effect of intermixing by ions that penetrate through the layer are investigated, both as a function of ion energy and angle of incidence. It is noted that the intermixing cannot be determined from single film experiments. The angular dependence of the etch yield is important when multilayer coatings are produced on curved substrates for optical systems, because in this case the angle of incidence of the ions varies across the surface. The variation of the etch yield across the surface has to be minimized and the interface roughness has to be equal for all angles between the ion beam and the curved substrate.

The ion beam parameters to obtain a maximum reflectivity, i.e. low interface roughness, are determined on the basis of post-deposition analysis by near-normal-incidence reflectivity using 14.4 nm radiation and specular reflectivity of small-angle reflectivity measurements using Cu-K $\alpha$  radiation. To investigate the lateral distribution of the interface roughness, diffuse x-ray scattering measurements are performed. The angular dependence of the etch yield is determined from the in-situ reflectivity measurements, which are also used to control the thickness during deposition.

### 3. Experimental

#### 3.1 Multilayer production

The Mo/Si multilayer structures are produced with e-beam evaporation in a dual chamber coating facility, which has been described in detail in Ref. [15].

For this study, 16-period Mo/Si multilayers are produced using Kr<sup>+</sup> ion bombardment of the Si layers. An additional 3.8 nm thick Si layer is deposited on each Si layer, which is removed by ion bombardment. The ion beam parameters investigated include energies between 300 eV and 2 keV, and angles between 20° and 50° with respect to the substrate. The ion beam current was constant (19 mA) during all experiments. During deposition as well as during ion bombardment the substrate holder is rotated with 60 rpm. The entire fabrication process is controlled by continuous in-situ x-ray reflectivity measurement [16,17].

#### 3.2 Multilayer characterization

In order to determine the interface roughness, both near-normal-incidence reflectivity and small angle reflectivity are measured. The near-normal-incidence measurements are performed at 85° with respect to the surface using wavelengths between 12.4 and 16.0 nm. For these measurements a reflectometer at the Center for X-ray Optics is used [18]. The small-angle reflectivity measurements are performed between 0° and 5° using Cu-K $\alpha$  radiation ( $\lambda = 0.154$  nm) at the Danish Space Research Institute [19].

Diffuse x-ray scattering has been used to obtain insight in the lateral distribution of the interface roughness. For these measurements a triple axis set-up with a 7.5 kW rotating Cu-anode (50 kV, 150 mA) is used at the Danish Space Research Institute. The detector is a 150 mm wide position-sensitive detector (2048 channels), which allows a wide detection angle (~8.5°) with a resolution of 2.7 mdeg/channel. This wide angle enables simultaneous detection of the specular beam and the diffuse x-ray scattering up to the fourth Bragg maximum. The data for the diffuse x-ray scattering is then extracted, which results in data corresponding to a scan parallel to the surface in reciprocal space. This will be referred to as transversal scans [19].



#### 4. Basic growth equations

Before we discuss the experiments performed, a growth model is formulated, to be able to explain the roughening and smoothening processes during deposition and ion bombardment. Many models of the growth of single layers and multilayers have been suggested [12,13,20]. We follow the model in Ref. 11 with several small modifications. This model has also been used in Chapter 4 of this thesis. In this model the surface profile of a film at time  $t$  is described by a function  $h(x,y,t)$ , where  $h$  is the height at a certain position  $(x,y)$ . The surface profile  $h(x,y,t)$  has a spatial frequency spectrum  $h(q,t)$ , and the model describes the evolution of  $h(q,t)$  by roughening and smoothening processes in time.

These smoothening processes are considered to be viscous flow (F) and surface diffusion (D) [14]. The rate of change of the height is expressed by:

$$\frac{d|h(q,t)|^2}{dt} = -(Fq + Dq^4)|h(q,t)|^2 \quad (1)$$

The term  $Fq$  is the rate of relaxation by viscous flow,

$$\text{where: } F = \frac{\gamma}{\eta} \quad (2)$$

and  $\gamma$ : the free energy,  
 $\eta$ : the viscosity.

The factor  $Dq^4$  is the rate of relaxation by surface diffusion,

$$\text{where } D = \frac{2D_s \gamma \Omega^2 v}{k_B T} \quad (3)$$

and  $k_B$ : the Boltzmann constant  
 $T$ : the temperature  
 $D_s$ : the surface diffusion coefficient  
 $\Omega$ : the atomic volume  
 $v$ : the number of atoms per unit surface.

Both diffusion and viscous flow are basically induced by the free energy ( $\gamma$ ). The difference between these two is found in the spatial frequency dependence: the relaxation by viscous flow has a  $q$  dependence, and relaxation by diffusion has a  $q^4$  dependence. This indicates that relaxation by diffusion is effective for small features, while relaxation by viscous flow is effective on larger features.

In order to limit the number of fit parameters in the model, we determine which of the two smoothening terms dominates. Earlier, the process of ion bombardment has been described by a local increase of temperature [21]. This study showed that in a small volume, around the colliding ion, the temperature increases and the material is considered to behave like a liquid.

Therefore, the Stokes-Einstein relation ( $\eta D = k_B T / 3\pi L$  where  $L$  is the diffusion length, which is considered to be equal to the nearest neighbour distance of Si  $\{0.234 \text{ nm}\}$ ), can be used to compare the effect of diffusion to that of viscous flow. A spatial frequency ( $q^*$ ) can be determined at which the effect of viscous flow is larger than the effect of diffusion ( $Fq > Dq^4$ ). Using Eqs. (2), (3), a value of  $\Omega$ , the atomic volume for Si is  $0.054 \text{ nm}^3$ , and  $v = 1.16 \times 10^{15} \text{ cm}^{-3}$ , the value  $q^* = (3\pi L / 2\Omega^2 v)^{1/3} \text{ nm}^{-3}$  is determined to be  $4 \text{ nm}^{-1}$  [22]. For values of  $q$  smaller than  $q^*$ , the effect of viscous flow dominates over diffusion. The maximum spatial frequency that can be determined from diffuse x-ray scattering measurements is limited by the angle of reflection, and is in this case  $0.2 \text{ nm}^{-1}$  at the fourth order Bragg maximum. Physically, the upper limit is a value of  $q \approx \pi/L$ , the atomic dimension in reciprocal space, for Si determined to be  $13 \text{ nm}^{-1}$ . This limit is close to the value where the smoothing effects of diffusion and viscous flow are calculated to be equal. From this, the general conclusion follows that viscous flow dominates over diffusion in the entire spatial frequency range investigated. These calculations explain why only viscous flow has to be taken into account for modifications of a layer with ion bombardment, with sufficient by high ion energy (above 100 eV). These general calculations show that the experiments performed earlier for Mo/Si multilayer mirrors are unnecessary [13,23].

Roughness of a surface can arise from two phenomena. The first is stochastic roughening by material deposition or removal described by the term ( $\alpha$ ) in Eq. (4). This term is independent of spatial frequency and amplitude, which is why a Poisson-like process is assumed. The second process is the frequency dependent roughening described by the term ( $Kq^2$ ) [24,25]. The roughening terms in the model of Ref. 12 are expressed by:

$$\frac{d|h(q,t)|^2}{dt} = \alpha + Kq^2|h(q,t)|^2 \quad (4)$$

The value of  $K$  is dependent on the angle of incidence  $\theta$  and the azimuth angle  $\phi$  of the ions with respect to the surface. Since the sample is rotated in the azimuth plane during ion bombardment as well as during deposition,  $K$  is averaged over the azimuth angle. By consequence,  $K$  can be simplified to only an angle of incidence dependence.

The frequency dependent roughening term is determined by:

$$K = \frac{af}{\rho} Y_0(\theta) \quad (5)$$

where:  $f$ : the ion flux  
 $a$ : the average penetration depth  
 $\rho$ : the density of atoms  
 $Y_0(\theta)$ : the sputter yield averaged over the azimuth angle.



The power spectral density function (PSD) of the height variation of the surface is defined as  $PSD(q,t) = \langle h(q,t)h^*(q,t) \rangle$ . Combining both the roughening and smoothing terms in Eqs (1) and (4) results in a PSD function of a single layer:

$$PSD_1(q) = \alpha \frac{[1 - \exp(-b(q)t)]}{b(q)} + \exp(-b(q)t)PSD_{sub}(q) \quad (6)$$

$$\text{where } b(q) = Fq - Kq^2. \quad (7)$$

The  $PSD_1$  is composed of contributions by the layer growth on an ideal smooth surface (the first term in Eq. (6)) and  $PSD_{sub}$ , the PSD of the substrate (the second term in Eq. (6)). The latter is attenuated by a factor  $\exp(-b(q)t)$ . By using this equation recursively, the PSD of each layer of a multilayer can be determined. In a similar way the PSD function of a grown layer can be separated from the PSD function after ion bombardment, using the expression of Ref. [26].

$$PSD(q) = PSD_{ion}(q) + \exp(-b_{ion}(q).t)PSD_{gr}(q) \quad (8)$$

The subscripts "gr" and "ion" denote values during growth and ion bombardment, respectively. For the analysis of the data we thus have three fit parameters:  $F_{gr}$ ,  $F_{ion}$  and  $K_{ion}$ . It is obvious that  $K_{gr} = 0$ , because during growth only stochastic roughening occurs. It is noted that no distinction is made between the growth of Si and Mo, implying that only average values are determined over the period of growth. Also Eq. (8) can be used recursively in order to determine the PSD of each layer of the multilayer [26]. The PSD of the entire multilayer from the diffuse x-ray scattering measurements is further determined using the method described in Ref. [27].

It is concluded that the model used in this study has only three parameters ( $F_{gr}$ ,  $F_{ion}$  and  $K_{ion}$ ), because the effect of diffusion is negligible compared to viscous flow.

## 5. Results

### 5.1 Ion etch yield

The etch yield determines whether the atoms are removed during ion bombardment or moved across the surface. In Section 4 it has been shown that moving atoms around, by diffusion or viscous flow, smoothens the layers, while removing the atoms roughens the layers.

The frequency dependent roughening term in Eq. (5) is dependent on the etch yield, the penetration depth, and the flux of ions. From the in-situ reflectivity measurements the etch yield is determined. In this experiment the additional thickness deposited is 3.8 nm, and the time needed to remove this excess layer is measured. Separate experiments have been performed to determine the flux of the ions for all energies and angles of incidence by measuring the electrical current on a 1 cm<sup>2</sup> probe on the position of the sample, while keeping the ion beam current constant (19 mA). The flux of ions decreases with the angle of

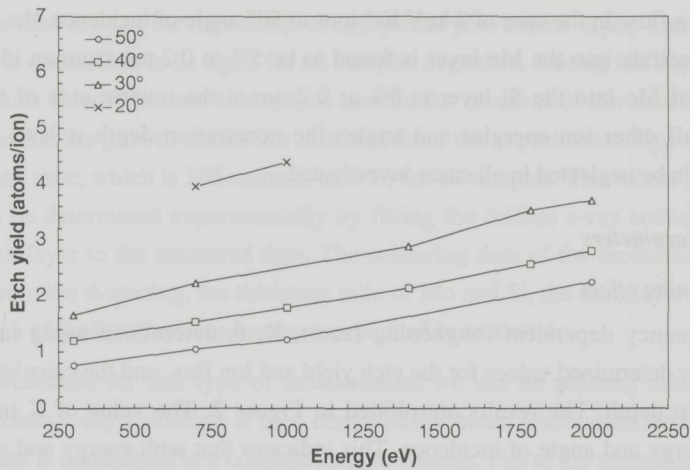


Figure 1: The measured etch yield of Si atoms as a function of ion energy and angle of incidence.

incidence, which is a geometrical effect. The flux also decreases up to 30% going from 300 eV to 2 keV, because of better defocusing properties at the higher ion beam voltage of the ion gun. This is consistent with the specifications of the gun.

The etch yield is displayed in Figure 1 for several angles of incidence as a function of ion energy. The values are averaged over 10 periods. The graph shows that the etch yield increases with increasing ion energy and decreasing angle of incidence of the ion gun. For the fabrication of a multilayer on a curved substrate the additional layer deposited has to vary over the surface. This additional layer can be calculated using the experimentally determined values for of the etch yield and the geometry of the mirrors. In the experiments described in this study the substrates are flat. For the fabrication of multilayers on curved substrates the effect of redeposition could be different compared to flat substrates. This effect will be addressed in future experiments.

### 5.2 Penetration depth

If the penetration depth of the ions becomes comparable to the Si layer thickness, the ions might cause intermixing of Mo and Si. The penetration depth and the lateral spread of collisions of the ions are calculated as a function of ion energy and angle using the TRIM-95 code [28]. The average penetration depth is calculated to be below 3.5 nm for all energies and angles of incidence. However, the maximum penetration depth could be as high as 6.5 nm for ions with an energy of 2 keV at 50° angle. The lateral spread of ions is determined to be equal to the penetration depth corrected for the geometrical effect of the angle of incidence. These calculations also yield the distributions of the Si and Mo atoms after bombardment. The fraction of intermixed atoms can be calculated using these distributions as well as the etch



rate and the ion flux. In the case of 2 keV  $\text{Kr}^+$  ions at  $50^\circ$  angle of incidence, the fraction of Si atoms that penetrate into the Mo layer is found to be 5% at 0.2 nm from an ideal interface. The fraction of Mo into the Si layer is 8% at 0.2 nm at the reverse side of the interface. Because for all other ion energies and angles the penetration depth is less, the effect of intermixing can be neglected in all cases investigated.

### 5.3 Growth parameters

#### 5.3.1 Roughening effect

First the frequency dependent roughening factor,  $K$ , is determined using in Eq. (5) the experimentally determined values for the etch yield and ion flux, and the calculated values for the penetration depth. The results are plotted in Figure 2. The value of  $K$  increases with increasing energy and angle of incidence. This indicates that with energy and angle also the roughness increases, supposing that the smoothing terms for all energies and angles are equal.

It is noted that tabulated values for the atomic densities are used. In previous experiments however, we have observed a large free volume in the Si layer deposited at room temperature without ion bombardment [29]. We suggest that the free volume decreases during ion bombardment, in agreement to EXAFS data on similar samples [30]. This implies that the accuracy of the value for the Si density is approximately 15%, which also determines the accuracy of the value of  $K$ .

#### 5.3.2 Smoothing effect

A few assumptions have been made in order to determine the values for the values for the viscous flow ( $F$ ). It is assumed in Eq. (8) that during growth the time for viscous flow is

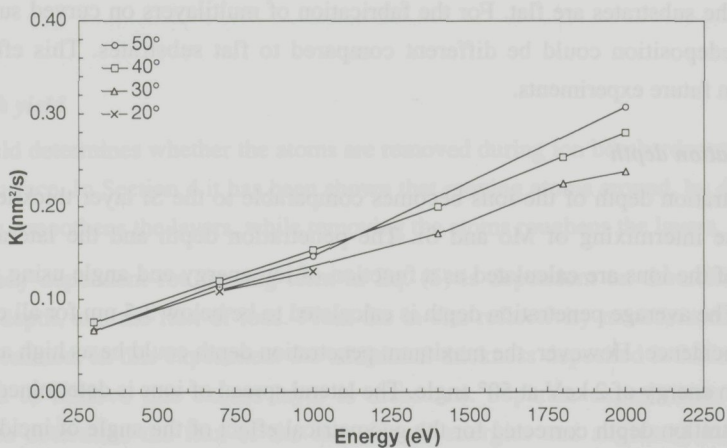


Figure 2: Calculated values of  $K$  using measured data on the etch yield and a calculated penetration depth.

limited to the time needed for deposition of one period plus excess layer. The value for this viscous flow is considered to be equal for all samples deposited. During ion bombardment the time for viscous flow is limited to the time needed for removal of the excess layer. Other values needed for the growth model are obtained from the experiments. One of these is the total deposition time, which is 360 seconds ( $\pm 10\%$ ) for all samples. The values for the viscous flow have to be determined experimentally by fitting the diffuse x-ray scattering data of a modelled multilayer to the measured data. The scattering data of the modelled multilayer is determined from the d-spacing, the thickness ratio of Mo and Si, the multilayer materials, and the PSD of each of the interfaces, as has been explained in section 4.

For the fit procedure for this type of measurement we use an existing method [26]. The calculated diffuse x-ray scattering is then corrected for beam attenuation, and the measured reflectivity data is normalized to a constant sample volume. Fits to the measured diffuse x-ray scattering are only performed at the third order Bragg maximum, because of a higher accuracy than with the first and second order Bragg maxima. Transversal scans and the simulated diffuse x-ray scattering of three samples (300 eV,  $50^\circ$ ; 1 keV,  $50^\circ$ ; 2 keV,  $40^\circ$ ) are plotted in Figure 3, 4 and 5, respectively. From the graphs it is concluded that the diffuse x-ray scattering data of the modelled structures fit accurately to the measured data.

The value found for the viscous flow during growth is less than 0.03 nm/s for all samples, which is negligibly small. In Figure 6 the calculated values for the viscous flow during ion bombardment are shown. This clearly indicates that the smoothening effect by ion bombardment is increasing with ion energy and angle. This also indicates that probably even larger values for the viscous flow can be obtained for ion energies above 2 keV and larger angles than  $50^\circ$ , both being currently the practical limits of the coating facility.

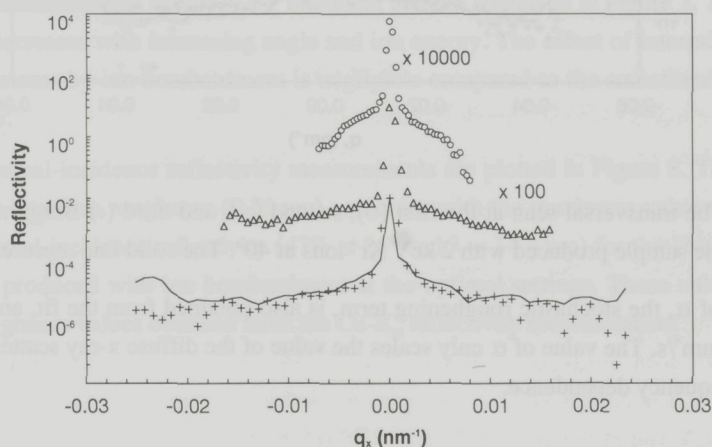


Figure 3: The transversal scan at the first (○), second (△), and third (+) Bragg maximum for the sample produced with 300 eV Kr<sup>+</sup> ions at  $40^\circ$ . The solid line represents the fit.



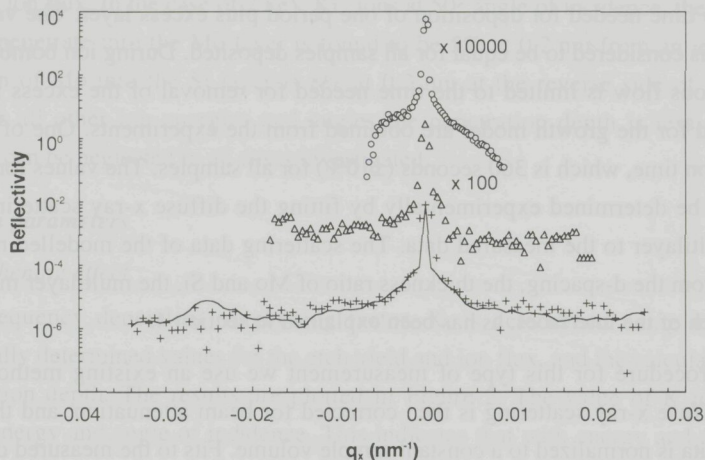


Figure 4: The transversal scan at the first ( $\circ$ ), second ( $\Delta$ ), and third ( $+$ ) Bragg maximum for the sample produced with 1 keV  $\text{Kr}^+$  ions at  $50^\circ$ . The solid line represents the fit.

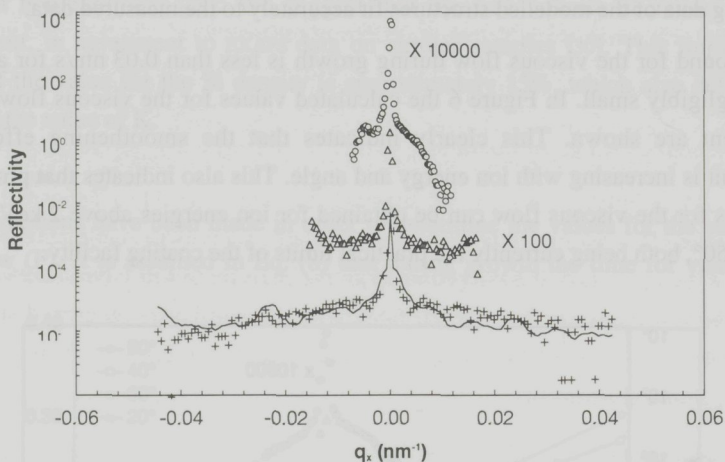


Figure 5: The transversal scan at the first ( $\circ$ ), second ( $\Delta$ ), and third ( $+$ ) Bragg maximum for the sample produced with 2 keV  $\text{Kr}^+$  ions at  $40^\circ$ . The solid line represents the fit.

The value of  $\alpha$ , the stochastic roughening term, is also obtained from the fit, and is found to be  $5 \times 10^{-6} \text{ nm}^4/\text{s}$ . The value of  $\alpha$  only scales the value of the diffuse x-ray scattering, because it has no frequency dependence.

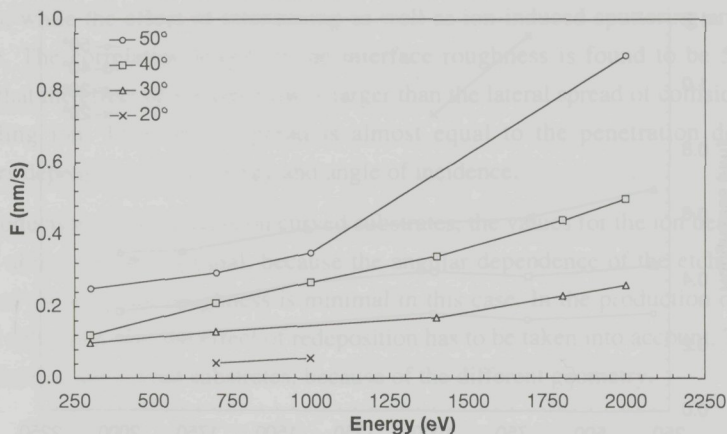


Figure 6: The values of  $F$  calculated from the diffuse x-ray scattering measurements.

### 5.3.3 Correlation length

From the transversal scan also the correlation length of the interface roughness can be determined using the method described in Ref. [23]. The correlation function used is a Lorentzian function. For all samples investigated a correlation length of  $50 \pm 10$  nm is found. A distinction for the correlation length between the different ion beam parameters could not be obtained from the fit of the correlation function. More precise values might be obtained using high resolution diffuse x-ray scattering [31] or AFM measurements.

### 5.4 Interface roughness

The different values for the sputter yield and the viscous flow result in differences in the interface roughness of the multilayers. These differences are determined from the specular reflectivity measurements using  $\text{Cu-K}\alpha$  radiation, and are displayed in Figure 7. The interface roughness decreases with increasing angle and ion energy. The effect of intermixing and the removal of atoms by ion bombardment is negligible compared to the smoothing effect by viscous flow.

The near-normal-incidence reflectivity measurements are plotted in Figure 8. The minimum value of the interface roughness (0.21 nm) coincides with the maximum value measured for the near-normal-incidence reflectivity (47% at  $85^\circ$  and  $\lambda = 14.4$  nm) for the 16-period Mo/Si multilayers produced with ion bombardment at the optimal settings. These values coincide with the roughness values obtained from the  $\text{Cu-K}\alpha$  reflectivity measurements.



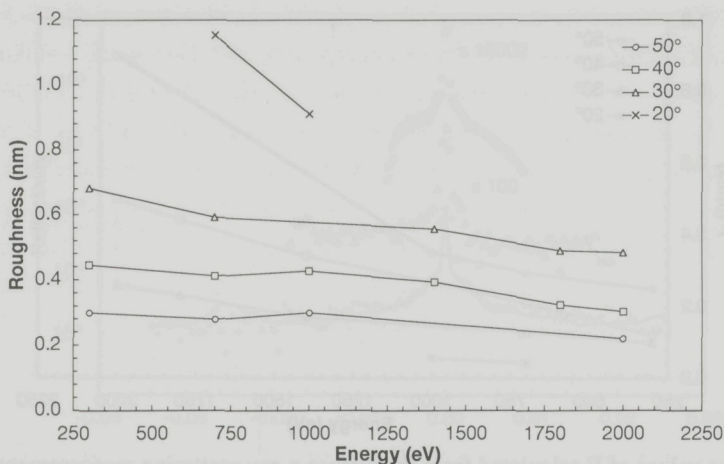


Figure 7: The interface roughness determined from the specular reflectivity measurements with Cu-K $\alpha$  reflectivity measurements.

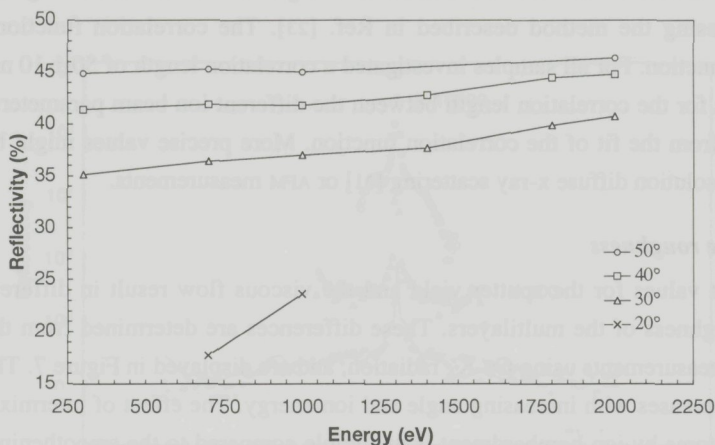


Figure 8: The measured near-normal-incidence reflectivity at 87° and 14.4 nm radiation. The values are corrected for small variations of the d-spacing.

## 6. Conclusions

Mo/Si multilayer x-ray mirrors have been produced using e-beam evaporation and additional ion bombardment at ion energies between 300 eV and 2 keV and angles of incidence between 20° and 50° with respect to the surface. From near-normal-incidence reflectivity measurements it is concluded that the optimal ion beam parameters within this parameter range are 2 keV and 50° angle of incidence. These settings result in a minimum value of the interface roughness. From diffuse x-ray scattering measurements it is concluded that the effect of viscous flow during ion bombardment dominates the change of the interface

roughness, while the effect of intermixing as well as ion-induced sputtering are found to be negligible. The correlation length of the interface roughness is found to be 50 nm, which indicates that the effect of viscous flow is larger than the lateral spread of collisions caused by the colliding ion. This lateral spread is almost equal to the penetration depth, several nanometers depending on the energy and angle of incidence.

For the production of multilayers on curved substrates, the values for the ion beam parameters described above are also optimal, because the angular dependence of the etch yield and the variation of the interface roughness is minimal in this case. In the production of multilayers on curved substrates also the effect of redeposition has to be taken into account. This might be different for flat and curved substrates, because of the different geometry.

## 7. Acknowledgements

We acknowledge the use of the soft x-ray reflectometer made available by E.M. Gullikson (Center for X-ray Optics, Lawrence Berkeley Laboratory, Berkeley (CA), USA). These investigations within the framework of FOM (the Foundation for Fundamental Research on Matter) are supported by STW (the Netherlands Technology Foundation) and the Dutch Government in the context of EUREKA.

## 8. References

1. K. Murakami, H. Nakamura, T. Oshino, M. Ohtani, and H. Nagata, Proc. SPIE **1742** (1992) 614-620
2. M. Cevro, and G. Carter, Opt. Eng. **34** (1995) 596-606
3. E. Spiller, Appl. Phys. Lett. **54** (1989) 2293-2295
4. E.J. Puik, M.J. v d Wiel, J. Verhoeven, and H. Zeijlemaker, Thin Solid Films **193/194** (1990) 782-787
5. E. Louis, E. Spiller, S. Abdali, F.E. Christensen, H.-J. Voorma, N.B. Koster, P.K. Frederiksen, C. Tarrío, E.M. Gullikson, and F. Bijkerk, Proc. SPIE **2515** (1995) 194-203
6. R. Schlatmann, C. Lu, J. Verhoeven, E.J. Puik, and M.J. van der Wiel, Physics of X-ray Multilayer Structures, OSA Technical Digest Series, **7** (1992) PD6-1
7. R. Schlatmann, A. Keppel, Y. Xue, and J. Verhoeven, Appl. Phys. Lett. **63** (1993) 3297
8. R. Schlatmann, J. Verhoeven, L. Chunguang, E.J. Puik, and M.J. van der Wiel, Appl. Surf. Sci. **78** (1994) 147-157
9. L.G. Parratt, Rhys. Rev. **95** (1954) 359-369
10. J. Verhoeven, L. Chunguang, E. J. Puik, M.J. van der Wiel and T.P. Huijgens, Appl. Surf. Sci. **55** (1992) 97-103
11. M. Niibe, M. Hayashida, T. Iizuka, A. Miyake, Y. Watanabe, R. Takahsi, Y. Fukuda, Proc. SPIE **1343** (1990) 2-12
12. E. Chason, T.M. Mayer, B.K. Kellerman, D.T. McIlroy and A.J. Howard, Phys. Rev. Lett. **72** (1994), 3040-3043
13. D.G. Stearns, Appl. Phys. Lett. **62** (1993) 1745-1747
14. T.M. Mayer, E. Chason, and A.J. Howard, J. Appl. Phys. **76** (1994) 1633-1643
15. E. Louis, H.-J. Voorma, N.B. Koster, L. Shmaenok, F. Bijkerk, R. Schlatmann, J. Verhoeven, Yu.Ya. Platonov, G.E. van Dorssen, and H. Padmore, Microelectron. Eng. **23** (1994) 215



16. E.J. Puik, M.J. van der Wiel, H. Zeijlemaker, and J. Verhoeven, *Appl. Surf. Sci.* **47** (1991) 63-76
17. E. Spiller, *Soft X-ray optics*, SPIE, 1994
18. E.M. Gullikson, J.H. Underwood, P.C. Baston, and V. Nikitin, *J. X-ray Sci. Technol.* **3** (1992) 283-299
19. F.E. Christensen, A. Hornstrup, E. Jakobsen, P. Jonasson, M.M. Madsen, H.W. Schnopper, N.J. Westergaard, and P. Orup, *Nucl. Inst. Methods A* **256** (1987) 381-392
20. W.W. Mullins, *J. Appl. Phys.* **30** (1959) 77-83
21. C. Volkert and A. Polman, *Mater. Res. Soc. Symp. Proc.* **235** (1992) 3-7
22. O.B. Loopstra, E.R. van Sneek, Th.H. de Keijser, and E.J. Mittemeijer, *Phys. Rev. B* **44** (1991)
23. R. Schlattman, J.D. Schindler, J. Verhoeven, Submitted to *Phys. Rev. B.*
24. R.M. Bradley and J.M.E. Harper, *J. Vac. Sci. Technol. A* **6** (1988) 2390-2395
25. P. Sigmund, *Phys. Rev.* **184** (1969) 383-416
26. E. Spiller, D.G. Stearns, and M. Kumrey, *J. Appl. Phys.* **74** (1993) 107-118
27. D.G. Stearns, *J. Appl. Phys.* **71** (1992) 4288-4298
28. J.F. Ziegler, *The Stopping Range of Ions in Matter*, Vol. 2-6 Pergamon Press, 1977-1985
29. H.-J. Voorma, E. Louis, N.B. Koster, and F. Bijkerk, submitted to *J. Appl. Phys.*
30. H.-J. Voorma, G.E. van Dorsen, E. Louis, N.B. Koster, A.D. Smith, M.D. Roper, and F. Bijkerk, *Appl. Surf. Sci.* **93** (1996) 221-230
31. F.E. Christensen, S. Abdali, A. Hornstrup, H.W. Shnopper, P. Slane, and S.E. Romaine, *Proc. SPIE* **2011** (1994) 18-33

## Exafs measurements on the structure of Mo/Si multilayers using ion bombardment and increased deposition temperature

### 1. Abstract

This study focuses on explaining differences in soft x-ray reflectivity observed for Mo/Si multilayers produced by e-beam evaporation with two different additional methods: ion-etching of the Si layer and optimization of the substrate temperature during deposition. A 32-period multilayer made with ion-etching has a near normal incidence reflectivity of 50%, while the one made at an optimum deposition temperature shows only 41%.

The values for the interface roughness or layer thickness errors obtained from the analysis of small angle reflectivity measurements cannot explain this difference, but a different morphology of the Si and Mo layers could. Extended x-ray absorption fine structure (EXAFS) experiments have been carried out at the Si-K and the Mo-K edge to obtain information on the multilayer structure and chemical composition.

The results of these EXAFS measurements on the two types of multilayers indicate that both the Si and the Mo have an amorphous structure and that no Mo-Si compounds are formed at the interfaces. However, it is found that multilayers made with ion-etching have a reduced fraction of oxygen ( $\leq 0.5\%$ ) in the Si layer compared to layers produced without etching (4.7%). The latter fraction of oxygen, originating from the background gas in the deposition system, results in higher absorption of soft x-ray radiation and therefore affects the near normal incidence reflectivity. Although both the Si and Mo layers produced with the three different deposition methods are amorphous, some structural differences have been found using the EXAFS analysis.

### 2. Introduction

Mo/Si multilayers attract considerable attention for various applications such as EUV lithography and x-ray spectroscopy [1]. To increase the image field these systems use mirrors at near normal incidence. Multilayer mirrors may then seem the appropriate choice since these can be produced with high reflection at near normal incidence. High reflectivity is needed



especially in systems consisting of multiple reflecting surfaces, since the total throughput of the system scales with  $R^n$ , with  $n$  the number of reflecting surfaces. The multilayer structures can be produced with techniques such as magnetron sputtering [2] or e-beam evaporation [3]. In the case of e-beam evaporation two additional techniques can be used to improve the optical performance of the multilayer: ion-etching of the interfaces and optimization of the substrate temperature during deposition.

A difference in the absolute reflectivity of the Mo/Si multilayers made with e-beam evaporation at near normal incidence has been reported for those produced with ion-etching [4, 5] compared to those deposited at an enhanced substrate temperature [6, 7]. In this study we investigate Mo/Si multilayers with 32 periods used at near normal incidence for a wavelength of 13.5 nm. These multilayers were produced with e-beam evaporation and either of the two or both additional techniques.

The d-spacing ( $\Lambda$ ) and the ratio ( $\Gamma$ ) of the thickness of the high-Z material to the total thickness determine the wavelength and angle of incidence at which maximum reflection is achieved. The optical performance of a multilayer is then determined by the interface roughness ( $\sigma$ ), the layer thickness errors ( $\zeta$ ), and the morphology and chemical composition of the materials deposited. Except for the last two parameters, we can obtain these parameters from analysis of small angle reflectivity ( $\theta$ - $2\theta$ ) measurements. However, the difference in the parameters obtained from the  $\theta$ - $2\theta$  scans cannot explain the difference in the optical quality observed.

What remains to be studied is the morphology and the elemental composition of the layers deposited. These factors can change the refractive index and might explain the difference in reflectivity. Several techniques are suitable to investigate the chemical composition: EXAFS analysis, Auger electron spectroscopy, Rutherford backscattering and X-ray Photoelectron Spectroscopy. The advantage of EXAFS analysis is that it yields information about the structure of the materials. A disadvantage might be that EXAFS analysis requires a priori knowledge about the composition. However, in our deposition system the elements are known because of controlled vacuum conditions and materials used for the deposition. The other techniques only determine the chemical composition. Therefore, we used EXAFS measurements, carried out at both the Si-K and the Mo-K edge to reveal the structure and the elemental composition of the layers.

### 3. Production of the multilayers

We produced the Mo/Si multilayers on Si (100) substrates with e-beam evaporation in an ultra-high vacuum system at a base pressure of  $5 \times 10^{-8}$  mbar [1]. The system is baked out for 10 hours in order to decrease the partial water pressure to  $2 \times 10^{-8}$  mbar. During deposition the layer thickness is monitored with an in-situ x-ray reflection system. This system uses N-K $_{\alpha}$

Table I: The deposition methods. T: substrate temperature and N: number of layer pairs.

Method	T (°C)	N
Optimal substrate temperature (T215)	215	32
Ion-etching of the Si layer at room temperature (ET36)	36	32
Optimal substrate temperature and ion-etching of the Si layer (ET215)	215	32

radiation (3.16 nm) at 13.5° angle of incidence with respect to the substrate. These monitor settings result in a multilayer with  $\Lambda = 7$  nm and  $\Gamma = 0.37$ .

To decrease the interface roughness we carried out experiments using enhanced substrate temperatures during deposition. The best reduction of the interface roughness [6] was found for a substrate temperature of 215 °C. Different optimal temperatures have been found for multilayers with other  $\Gamma$  [6, 7].

The second method, ion-etching, also decreases the interface roughness. Earlier experiments showed that ion-etching of the Si layer does result in an improved interface roughness, while etching of the Mo layer does not [4, 8]. From each Si layer 2.2 nm is removed using etching with Kr<sup>+</sup>-ions after deposition. The optimized ion-beam parameters for Mo/Si multilayers are: 300 eV Kr<sup>+</sup>-ions at an angle of 45 degree, and a flux of  $1.25 \times 10^{14}$  ions/cm<sup>2</sup> s [9].

A summary of the methods investigated are listed in Table I. These methods have demonstrated their reproducibility in many deposition runs and were evaluated in both grazing angle and near normal incidence reflectivity measurements.

#### 4. Experimental

Small angle reflectivity is measured and used to quantify the interface roughness ( $\sigma$ ), the thickness ratio ( $\Gamma$ ), the d-spacing ( $\Lambda$ ), and the layer thickness errors ( $\zeta$ ). The near normal incidence reflection is measured at the wavelength and angle used for the final application, which in our case is EUV projection lithography. EXAFS spectra both at the Si-K and the Mo-K edge are measured to investigate a possible different morphology or chemical composition of the materials deposited.

##### 4.1 Small angle reflectivity measurements

Small angle reflection measurements ( $\theta$ -2 $\theta$  scans) with Cu-K $\alpha$  radiation are generally used to characterize multilayer structures [10, 11, 12]. The  $\Lambda$  and the refractive index decrement of the multilayer are obtained from the positions of the Bragg maxima in the  $\theta$ -2 $\theta$  scan. Further characterization is based on the analysis of the reverse Fourier transforms of the reflection at the Bragg peaks of these  $\theta$ -2 $\theta$  scans [11]. Using this method, the average interface roughness, the thickness ratio and the layer thickness errors are determined (Table II).



Table II: Results of the Cu-K $\alpha$  measurement. The symbols are defined in the text.

Method	$\Lambda$ (nm)	$\sigma$ (nm)	$\Gamma$ -factor	$\zeta$ (nm)
T215	7.15	0.37	0.418	0.5
ET36	6.89	0.35	0.374	0.2
ET215	7.32	0.36	0.408	0.2

As can be concluded from Table II, all three deposition methods result in an interface roughness of approximately 0.36 nm. The multilayers made with additional ion-etching have smaller layer thickness errors compared to the multilayers deposited without ion-etching. This is explained by the fact that the slow etch rate enables a better thickness control of each individual layer compared to the faster deposition process. Also, determination of the etching end points, obtained from the monitor signal, is more distinct.

The temperature optimized multilayers have a slightly different  $\Gamma$ , which is explained by a decrease of the Si thickness. After deposition of each single layer the structure of the Si layer changes to a more compact structure due to the enhanced substrate temperature. Changes in the thickness of the Si layer up to 10% are reported for a multilayer deposited at a temperature of 215°C compared to room temperature [13]. We would expect the multilayers to have the same near normal incidence reflectivity because all methods result in the same interface roughness.

#### 4.2 Soft x-ray measurements

The near normal incidence reflectivity measurements have been carried out at station 5U.1 of the Daresbury SRS [14]. The best reflectivity is obtained for the ion-etched multilayer deposited at room temperature (Table III). This multilayer has a near normal incidence reflectivity of 50%, while the one made at an optimum deposition temperature shows only 41%. The differences in the reflection observed cannot be ascribed to the small differences of the angle or wavelength used for these measurements. This follows from calculations on the theoretical reflectivity with the measured interface roughness and an identical angle and wavelength as used for the measurement ( $R_{th}$  in Table III). We have demonstrated in the previous section that interface roughnesses between 0.35 and 0.37 nm are found for all the multilayers using small angle reflectivity measurements, reported in Table II. With that roughness, an otherwise ideal reference multilayer would have a near normal incidence reflectivity of 64%. We note that considerably higher values, up to 64%, are obtained for samples produced with a larger number of layer pairs [5]. We can conclude that no critical layer thickness errors have been made during deposition because the multilayers are produced using the in-situ reflection. In the previous section we have shown that for the ion etched samples a typical value for the layer thickness errors is 0.2 nm. This value will introduce an uncertainty of 1% in the near normal incidence reflection, dependent on actual set of layer

Table III: Near normal incidence x-ray reflection.  $R_m$  is the measured reflectivity,  $R_{th}$  is the simulated reflectivity of a reference Mo/Si multilayer with the measured interface roughness listed in Table II.

Method	$\theta$ (deg.)	$\lambda$ (nm)	$R_m$ (%)	$R_{th}$ (%)
T215	77.9	13.7	41.0	60.8
ET36	83.0	13.3	50.0	64.2
ET215	83.0	13.8	45.7	61.8

thicknesses. We conclude that the analysis of small angle reflectivity does not give sufficient information to adequately predict the near normal incidence reflectivity. Apparently another parameter, such as the chemical composition or the structure, of the multilayer determines the near normal incidence reflectivity.

### 4.3 EXAFS measurements

The analyses of the measured EXAFS data are performed using the standard procedure for data reduction: the measured spectra are summed and smoothed, after which the pre- and post-edge continua are removed using a polynomial fit procedure [15, 16, 17]. The EXCURV92 computer code is used for fitting a model structure to the observed EXAFS spectrum and its Fourier transform [18]. The program uses calculated phase shifts and the curved wave theory. The  $k^3$ -weighted EXAFS signal,  $\chi(k)$ , is extracted. The model, containing the central atom and neighbouring atoms, is fitted to both the EXAFS signal and its Fourier transform. This fit yields the number, the distance to the surrounding atoms and the mean square average of the atomic displacements ( $\sigma_r^2$ ).

The following atomic numbers are taken into account: 14 (Si), 42 (Mo), 16 (O). Molybdenum and silicon are considered because Mo and Si layers are investigated and some Mo in the Si structure and vice versa is expected due to interdiffusion. Oxygen is taken into account because of its presence in the background gas in the deposition system. Also other atoms are present in the background gas such as N and C (mostly as CO and CO<sub>2</sub> molecules), but the activation energy for the formation of Si-O is considerably higher than for Si-N or Si-C. Therefore, only O is expected in the Si layers caused by adsorption of oxygen atoms to the Si surface during the coating procedure [19]. At our operational pressure, one monolayer of oxygen is formed during the time needed for the deposition of one Si layer, which would correspond to an O amount of  $5\% \pm 1\%$ . The activation energy for the formation of Mo-O is also lower than for Si-O. Therefore, we do not expect much oxygen in the Mo layer.

The data obtained from the EXAFS analyses are used to calculate the refractive index and absorption coefficients in order to explain the differences in soft x-ray reflectivity. Using the number of neighbour atoms and distances obtained from the model, the atomic percentages of the elements (Mo, Si, and O) surrounding the central Si and Mo atoms, respectively, can be



determined, as well as the refractive index of each of the layers. The contributions from the interfaces will be considered in section 5.

#### 4.3.1 Measurements at the Si-K edge

Reflection EXAFS measurements at the Si-K edge were performed at station 3.4 of the Daresbury SRS [20]. The critical angle was measured for wavelengths between 0.55 and 0.69 nm. At the Si-K edge (0.675 nm) the critical angle was found to be  $0.8^\circ$ . We measured the EXAFS signal in reflection mode at  $0.6$  and  $1.1^\circ$ , that is below and above the critical angle. The advantage of measurements below the critical angle is that the EXAFS signal is high, a disadvantage is that only a few layers are measured because of the limited penetration depth. We calculate that only 2 layer pairs are contributing to the EXAFS signal [21]. For the measurement performed at  $1.1^\circ$  the entire stack of 32 layer pairs is contributing to the EXAFS signal. A disadvantage of the measurements at  $1.1^\circ$  is that the EXAFS signal can in principle be influenced by the Si (100) substrate. The effective transmission of the multilayer for the EXAFS signal at  $1.1^\circ$  is calculated to be 3%: this amount could contain information from the Si structure of the substrate. We conclude that the morphology of Si structure is constant throughout the stack and that the measurements are not influenced by the substrate, because no significant difference is observed in the models obtained from the measurements below and above the critical angle.

To match the theoretical  $\chi(k)$  to the experimental function, a model structure is made with Si, Mo, and O atoms up to a distance of 0.9 nm, limited by the quality of the EXAFS signal. As an example of the EXAFS measurements, Figure 1 shows the experimental and the fitted EXAFS signal of sample ET36 for the measurement at 0.6 degree. In Figure 2 their Fourier transforms

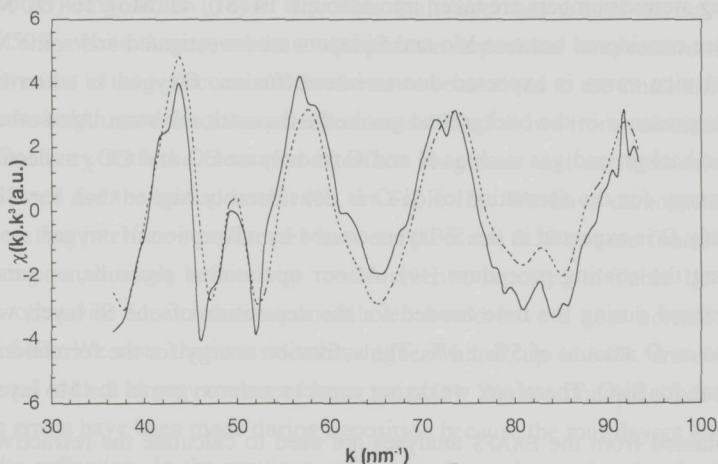


Figure 1: EXAFS signal for the Si structure for method ET36. Experimental (—) and fitted ( - - ) curves

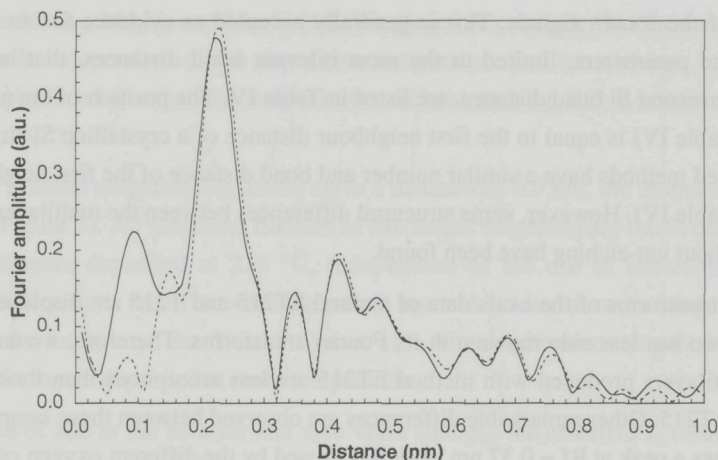


Figure 2: Fourier transforms of the EXAFS signals of method ET36 shown in Figure 1. Experimental (—) and fitted (---) curves.

are displayed. As can be seen in for example the Fourier transform in Figure 2, there is a discrepancy between the experimental and fitted data at low, not significant,  $R_f$  values. The difference between the experimental and the theoretical curve in Figure 2 is calculated. The Fourier transform of this difference shows a clear peak at  $R_f = 0.1$  nm. This is caused by incomplete subtraction of the background by the algorithm of the computer program. Since, the peak is not a meaningful value this will not influence the calculated model structure.

We observe only one strong maximum and some smaller side maxima in the Fourier

Table IV: Fit parameters for the Si signal:  $n$  is the number of neighbouring atoms surrounding a Si atom,  $R_f$  the average bond distance (nm) from Si to neighbouring atoms, and  $\sigma_f$  the rms deviation from the average bond distance.

Method	$n$	Element	$R_f$ (nm)	$2\sigma_f^2$ ( $10^{-4}$ nm <sup>2</sup> )
T215	0.7	O	0.157	0.1
	2.4	Si	0.231	0.3
	1.3	Mo	0.288	0.3
	2.2	O	0.307	0.3
	3.3	Si	0.361	0.5
ET36	0.3	O	0.165	0.1
	1.5	Si	0.231	0.3
	0.5	Mo	0.287	0.3
	0.8	Si	0.301	0.6
ET215	0.3	O	0.170	0.2
	1.1	Si	0.233	0.2
	0.4	Mo	0.288	0.3
	1.1	Si	0.310	0.3



transforms of the EXAFS signals. This is generally accepted as evidence for an amorphous structure. The parameters, limited to the most relevant bond distances, that is up to and including the second Si bond distance, are listed in Table IV. The position of the main peak at 0.231 nm (Table IV) is equal to the first neighbour distance of a crystalline Si structure [22]. The ion-etched methods have a similar number and bond distance of the first neighbouring Si atoms (see Table IV). However, some structural differences between the multilayers deposited with and without ion-etching have been found.

The Fourier transforms of the exafs data of method ET215 and T215 are displayed in Figure 3. The last two has less side maxima in its Fourier transforms. Therefore, we can conclude that the multilayers produced with method ET215 are less amorphous than those produced with method T215. Other remarkable differences are observed between these samples. Firstly, Figure 3 shows a peak at  $R_f = 0.37$  nm, which is caused by the different oxygen content in the Si layers. The ion-etched multilayers contain less oxygen compared to the non-etched multilayers. Secondly, the value of the Si-O bond distance is larger if ion-etching is applied (Table IV). This distance is 0.157 nm for the temperature optimized method and between 0.165 and 0.170 nm for the ion-etched methods. A third difference is found in the distance of the second Si neighbour. This distance is 0.31 nm for the etched samples and 0.36 nm for the non-etched samples both deposited at 215°C (Table IV). These three facts indicate that the ion-etching process forces the Si layer into a more compact structure and that most of the oxygen atoms are removed from the Si layers. Apparently, a structure with a lower fraction of oxygen results in a larger Si-O bond distance. A similar effect has been reported in studies on single thin films of amorphous hydrogenated silicon oxide [23].

For all multilayers produced, the Si-Mo bond distances in the Si layer do not coincide with the

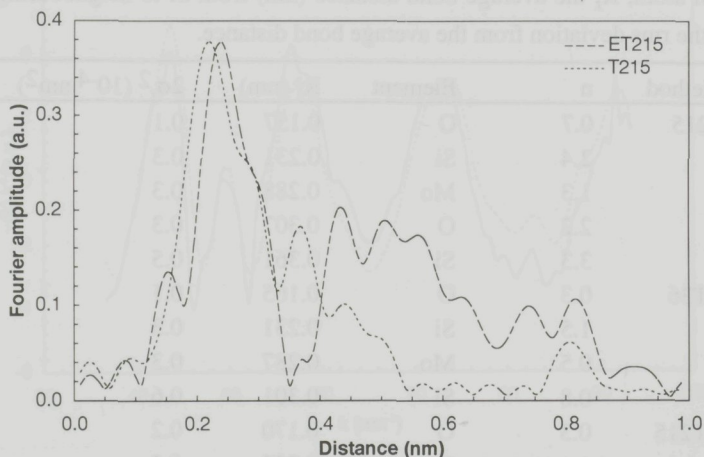


Figure 3: Fourier transforms of the fitted EXAFS signals of the Si structure of method ET215 and T215.

distances for  $\text{MoSi}_2$ ,  $\text{Mo}_3\text{Si}$ , and  $\text{Mo}_5\text{Si}$  [24]. We therefore conclude that the samples contain no compounds independent of the deposition temperature and ion-etching. In the case of multilayers produced at enhanced temperatures without etching, this is confirmed by TEM analysis [25, 26, 27].

Taking into account neighbouring atoms up to a distance of 0.9 nm, the atomic fractions are calculated (Figure 3). An increased fraction of Mo atoms neighbouring the Si atoms is found in the multilayers deposited at 215 °C, independent of the use of ion-etching. Another significant difference is found between the etched layers deposited at room temperature and at 215 °C. In the latter case the Si atoms have 41% Mo neighbours compared to 25% Mo neighbours for layers deposited at room temperature.

The presence of Mo in the Si layer and vice versa changes the effective  $\Gamma$  value, but hardly influences the near normal incidence reflection. However, the presence of O atoms in the Si layer results in a higher absorption of 13.5 nm radiation and therefore in a reduction of the near normal incidence reflectivity. The 4.7% oxygen content, found by exafs analysis, fully explains the loss of near normal incidence reflectivity observed for method T215 ( $R = 41\%$ ) compared to method ET215 ( $R = 46\%$ ). Factors that might have resulted in a reduction of the partial oxygen pressure in the deposition system, such as flushing with Kr gas, have been tested separately [28]. These experiments did not result in a decrease of the oxygen pressure in the system. We therefore conclude that it is the ion-etching process that removes oxygen atoms from the Si layer.

From these experiments we conclude that increasing the temperature always increases the amount of diffusion into the Si layer. Ion-etching of the Si layer decreases the fraction of O in the Si layer and therefore minimizes the absorption of 13.5 nm radiation. This indicates our preference for using ion-etching of the Si layer over temperature optimization in the production of Mo/Si multilayers. A further improvement is to be expected by using a decreased operational pressure of less than  $10^{-9}$  mbar in order to prevent the oxygen contamination of the Si layer.

#### 4.3.2 Measurements at the Mo-K edge

Measurements at the Mo-K edge have been performed to reveal the Mo structure. These were carried out at station 9.2 of the Daresbury SRS [29]. The EXAFS signal was measured in

Table V: Atomic percentage of Si, Mo, and O surrounding the Si atoms.

Method	Si (%)	Mo (%)	O (%)
T215	59	36	4.7
ET36	75	25	0.5
ET215	59	41	0.5



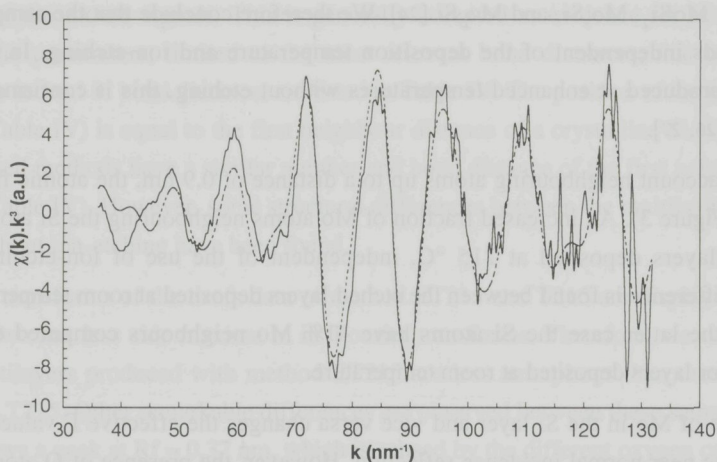


Figure 4: EXAFS signal for the Mo structure for method ET36. Experimental (—) and fitted (---) curves.

fluorescence mode and the incident x-ray beam was at 45° with respect to the surface. The EXAFS analysis is identical to the method described in section 3.3.1. Figure 4 shows the simulated  $\chi(k)$  fitted to the experimental data of method ET36.

In the Fourier transform of the EXAFS signals again only one strong maximum is found with smaller side maxima (Figure 5). We therefore conclude that the Mo layers stay amorphous up to a substrate temperature of at least 220 °C, again independent of ion-etching. Other studies limited to room temperature, concluded that the Mo layer is amorphous up to a thickness of 4.0 nm (In our case the thickness of the Mo layer is approximately 3.0 nm) [9].

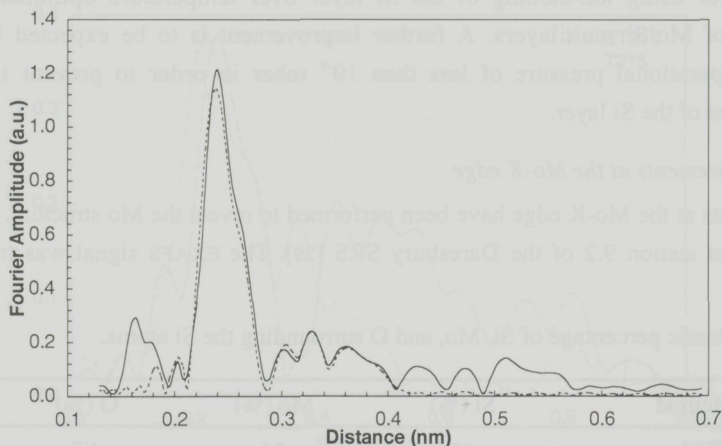


Figure 5: Fourier transforms of the EXAFS signals of method ET36 shown in Figure 4. Experimental (—) and fitted (---) curves.

Table VI: Fit parameters for the Mo signals, the symbols are indicated in Table IV

Method	n	Element	R <sub>f</sub> (nm)	2σ <sup>2</sup> (10 <sup>-4</sup> nm <sup>2</sup> )
T215	0.2	O	0.162	0.1
	1.7	Si	0.254	0.2
	3.8	Mo	0.270	0.5
	5.6	Mo	3.123	0.8
ET36	0.2	O	0.161	0.3
	0.6	Si	0.254	0.3
	3.8	Mo	0.273	0.7
	2.7	Mo	3.144	0.8
ET215	0.1	O	0.162	0.1
	2.7	Si	0.254	0.3
	2.1	Mo	0.269	0.7
	1.4	Mo	3.152	0.7

The methods T215 and ET36 show remarkable resemblance: the number and distances found for the first neighbouring atoms at 2.7 nm are almost equal (see Table VI). The position of the first peak in the Fourier transforms coincides with the bond distance for Mo-Mo (Table VI). This distance is similar to the value found for the first neighbouring atom for a bcc Mo structure. We conclude that the number of surrounding atoms is different for all methods. The Mo atoms from method T215 have 5.6 second neighbours and from method ET36 only 2.7.

The difference between the Mo structures is best displayed in the Fourier transforms of the EXAFS signal (Figure 6). The positions of the peaks in Figure 6 are shifted not phase shift

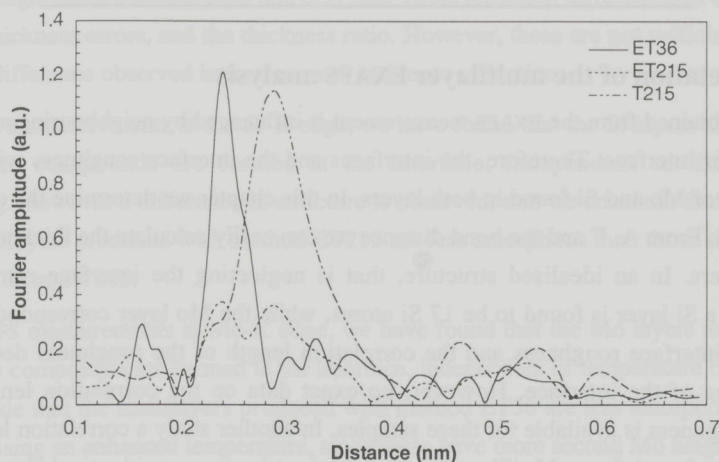


Figure 6: Fourier transforms of the fitted EXAFS signals of the Mo structure of method ET36, ET215 and T215.



corrected, the distances do not coincide with the distances in Table IV. The structure of the multilayer produced with method ET215 shows a result that combines these two methods. For the multilayers deposited at 215°C without etching, the number of second neighbours, indicated by the peak in Figure 6 at  $R_2 = 0.29$  nm, is higher than for multilayers deposited at room temperature with etching. Therefore, we conclude that the Mo layer of the temperature optimized samples are less amorphous. The difference in structure between method ET215 and T215 could be caused by the ion-etched Si layer on which the Mo layer is deposited, because the Mo layer are both deposited at 215°C and not ion-etched. The layers deposited at room temperature are more amorphous than the layers deposited at increased temperature and are therefore preferred for the production of Mo/Si multilayers.

The fractions of atoms in the Mo structure are calculated with a method similar to that used for the Si structure. Taking into account neighbouring atoms up to a distance of 0.6 nm, the atomic fractions are calculated (Table VII). The fraction of Si atoms surrounding the Mo atoms is found to be independent of the temperature or the use of ion-etching. In section 4 we discuss the effect of the interface and interface roughness on these fractions. With all deposition methods, we observe a smaller fraction of O in the Mo layers than in the Si layers as described in section 3.3.1. This has been expected because of the lower activation energy for the formation of Mo-O compared to Si-O.

Table VII: Atomic percentage of Si, Mo, and O surrounding the Mo atoms.

Method	Si (%)	Mo (%)	O (%)
T215	32	68	0.3
ET36	30	69	0.2
ET215	32	68	0.1

## 5. Interpretation of the multilayer EXAFS analysis

The model obtained from the EXAFS measurement is influenced by neighbouring atoms across the multilayer interface. Therefore, the interfaces and the interface roughness will influence the fractions of Mo and Si found in both layers. In this chapter we determine the contribution by this effect. From  $\Lambda$ ,  $\Gamma$  and the bond distance we can easily calculate the thickness of the Si and Mo layers. In an idealised structure, that is neglecting the interface roughness, the thickness of a Si layer is found to be 17 Si atoms, while the Mo layer corresponds to 10 Mo atoms. The interface roughness and the correlation length of the roughness determine the effective area of the interface. However, no exact data on the correlation lengths of the interface roughness is available for these samples. In another study a correlation length of 0.1 nm has been found for a Mo/Si multilayer produced using an identical deposition and ion-etching procedure [8]. With the measured interface roughness and the assumption for the

correlation length of 0.1 nm the effective area increases with a factor of two compared to an idealized interface. We now find that the presence of the interface results in approximately 25% of Si atoms surrounding the Mo atoms and 13% of Mo atoms surrounding the Si atoms.

These percentages indicate that the 30% of Si atoms surrounding the Mo atoms is primarily due to the interface (Table VII). Therefore we conclude that only a low fraction of Si atoms ( $\approx 5\%$ ) diffuses into the Mo layer and the amount of diffusion is independent on temperature. For multilayers produced at enhanced substrate temperature without etching, the low interdiffusion into the Mo layer is consistent with literature [27]. From the 25-40% of Mo atoms surrounding the Si atoms, only 13% can be explained by the interface effect (Figure 3). The remaining 12 to 27% is due to diffusion of Mo into the Si layer. The amount of interdiffusion in the Si layer is dependent on the temperature. Computer simulations show that the effect of Mo atoms in the Si layer hardly influences the near normal incidence reflection, e.g. a multilayer with 12% of Mo in the Si layer has a calculated reflection of 59% compared to a reflectivity of 55% for the Si layers with 27% of Mo.

With both EXAFS measurements the Si-Mo bond distance is determined. In the Si layer this distance is found to be 0.28 nm while amounting 0.25 nm in the Mo layer. This clearly indicates that the Mo-Si bonds have a different structure in different layers. We suppose that the bond distance of Si-Mo changes from 0.25 nm at the Mo side to 0.28 nm at the Si side of the interface.

## 6. Conclusions

From small angle reflectivity measurements we conclude that multilayers produced with temperature optimization (at the optimal value of 215 °C) or ion-etching, have nearly equal interface roughnesses between 0.35 and 0.37 nm. There are small differences in the d-spacing, the layer thickness errors, and the thickness ratio. However, these are not sufficient to explain the major difference observed in near normal incidence reflection.

From EXAFS measurements at the Si-K edge, we have found that the Si layers are amorphous and that no compounds are formed at the interface, independent on temperature or ion-etching. However a difference in structure is observed, and we conclude that the Si layers in the multilayers produced with method ET215 are less amorphous than those produced with method ET36 and T215.

From EXAFS measurements at Mo-K edge, we have found that the Mo layers are amorphous and that no compounds are formed at the interface, independent of temperature or ion-etching. We conclude that the multilayers produced with method ET36 are less amorphous than those produced using an enhanced temperature, since these have more second Mo neighbours.

We do find an increased amount of diffusion for the multilayers produced at the optimal temperature of 215 °C. In this case the Si atoms are surrounded by 41% of Mo atoms



compared to 25% of Mo atoms in the case of deposition at room temperature with ion-etching. For the Mo atoms no significant difference in the surrounding by Si is found between the methods tested. The fraction is mainly determined by a contribution of Si atoms across the interface. For the Si layer this contribution is small (13%) compared to the fraction of Mo in the layer. For the Si layer the fraction of Mo atoms in the Si layer ranges from 12% for method ET36 to 27% for method ET215. At least half of the fraction is caused by interdiffusion

Furthermore, we find that ion-etching of the Si interfaces not only reduces the roughness, but also results in a reduced fraction of oxygen (0.5%) in the Si layer. The inclusion of 4.7% oxygen in the Si layer, when the multilayers are produced at 215 °C without ion-etching, results in higher absorption of 13.5 nm radiation, and consequently, in a 9% reduction of the reflectivity. This is in full agreement with the loss in reflectivity observed experimentally. Moreover, due to the ion etching process, the amorphous Si structure is found to be more compact, while the Si-O bond distance has larger values compared to the non-etching method.

Multilayers that have been produced with ion-etching at room temperature show maximal reflectivity for soft x-rays because of the low fraction of O and Mo in the Si layer and a more amorphous Mo layer compared to the temperature optimized methods.

## 7. Acknowledgements

We acknowledge the contribution of Yu. Platonov from the Institute for Physics of Microstructures (Nizhny Novgorod, Russia) performing the Cu-K $\alpha$  measurements. We thank Daresbury SRS for making available the facilities to carry out the EXAFS measurements and the use of the Chemical Database Service. These investigations, within the framework of a research project of FOM (the Foundation for Fundamental Research on Matter), are supported by STW (the Netherlands Technology Foundation) and the Dutch Government in the context of EUREKA.

## 8. References

1. E. Louis, F. Bijkerk, L. Shmaenok, H.-J. Voorma, M. v.d. Wiel, R. Schlatmann, J. Verhoeven, E. v. d. Drift, J. Romijn, B. Rousseuw, F. Voß, R. Desor, B. Nikolaus, *Microelectron. Eng.* **21** (1993) 67-70
2. T. Barbee, *Opt. Eng.* **25** (1986) 898-914
3. E. Spiller, A. Segmüller, J. Rife and R.-P. Heilich, *Appl. Phys. Lett.* **37** (1980) 1048-1050
4. E. Louis, H.-J. Voorma, N.B. Koster, F. Bijkerk, and M. v.d. Wiel, *Microelectron. Eng.* **23** (1994) 215-218
5. E. Louis, H.-J. Voorma, N.B. Koster, F. Bijkerk, Yu. Ya. Platonov, S. Yu. Zuev, S. Andreev, E. Shamov, and N. Salashchenko, *Microelectron. Eng.* **27** (1995) 235-238
6. E. Louis, H.-J. Voorma, N.B. Koster, F. Bijkerk, Yu. Ya. Platonov, G.E. van Dorssen and H.A. Padmore, *Physics of X-ray Multilayer Structures*, O.S.A. Technical Digest Series, Vol. **6** (1994) 35-39
7. A. Klöidt, K. Nolting, U. Kleineberg, B. Schmiedeskamp, U. Heinzmann, P. Müller, M. Kühne, *Appl. Phys. Lett.* **58** (1991) 2601-2603

8. R. Schlatmann, J.D. Schindler, J. Verhoeven, Physics of X-ray Multilayer Structures, O.S.A. Technical Digest Series, Vol. 7, (1992) PD6-2
9. R. Schlatmann, C. Lu, J. Verhoeven, E. Puik, M. v. d. Wiel. Appl. Surf. Sci. **78** (1994) 147-157
10. A. Akhsakhalyan, A. Fraerman, N. Polushkin, Yu.Ya. Platonov, N. Salashchenko, Thin Solid Films **203** (1991) 317-326
11. H.-J. Voorma, E. Louis, N.B. Koster, F. Bijkerk, and M. v.d. Wiel, Physics of X-ray Multilayer Structures, O.S.A. Technical Digest Series, Vol. 6 (1994) 134-137
12. E. Spiller, A. Rosenbluth, Opt. Eng. **25** (1986) 954-963
13. H.-J. Voorma, E. Louis, N.B. Koster, F. Bijkerk and M. v.d. Wiel, Proc. MRS sym. **382** (1995) 375-380
14. H.A. Padmore, Internal SRRD report S/HAP/4.11.92 (1992)
15. E. Stern, Phys. Rev. B **11** (1974) 3027-3037
16. F. Lytle, D. Sayers and E. Stern, Phys. Rev. B **11** (1975) 4825-4835
17. E. Stern, D. Sayers and R. Lytle, Phys. Rev. B **11** (1975) 4836-4846
18. N. Binsted, J. Campbell, S. Gurman and P. Stevenson, DRAL Daresbury Laboratory EXCURV92 program (1991)
19. N and C have been examined but could not be fitted to both the EXAFS signal and its Fourier transform. Also Kr has been examined for the method where ion etching is used, but could not be detected.
20. A. Smith, M. Roper, H. Padmore, Nucl. Instrum. Meth. B. **97** (1995) 579-584
21. S. Pizzini, K. Roberts, G. Greaves, N. Barrett, I. Dring and R. Oldman, Proc. 2nd Workshop on Synchrotron Light: Applications and Related Techniques, Campinas (1989)
22. C. Kittel, Introduction to Solid State Physics, John Wiley & Sons, sixth edition (1986)
23. G. Greaves, X. Jiang, R. Jenkins, E. Holzenkampfer, and S. Kalbitzer, J. Phys. **12** (1986) C8-853
24. A. McMahan, J. Klepeis, M. v. Schilfgaarde, M. Methfessel, Phys. Rev. B **50** (1994) 10742-10760
25. J. Cheng, H. Cheng, and L. Cheu, J. Appl. Phys. **61** (1989) 221-230
26. K. Holloway, K. Do, and R. Sinclair, J. Appl. Phys. **65** (1989) 474-480
27. M. Stearns, C. Chang, D.G. Stearns, J. Appl. Phys. **71** (1992) 187-194
28. The experimental procedure for flushing with Kr gas is as follows. The pressure in vacuum system is increased from  $2 \times 10^{-8}$  mbar to  $3 \times 10^{-5}$  mbar with Kr followed by flushing for 5 minutes. Then the system is evacuated to  $2 \times 10^{-8}$  mbar and the vacuum is analysed with a mass spectrometer. This whole procedure is repeated 40 times, corresponding to the ion polishing method. After this, the vacuum is analysed with a mass spectrometer at  $2 \times 10^{-8}$  mbar.
29. G. Diakun, G. Greaves, S. Husnain and P. Quin, Technical Memorandum Daresbury Laboratory, DL/SCI/TM38E (1984)

## 2. Introduction

The feasibility of extreme ultra-violet lithography (EUVL) is continually studied, because EUVL is a promising candidate for the fabrication of micro-circuit devices with feature sizes of 0.1  $\mu\text{m}$  and below [1, 2, 3]. Presently, these studies focus on debris-free laser plasma EUV sources with a high average power, fabrication and technology of mirror substrates, as well as fabrication of high reflectivity defect-free reflectors made including options for mask repair.

The specifications for the multilayer reflection mask are determined by the requirements for the EUV system under study, and depend on the configuration of the optics, the near-normal incidence reflectivity and the  $d$ -spacing of the multilayer structures. The first requirement for a





## Fabrication and analysis of Extreme Ultra-violet reflection masks with patterned W/C absorber bi-layers

### 1. Abstract

We report on a novel procedure developed for the fabrication of reflection masks for Extreme UV lithography. The procedure involves the deposition and patterning of an absorber bi-layer (40 nm W and 25 nm C) on Mo/Si multilayer blanks. The C layer is used to protect the underlying Mo/Si multilayer structure during processing and repair. The pattern is written with an e-beam pattern generator into EPR resist and is transferred into the absorber bi-layer with three consecutive RF etching processes.

We have investigated the effect of the full mask making procedure on the multilayer reflectivity using 13 nm radiation. The procedure causes some oxidation of the top Si layer of the multilayer, an effect which is confirmed by XPS measurements. However, the method does not affect the multilayer reflectivity to within narrow tolerances.

The profiles of patterns in the absorber layer are inspected with a SEM, showing patterns with a feature size of 250 nm and side wall slope angles of 80°.

An indication is found that cleaning of the substrate with ion etching prior to the fabrication of the mask blanks reduces the defect density.

### 2. Introduction

The feasibility of extreme ultra-violet lithography (EUVL) is extensively studied, because EUVL is a promising candidate for the fabrication of microcircuit devices with feature sizes of 0.1  $\mu\text{m}$  and below [1,2,3]. Presently, these studies focus on debris-free laser plasma EUV sources with a high average power, fabrication and metrology of mirror substrates, as well as fabrication of high reflectivity defect-free reflection masks including options for mask repair.

The specifications for the multilayer reflection mask are determined by the requirements for the EUVL system under study, and depend on the configuration of the optics, the near-normal incidence reflectivity and the d-spacing of the multilayer structures. The first requirement for a



reflection mask is a high reflectivity of the Mo/Si multilayer after mask fabrication. Reflectivity values should be similar to the more than 60%, which has been reported for Mo/Si multilayers [4,5]. The second requirement concerns the matching of the d-spacing of the mask to the d-spacing of the other multilayer mirrors in the optical system. It is noted that for example a 1% shift in the d-spacing of the mask causes an 8% reduction of the throughput of a 7-mirror EUVL system. A reduced reflectivity of the mask is less critical: a 5% reduction of the mask reflectivity causes a proportional reduction of the total throughput.

For the fabrication of reflection masks two techniques have been suggested [6,7]. Firstly, a mask pattern can be made by local removal of the multilayer structure. However, in this case repair of opaque defects is virtually impossible, because of the inability to deposit a multilayer locally. The second option consists of deposition of an absorber layer on top of the multilayer structure, which is then removed locally using standard lithographic techniques. We prefer to use this last option, because it enables repair of both clear and opaque defects.

In this paper a novel bi-layer absorber, consisting of W and C, is proposed and investigated in detail. The W layer is used as absorber layer, providing the required mask contrast, while the C layer is primarily used to protect the multilayer structure during patterning and repair.

### 3. Mask production

#### 3.1 Multilayer production

The Mo/Si multilayer structures have been produced using e-beam evaporation. A double chamber coating facility has been used, of which the lower chamber contains an e-gun and the multilayer materials and the upper chamber an in-situ reflectometer, an ion gun, and a substrate holder. The coating facility has been described in detail in reference 8.

The reflectometer is used to control the multilayer d-spacing during deposition. A d-spacing of 7.1 nm is selected for the multilayer structures, which is obtained using N-K radiation (3.16 nm) and an angle of 13.5° with respect to the substrate for both the detector and the x-ray source. Ion etching is used to reduce the interface roughness of the multilayer structures. The ion-beam parameters, 300 eV Kr<sup>+</sup>-ions at an angle of 45°, result in an interface roughness of 0.4 nm rms. The top layer consists of 4.9 nm Si, which is a better top material than Mo since it forms a thinner cap-layer of oxide [9].

For testing of all individual steps and of the full procedure of mask fabrication, we use 40-period Mo/Si multilayer structures that are characterized before and after each process step. For the final test of the mask fabrication procedure we use samples that are cut into two pieces, of which one half is prepared using the mask fabrication procedure, and the other half is not processed and used as a reference.

### 3.2 Production of absorber bi-layer

The Mo/Si multilayers are overcoated with a 25 nm thick C layer and a 40 nm W thick layer. Calculations show that these layer thicknesses and materials ensure a mask contrast of 40, which is assumed to be sufficient for most EUV photoresist materials. The C layer is deposited in the e-beam evaporation set-up described above. The W layer is deposited with RF sputter deposition ( $0.93 \text{ W/cm}^2$ ) using an Ar pressure of 3.3 Pa

### 3.3 Patterning

After deposition of the absorber bi-layer on top of the multilayer structure we produce the mask pattern by local removal of this absorber using standard lithographic techniques. The full procedure of mask patterning is shown in Figure 1. It includes a prebake, an exposure with an e-beam pattern generator (EBPG, Cambridge-Leica) of EPR electron beam resist, a postbake, development in PGMEA [10], and a descum in a low pressure  $\text{O}_2$ -plasma. To transfer the pattern from the resist into the W layer, an  $\text{SF}_6$ -plasma is used, followed by a low pressure  $\text{O}_2$ -plasma to remove the residual C layer. The process conditions are listed in Table I.

A parameter that is important during the patterning process is the etch rate selectivity, because

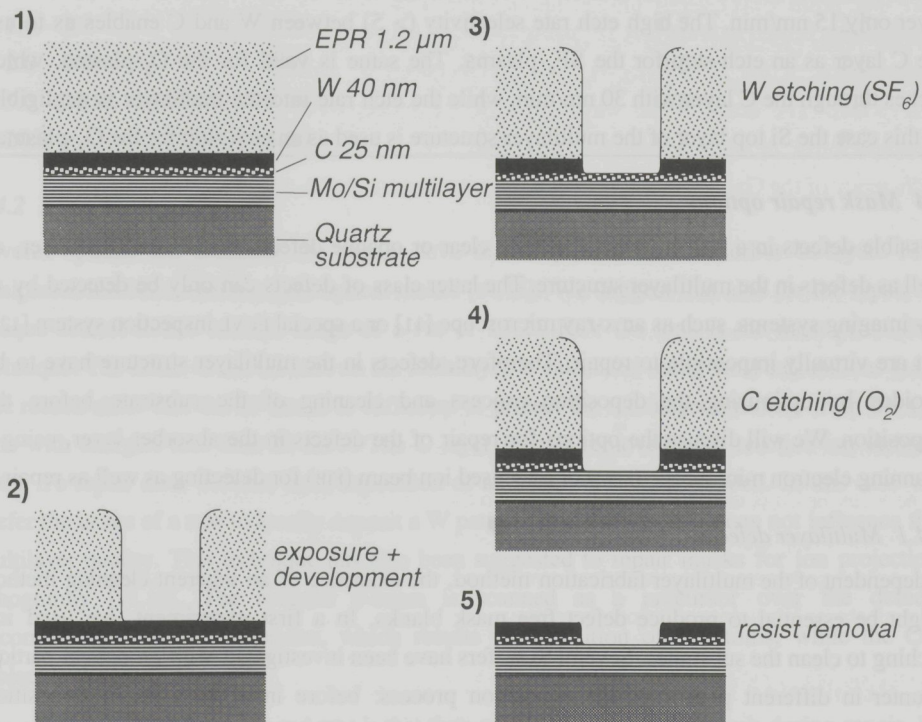


Figure 1: Schematic representation of the patterning process of EUVL reflection masks.



Table I: Summary of conditions used for resist processing and pattern transfer.

Process		Conditions	Gas composition	Gas pressure
Resist	spinning	3000 rpm Thickness : 1.2 $\mu\text{m}$		
	prebake	120°C for 15 min		
	exposure	electrons: 100 kV dose: 4 $\mu\text{C}/\text{cm}^2$		
	postbake	90°C for 5 min		
	development	2 min in PGMEA		
Descum	O <sub>2</sub> -plasma	0.06 W/cm <sup>2</sup>	O <sub>2</sub> : 20 sccm	0.3 Pa
W etching	SF <sub>6</sub> -plasma	0.12 W/cm <sup>2</sup>	SF <sub>6</sub> : 12 sccm	1.0 Pa
			He: 9.5 sccm	
C etching	O <sub>2</sub> -plasma	0.06 W/cm <sup>2</sup>	O <sub>2</sub> : 20 sccm	0.4 Pa

this determines the suitability of the C layer as an etch stop for the SF<sub>6</sub>-plasma. The etch rate of the SF<sub>6</sub>-plasma into the EPR resist is 90 nm/min, into the W layer 80 nm/min, and into the C layer only 15 nm/min. The high etch rate selectivity (> 5) between W and C enables us to use the C layer as an etch-stop for the SF<sub>6</sub>-plasma. The same is valid for the O<sub>2</sub>-plasma, which etches through the C layer with 30 nm/min, while the etch rate into the multilayer is negligible. In this case the Si top layer of the multilayer structure is used as an etch stop for the O<sub>2</sub>-plasma.

### 3.4 Mask repair options

Possible defects in a reflection mask can be clear or opaque defects in the absorber layer, as well as defects in the multilayer structure. The latter class of defects can only be detected by x-ray imaging systems, such as an x-ray microscope [11] or a special EUVL inspection system [12], but are virtually impossible to repair. Therefore, defects in the multilayer structure have to be avoided by optimizing the deposition process and cleaning of the substrate before the deposition. We will discuss the options for repair of the defects in the absorber layer, using a scanning electron microscope (SEM) or a focused ion beam (FIB) for detecting as well as repair.

#### 3.4.1 Multilayer defects

Independent of the multilayer fabrication method, the existence of an inherent cleaning method might be essential to produce defect free mask blanks. In a first experiment, we used ion etching to clean the substrates. Several Si wafers have been investigated with an optical particle counter in different phases of the deposition process: before installation in the deposition system, after installation, pump down and venting, after ion etching, and after deposition of several periods of a Mo/Si multilayer. The last two phases include installation, pump down and

venting. Ion etching is performed using 500 eV Kr<sup>+</sup> ions for 5 minutes. The deposition of the multilayers is performed according to the procedure described above.

The results, listed in Table II, indicate that the substrate is cleaned using ion bombardment. It is noted that the cleaning mechanism induced by ion bombardment is similar to the glow discharge used for the fabrication of optical elements [13]. Due to the absence of cleanroom conditions, the differences between the last two columns in Table II are not significant. Separate tests have been performed, using 4 and 16 period multilayer structures, showing that the defect density does not increase with increasing number of layers. We obtained an average integrated defect density of less than 100/cm<sup>2</sup>. It is emphasized that this value has been obtained without the use of a cleanroom around the deposition system. Such a cleanroom is currently being installed.

Table II: The defect density after different process steps of the fabrication of mask blanks.

Particle size ( $\mu\text{m}$ )	Number of particles per cm <sup>2</sup>			
	from manufacturer	after installation, pump down and venting	after deposition and polishing of Si	after deposition and polishing of Si + Mo + Si
0.2 - 1.0	0.00	76	5.6	7.6
1.0 - 2.0	0.00	51	0.7	2.5
2.0 - 5.0	0.02	24	0.5	1.8
5.0 - 20.0	0.00	6	0.8	0.9
20.0 >	0.00	0.3	0.3	0.2

### 3.4.2 Absorber layer defects

Several options are available for repair EUVL masks [6] and our absorber bi-layer. FIB equipment has been used to repair optical masks [14,15]. We suggest that also for the repair of opaque defects in EUV masks, usage of a FIB of 15-25 KeV Ga ions is the most promising technique. The effect of the Ga ions on the multilayer is calculated using TRIM calculations [16]. The results show that the 25 nm C is sufficient to protect the multilayer structure from the Ga ions with energies less than 20 KeV. The C layer is later removed with reactive ion etching (RIE). To repair clear defects, local deposition of an absorber layer is needed. In this case we prefer the usage of a SEM to locally deposit a W pattern, because the SEM does not influence the multilayer quality. This technique has also been suggested to repair masks for ion projection lithography [17,18]. The focused e-beam is scanned as a precursor over the defect, decomposing W(CO)<sub>6</sub> molecules, which results in deposition of W atoms, while the CO molecule desorbs.

The advantage of both the FIB and SEM is that they enable imaging of the mask during repair. In order to repair both defects in one set-up, designs are under construction to combine both a FIB and a SEM [19].



## 4. Mask characterization

### 4.1 Small-angle reflectivity measurements

Small-angle reflectivity measurements ( $\theta$ - $2\theta$  scans) with Cu- $K_{\alpha}$  radiation ( $\lambda = 0.154$  nm) are used to determine the d-spacing and the interface roughness of the multilayer structures. For these measurements an angular resolution of better than  $0.01^{\circ}$  is needed for the reflectometer, which is obtained with a Si-crystal monochromator in combination with two slits [20,21,22].

The multilayer d-spacing is determined from the positions of at least three Bragg maxima in a  $\theta$ - $2\theta$  scan. The interface roughness and thickness ratio are determined using a more advanced method of analysis of the small-angle reflectivity measurements, as has been described in references 23 and 24.

### 4.2 Soft x-ray reflectivity measurements

Soft x-ray reflectivity measurements are carried out at the bending magnet reflectometer beam line of HASYLAB (Desy, Hamburg, Germany) [25,26]. The angular range in the reflectometer can be varied between  $0^{\circ}$  and  $78^{\circ}$  with respect to the surface. The spot size of the beam on the sample is  $0.5 \times 1.5$  mm. In order to measure the reflectivity of the mask samples the absorber bi-layers are removed over an area of  $10 \times 10$  mm. The near-normal incidence reflectivity of the multilayers is then measured at  $78^{\circ}$  using radiation between 11.8 nm and 14.5 nm. The angular dependence of the reflectivity is measured between  $0^{\circ}$  and  $73^{\circ}$  at a fixed wavelength of 12.78 nm. The error in the wavelength of the reflectometer set-up is less than 1%. The absolute error in the reflectivity is less than 1%, and is caused by local variations in the efficiency of the GaAsP-Schottky-diode detector and by the beam intensity profile.

### 4.3 X-ray photo-electron spectroscopy

The chemical compositions of the top layer of the mask and reference samples are investigated with x-ray photo-electron spectroscopy (XPS). For this work a PHI 5400 ESCA (Perkin-Elmer at Delft University of Technology, Delft, The Netherlands) is used, which contains a Mg x-ray source ( $\lambda = 0.99$  nm) and a concentric hemispherical analyser. The XPS measurements are performed with a step size of 0.1 eV and a pass energy of 34.75 eV.

The x-ray beam is used at  $15^{\circ}$  with respect to the substrate. In the measurements performed, the thickness investigated is limited by the escape depth of the photo-electrons (4 nm). The analysis of these measurements is performed assuming an exponential decay as a function of depth for the electrons from deeper below the surface.

## 5. Results and discussion

Firstly, each step of the mask fabrication process is investigated separately by comparing the d-spacings before and after each step. Secondly, the soft x-ray reflectivity of the mask and

reference samples are measured and analysed. The samples are also investigated with XPS measurements. Finally, we inspect the profile of the patterns in the absorber layer with a SEM.

### 5.1 Individual process steps of the mask fabrication procedure

As has been indicated before, a change in d-spacing due to mask fabrication is the most important parameter to investigate. The d-spacing may change when the multilayer is heated, therefore, we investigate two process steps that influence the temperature of the mask samples. The first one is the effect of the deposition and the removal of the absorber bi-layer (40 nm W, 25 nm C). The reflectivity of the multilayer structures is measured before and after this production step and shown in Figure 2. We conclude that the deposition and etching of the absorber bi-layer have little influence on the d-spacing of the multilayer structures. A possible variation in the d-spacing is found to be within 0.15%, a value which is determined by the resolution of the reflectometers used.

The second process step investigated is baking of the EPR resist and consequently the Mo/Si multilayer. We have found that increasing the temperature of a Mo/Si multilayer above 175°C for 60 minutes, which corresponds to values used for most classical resists, decreases the d-spacing with 1.8%. Since, this is not acceptable for the production of reflection masks, we have tested several other temperatures (90°C-130°C) and baking times (5-15 minutes). The multilayer structure that is baked for 15 min at 130°C, has the same d-spacing after baking compared to the d-spacing before, within the 0.25% error in the measurements of the d-spacings corresponding to the resolution of the reflectometers.

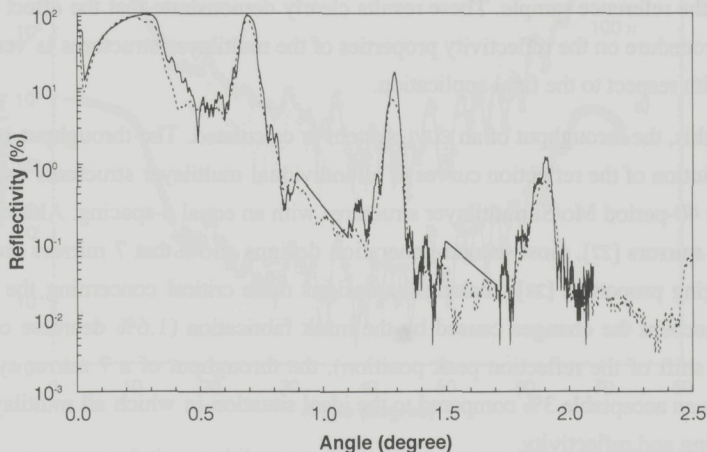


Figure 2: Small-angle reflectivity measurement of a multilayer structure before (solid line) and after (dashed line) deposition and removal of the absorber bi-layer.



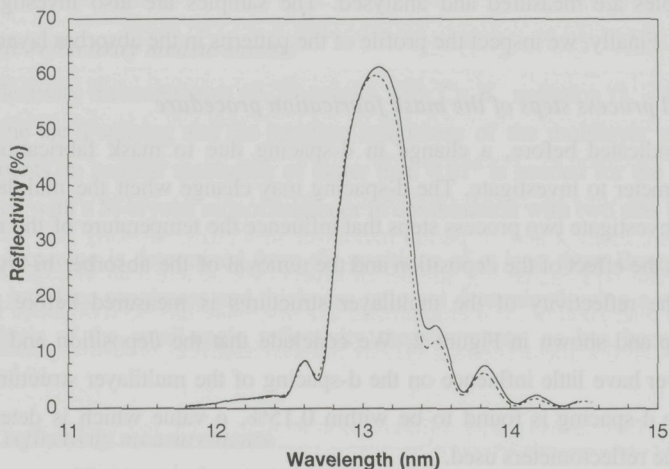


Figure 3: Near-normal incidence reflectivity measurement ( $78^\circ$ ) before (solid line) and after (dashed line) the full mask fabrication process.

### 5.2 Full mask fabrication procedure

For the purpose of testing the overall procedure half of the sample is prepared using the mask fabrication procedure, while the other half is not processed and used as a reference sample. After this, the soft x-ray reflectivities of both samples are measured at near normal incidence ( $78^\circ$ ). From the results, shown in Figure 3, we conclude that the central wavelength of the reflection peak of the mask sample shifts 0.01 nm and the reflectivity decreases with 1.6% compared to the reference sample. These results clearly demonstrate that the effect of the mask fabrication procedure on the reflectivity properties of the multilayer structures is very small and acceptable with respect to the final application.

To illustrate this, the throughput of an EUVL system is calculated. The throughput is determined by the convolution of the reflection curves of all individual multilayer structures using 13.1 nm radiation and 40-period Mo/Si multilayer structures with an equal d-spacing. Although our EUVL system has 4 mirrors [27], most second-generation designs show that 7 mirrors are needed for suitable imaging properties [28], making the designs more critical concerning the throughput. Taking into account the changes caused by the mask fabrication (1.6% decrease of reflectivity and 0.01 nm shift of the reflection peak position), the throughput of a 7 mirror system would decrease with an acceptable 3% compared to the ideal situation in which all multilayers have an equal d-spacing and reflectivity.

#### 5.2.1 Analysis using soft x-ray reflectivity

The difference in soft x-ray reflectivity between the mask and reference sample is investigated in more detail using angular reflectivity scans ( $\theta$ - $2\theta$ ). We expect that the mask fabrication

process only affects the top layer of the multilayer structure. If this is the case, a difference between the reflectivity signals of the two samples will be observed just above the critical angle. If the entire multilayer structure is changed by the process, differences for all angles will be observed, especially at the side fringes of the Bragg peaks. Therefore, we measure the angular dependence ( $\theta$ - $2\theta$  scan) of the reflectivity between  $0^\circ$  and  $73^\circ$  using 12.78 nm radiation.

The angular scan of both the reference (curve a) and the mask sample (curve b) are displayed by the lines in Figure 4. We observe a large difference in the value of the reflectivity between both multilayer structures at angles between  $10^\circ$  and  $35^\circ$ . However, the shapes of the reflection curves are almost similar, indicating that indeed only the top layers of these multilayer structures are different.

The angular scans in Figure 4 are analysed further using the following fit procedure. Firstly, we take into account that after deposition the outermost part of the Si top layer oxidizes to a thin  $\text{SiO}_2$  layer. This oxidation is confirmed by XPS measurements described in the next paragraph. Secondly, we fit the layer thicknesses of the multilayer structure to the measured reflectivity signals. From the fitted thicknesses small layer thickness errors are found, which are also observed in the in-situ reflectivity signal, indicating that the fit is accurate. Comparing all individual layer thicknesses of both samples, we conclude that only the top layer is affected by the mask fabrication process. The top layers of the reference samples consist of 1 nm  $\text{SiO}_2$  and 4 nm Si, while the top layers of the mask samples consist of 4 nm  $\text{SiO}_2$  and 1 nm Si. The error in these thicknesses is found to be 0.1 nm. These results indicate that the  $\text{O}_2$ -plasma, used to

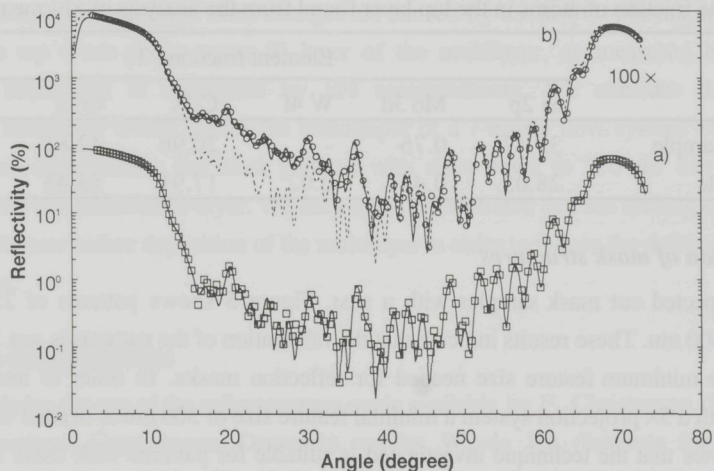


Figure 4: Measurement of the multilayer reflectivity between  $0^\circ$  and  $73^\circ$  using 12.78 nm radiation a): before mask production (solid line,  $\square$  represent data obtained from the fit), b): after mask production (solid line,  $\circ$  represent data obtained from the fit). For clarity curve b) has been multiplied by a factor of 100. To facilitate comparison, curve a) is shown again (dotted line), multiplied by a factor of 100.



remove the residual C layer, almost completely oxidizes the Si top layer. Using these layer thicknesses, the soft x-ray reflectivity of the multilayer structure is calculated. The calculations show that the 4 nm SiO<sub>2</sub> top layer reduces the reflectivity with 1.6% and shifts the position of the reflection peak with 0.01 nm, which corresponds to the values given in section 4.2. Thus, the oxidation fully explains the changes of the reflectivity properties of the mask.

### 5.2.2 Analysis using XPS

XPS measurements are carried out to investigate the difference in chemical composition of the top layers, i.e. the top 4 nm of the reference and the mask samples. The results of the XPS measurements are listed in Table III. The most remarkable difference between the mask and reference samples is the difference in the Si and the O content. While the reference samples have a Si:O ratio of 5:6, the mask samples have a Si:O ratio of almost 1:2, indicating a complete oxidation of from the top 4 nm of Si that can be analysed by XPS. We also conclude that all samples contain C, probably from organic contamination by the atmosphere. Calculations show that this contamination hardly influences the reflectivity of a Mo/Si multilayer in the wavelength range between 12 and 14 nm. The mask samples also show minor fractions of W and F, caused by the absorber layer and the SF<sub>6</sub>-plasma, respectively.

We conclude that the top layers of the reference samples consist of 1 nm SiO<sub>2</sub> on top of Si. The top 4 nm of the mask samples are completely oxidized. Thus the XPS data confirm the results obtained from the soft x-ray reflectivity measurements.

Table III: The fraction of atoms in the top layer found from the analysis of XPS measurements.

	Element fraction (%)					
	Si 2p	Mo 3d	W 4f	C 1s	O 1s	F 1s
Reference sample	35.47	0.76	-	20.96	42.81	-
Mask sample	28.05	0.44	0.02	17.91	53.43	0.15

### 5.3 Inspection of mask structures

We have inspected our mask samples with a SEM. Figure 5 shows patterns of 250 nm with spacings of 500 nm. These results indicate that the fabrication of the patterns is not limited with respect to the minimum feature size needed for reflection masks. In order to image 100 nm structures with a 5× projection system a minimal feature size of 500 nm is needed on the mask. Figure 5 shows that the technique investigated is suitable for patterns with these dimensions. For EUVL systems the profile of the absorber layer partly determines the quality of the image. SEM analysis shows that the absorber layer profile has a slope angle of the side walls of at least 80°.

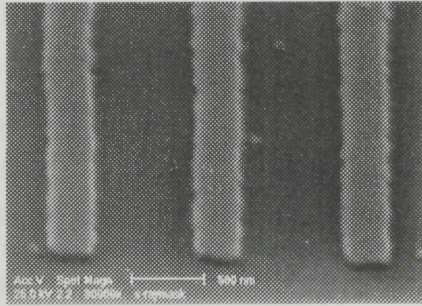


Figure 5: SEM measurement of mask structures on a 40 period Mo/Si multilayer mask blank. The feature sizes are 250 nm lines and 500 nm spacings.

## 6. Conclusions

We have produced and analysed EUVL reflection masks with a new absorber bi-layer. The bi-layer consists of 25 nm C and 45 nm W, providing a mask contrast of 40. Forty-period Mo/Si multilayers have been used as mask blanks. The W layer is used to ensure sufficient contrast for the 13 nm radiation, while the C layer is used to protect the multilayer during patterning and repair. Patterns in this absorber bi-layer have been produced using an EBPG and three consecutive etch steps. After the full fabrication procedure, the near normal incidence reflectivity of the mask samples has been measured and is found to remain constant within 1.6%. The positions of the reflection peaks shifted a minor 0.01 nm compared to the unprocessed reference samples. Both changes are caused by the last O<sub>2</sub>-plasma applied, which oxidizes the top 4 nm of the upper Si layer of the multilayer, as measured by soft x-ray reflectivity scans and is confirmed by XPS measurements. We consider these changes acceptable, since they would reduce the throughput of a 7-mirror EUVL system with only 3%. SEM analysis demonstrates that mask patterns with sizes down to 250 nm can be faithfully fabricated into this absorber bi-layer. We have also demonstrated that ion etching can be used to clean the substrate before deposition of the multilayer in order to reduce the defect density of the mask blanks.

## 7. Acknowledgements

We acknowledge the use of the reflectometers made available by F. Christensen (Danish Space Research Institute, Copenhagen, Denmark) and by W. de Jeu (Institute for Atomic and Molecular Physics, Amsterdam, The Netherlands). We also acknowledge the XPS measurements performed by E. Fakkeldij (Delft University of Technology, The Netherlands). These investigations within the framework of FOM (the Foundation for Fundamental Research on Matter) are supported by STW (the Netherlands Technology Foundation) and the Dutch government in the context of EUREKA.



## 8. References

1. M. Ito, S. Katagiri, H. Yamanashi, E. Seya, T. Ogawa, H. Oizumi, and T. Tersasawa, *OSA Proc. Extreme Ultraviolet lithography* **4** (1996) 9-12
2. F. Bijkerk, L. Shmaenok, E. Louis, H.-J. Voorma, N.B. Koster, C. Bruineman, R.K.F.J. Bastiaensen, E.W.J.M. van der Drift, J. Romijn, L.E.M. de Groot, B.A.C. Rousseeuw, T. Zijlstra, Yu.Ya. Platonov, and N.N. Salashchenko, *Microelectron. Eng.* **30**, 183 (1996)
3. D.A. Tichenor, A.K. Ray-Chaudhuri, G.D. Kubiak, K.B. Nguyen, S.J. Haney, K.W. Berger, R.P. Nissen, Y.E. Perras, P.S. Jin, L.I. Weingarten, P.N. Keifer, R.H. Stulen, R.N. Shagam, W.C. Sweatt, T.G. Smith, O.R. Wood II, T.E. Jewell, and F. Zernike, *OSA Proc. Extreme Ultraviolet lithography* **4** (1996) 2-6
4. E. Louis, H.-J. Voorma, N.B. Koster, F. Bijkerk, Yu.Ya. Platonov, S.Yu. Zuev, S.S. Andreev, E.A. Shamov, and N.N. Salashchenko, *Microelectron. Eng.* **27**, 235 (1995)
5. D.G. Stearns, R.S. Rosen, and S.P. Vernon, *Appl. Opt.* **32**, 6975 (1993)
6. A.M. Hawryluk and D. Steward, *Appl. Opt.* **32**, 7012 (1993)
7. M. Ito, H. Ozumi, T. Soga, H. Yamanashi, T. Ogawa, S. Katagiri, E. Seya, and E. Takeda, *Microelectron. Eng.* **27**, 285 (1995)
8. E. Louis, H.-J. Voorma, N.B. Koster, L. Shmaenok, F. Bijkerk, R. Schlatmann, J. Verhoeven, Yu.Ya. Platonov, G.E. van Dorssen and H. Padmore, *Microelectron. Eng.* **23**, 215 (1994)
9. J.H. Underwood, E.M. Gullikson, and K. Nguyen, *Appl. Opt.* **32**, 6985 (1993)
10. PGMEA: propyleneglycol monomethylether acetate
11. J. Voss, M. Fornafett, C. Kunz, A. Moewes, M. Pretorius, A. Ranck, M. Schroeder, V. Wedemeier, J. *Electron. Spectrosc. Relat. Phenom.* (1996) in print
12. D.L. White, J.E. Bjorkholm, J. Bokor, L. Eichner, R.R. Freeman, J. Grevus, T.E. Jewell, W.M. Mansfield, A.A. Mac Dowell, E.L. Raab, W.T. Silvast, L.H. Szeto, D.M. Tennant, W.K. Waskiewics, D.L. Windt and O.R. Wood II, *Proc. Spie.* **1343**, 204 (1990)
13. D.G. Armour, *Vacuum* **43**, 117 (1992)
14. P.G. Blauner, and J. Mauer, *IBM J. Res. Develop.* **37**, 421 (1993)
15. A. Wagner, J.P. Levin, J.L. Mauer, P.G. Blauner, S.J. Kirch, and P. Longo, *J. Vac. Sci. Technol. B* **8**, 1557 (1990)
16. J. F. Ziegler, *The Stopping Range of Ions in Matter*, Vol. 2-6 Pergamon Press, 1977-1985
17. W.H. Brünger, *Microelectron. Eng.* **9**, 171 (1989)
18. K.T. Kohlmann, M. Thiemann, and W.H. Brünger, *Microelectron. Eng.* **13**, 279 (1991)
19. P.W.H. de Jager, M.C.W. Kelder and P. Kruit, *Microelectron. Eng.* **30**, 427 (1996)
20. F.E. Christensen, E. Jacobsen, P. Jonasson, M.M. Madsen, H.W. Schnopper, E.H. Silver, N.J. Westergaard and P. Orup, *Proc. SPIE* **597**, 316 (1985)
21. D.K.G. de Boer, A.J.G. Leenaers, W.W. van den Hoogenhof, *Appl. Phys. A* **58**, 438 (1994)
22. P. Lambooy, PhD Thesis, Open University Heerlen (1992)
23. H.-J. Voorma, E. Louis, N.B. Koster, F. Bijkerk, and M.J. v.d. Wiel, *Physics of X-ray Multilayer Structures*, OSA Technical Digest Series, **6**, 134 (1994)
24. H.-J. Voorma, E. Louis, N.B. Koster, F. Bijkerk, and E. Spiller, Submitted to *J. Appl. Phys.*
25. W. Jark, Thesis University of Hamburg, Internal report, Desy F41, Hasylab 85-14 (1985)
26. H. Hogrefe, D. Giesenberg, R.-P. Haelbich and C. Kunz, *Nucl. Inst. and Methods B* **208**, 415 (1983)
27. H.-J. Voorma and F. Bijkerk, *Microelectron. Eng.* **17**, 145 (1992)
28. T.E. Jewell, J.M. Rodgers and K.P. Thompson, *J. Vac. Sci. Technol. B* **8**, 1519 (1990)

# Mo/Si multilayer optics for micro-lithography

## Summary

The research described in this thesis has been focused on molybdenum/silicon multilayer x-ray optics for Extreme Ultraviolet Lithography (EUVL), a high-resolution imaging process for semiconductor fabrication. In EUVL Mo/Si multilayers are used to reflect radiation with a wavelength of 13 nm at near-normal-incidence. The topics of this thesis include the design and construction of a two-mirror imaging system, the development of a general method for analysis of multilayer structures, the development of a process for fabrication of EUV reflection masks, and the optimization of two different auxiliary techniques used during the fabrication of multilayer mirrors.

The two-mirror system including a spherical reflection mask and an illuminator, are part of a projection system, which is developed in order to allow assessment of EUV optics research aspects. The system has an intrinsic resolution of 76 nm over a medium-size image field. The construction consists of micro-mechanical systems, and the alignment is performed with a Fizeau interferometer. In order to obtain maximum intensity at the image field, mirrors with a high reflectivity at near-normal-incidence are needed. It is shown that Mo/Si multilayer mirrors with an interface roughness of below 0.4 nm rms enable a reflectivity of up to 64% at 13 nm radiation.

A new method has been developed for the analysis of multilayer mirrors using small-angle reflectivity measurements. The method is faster than fitting of the reflectivity of a modelled structure to the measured reflectivity, results in an accurate value of the density, interface roughness, and d-spacing, and needs no pre-assumption about the material composition. An additional advantage is that a distinction is made between interface roughness and layer thickness errors. A minor disadvantage is that only an average value of the period thickness is determined, rather than all individual layer thicknesses. This method facilitates the characterization of the numerous multilayers that are produced during the optimization of the fabrication processes.

The Mo/Si multilayer mirrors discussed in this thesis are produced with e-beam evaporation and two additional techniques to reduce the interface roughness and improve the reflectivity. Firstly, an enhanced substrate temperature has been used during deposition, a method in which the thermal energy is used to increase the mobility of the atoms. The results of the investigations, in a wide temperature range (300 - 550 K), show a minimum at 488 K at which the interface roughness (0.3 nm rms) is less than half of the value obtained at room temperature. Also a decrease of the Si layer thickness as a function temperature is observed. This change amounts to 15% at 550 K compared to a multilayer produced at room temperature. The changes in the Si layer thickness and the interface roughness as a function of time and temperature are explained



by diffusion-like processes, which decrease the free volume in the Si layer with increasing temperature.

The second additional technique investigated is ion bombardment of the Si layers. In this technique the energy of the colliding ions is applied to increase the mobility of the deposited atoms by simultaneously removing an additional thickness and smoothing of the layer. Both the angle ( $20^\circ - 50^\circ$ ) and the ion energy (300 eV - 2 keV) of the ion beam are optimized, using multilayer mirrors rather than single layers. Analysis of the results shows that ion bombardment induces viscous flow, which increases with ion energy as well as angle of incidence. For all ion beam parameters investigated, the effect of intermixing can be neglected. The optimal parameters for this material combination (2 keV at  $50^\circ$ ) result in a minimum interface roughness of 0.21 nm rms, which is an improvement of at least 50% compared to results published earlier.

Both additional techniques result in an almost equal interface roughness, but a difference is observed in the near-normal-incidence reflectivity. To obtain information on the structure and chemical composition of the layers, Extended X-ray Absorption Fine Structure (EXAFS) experiments are performed at both the Si-K and Mo-K edge. The results show that the Si as well as the Mo layer have an amorphous structure and that no Mo-Si compounds are formed at the interfaces. The background gas in the deposition system causes inclusion of 4.7% oxygen in the Si layer, which absorbs the soft x-ray radiation. From these experiments it is concluded that ion bombardment reduces the fraction of oxygen in the Si layer to  $\leq 0.5\%$ .

A novel procedure has been developed for the fabrication of EUVL reflection masks. The procedure involves the deposition and patterning of an absorber bi-layer (40 nm W and 25 nm C) on top of a Mo/Si multilayer mirror. The pattern is written with an e-beam pattern generator into a resist and is transferred into the bi-layer with standard etching processes. During processing, the C layer is used to protect the underlying Mo/Si multilayer mirror. The full mask making procedure has only a minor effect on the multilayer reflectivity. The C layer also shows good perspective for mask repair with a focused ion beam.

## Mo/Si multilaags-spiegels voor microlithografie

### Samenvatting

In dit proefschrift wordt het onderzoek beschreven naar molybdeem/silicium multilaagsspiegels voor Extreem Ultra-Violet Lithografie (EUVL), een afbeeldingstechniek met een hoge resolutie ten behoeve van de halfgeleiderindustrie. De Mo/Si multilaagsspiegels worden gebruikt om straling met een golflengte van 13 nm te reflecteren bij normale inval. De onderwerpen die in dit proefschrift behandeld worden zijn het ontwerp, de constructie en het uitlijnen van een afbeeldend systeem bestaande uit twee spiegels, een algemene methode voor het karakteriseren van multilagen, de optimalisatie van twee additionele technieken gebruikt tijdens de productie van deze multilagen, en een fabricageproces voor reflectiemaskers.

Een beschrijving wordt gegeven van een afbeeldend systeem van twee spiegels, een collimator en een reflectiemasker. Het ontwerp voldoet aan een groot aantal eisen voor EUVL, zoals resolutie ( $< 100$  nm) en scherptediepte ( $1 \mu\text{m}$ ). Het systeem is ontworpen om onderzoek mogelijk te maken naar de procedure voor het maken van een afbeelding in een voor zachte-röntgenstraling geschikte fotolak, het gebruik van een laserplasma röntgenbron, en het construeren en uitlijnen van röntgen-optiek. De eerste experimenten hebben een indicatie gegeven voor een resolutie van ongeveer 200 nm; deze wordt tot dusver beperkt door de eigenschappen van de fotolak.

Voor EUVL systemen is gekozen voor het gebruik van 13 nm straling, omdat voor deze golflengte multilaagsspiegels ontwikkeld zijn die een reflectie hebben van 64% en hoger bij een ruwheid van minder dan 0,4 nm rms.

Om multilaagsspiegels na de productie te karakteriseren moeten deze worden doorgemeten met röntgenstraling, waarbij het gebruik van een golflengte van 0,154 nm bij scherpende hoek van inval een standaardtechniek is. Aangezien er voor de analyse van deze metingen geen betrouwbare en snelle methode voorhanden was, is er een nieuwe methode ontwikkeld. Het grote voordeel van deze techniek boven de bestaande technieken is dat naast de d-waarde en de ruwheid, ook de variatie in de d-waarde en de dichtheid van de materialen bepaald kan worden. Tevens is de methode betrouwbaar gebleken, snel en onafhankelijk van degene die de analyse uitvoert.

Dit proefschrift betreft verder de fabricage van multilaagsspiegels met behulp van elektronenstraal-verdampen, waarbij gebruik gemaakt wordt van twee additionele technieken om de ruwheid te verminderen en de reflectiviteit te verbeteren.

De eerste techniek betreft het toepassen van een verhoogde substraattemperatuur (300 - 550 K). Bij een temperatuur van 488 K hebben de Mo/Si multilagen een minimale ruwheid (van 0,3 nm rms), hetgeen minder is dan de helft van de ruwheid van lagen die bij kamertemperatuur opgedampt zijn. Echter ook de d-waarde verandert bij toenemende substraat-



temperatuur. Deze verandering wordt veroorzaakt door een vermindering van het vrije volume van de Si laag met 15% bij 550 K ten opzichte van het vrije volume bij kamertemperatuur. Deze verandering treedt op binnen 1000 seconden na de depositie van de Si laag.

De tweede additionele techniek is het verwijderen van een vaste laagdikte Si (3,8 nm) met behulp van ionenpolijsten, waarbij de ruwheid onderzocht is als functie van de ionen-energie (300 eV - 2 keV) en de hoek van inval ( $20^\circ$  -  $50^\circ$ ). Bij de optimale polijstconditie ( $50^\circ$  en 2 keV) binnen dit gebied blijkt de ruwheid 0,21 nm rms, hetgeen een verbetering is van meer dan 50% ten opzichte van eerdere resultaten. De vermindering van de ruwheid wordt verklaard door visceuze stroming, die toeneemt met de hoek van inval en de energie van de ionen. Tevens is er aangetoond dat bij alle onderzochte ionbundel-parameters de lagen niet mengen.

Hoewel met beide additionele technieken de ruwheid van de multilagen verminderd kan worden tot 0,3 nm rms en beter, is de reflectie bij 13 nm verschillend. Om dit te verklaren zijn EXAFS metingen verricht, waarmee de chemische samenstelling en de structuur van zowel de Si als de Mo lagen onderzocht is. Uit de resultaten blijkt dat beide lagen amorf zijn, en dat er geen chemische verbindingen gevormd worden. De verminderde reflectiviteit is te verklaren doordat de temperatuur-geoptimaliseerde multilagen 4,7% zuurstof in de Si lagen bevatten. Deze fractie is significant lager in multilagen die geproduceerd zijn met ionenpolijsten, waarbij in de Si lagen maar 0,5% zuurstof aangetroffen werd. Aangezien de overige procescondities vergelijkbaar zijn, concluderen we dat door het ionenpolijsten de zuurstof uit de Si lagen verwijderd wordt. De fractie zuurstof is van groot belang bij deze multilaagsspiegels aangezien zuurstof een zeer hoge absorptie heeft van straling van 13 nm.

Tot slot wordt de fabricagetechniek voor reflectiemaskers beschreven. Voor het reflectiemasker is er gebruik gemaakt van een multilaag met daarop een absorptielaag (40 nm W en 25 nm C) met een patroon. De C laag dient er voor om de multilaag te beschermen tijdens de fabricage en eventuele reparatie van de patronen. Uit reflectiemetingen is gebleken dat het fabricageproces van het masker nauwelijks effect heeft op de reflectie van de onderliggende multilaag. Er is tevens aangetoond dat door oxydatie van de toplaag de reflectie maar 1,6% lager uitkomt t.o.v. een referentiespiegel.

## Curriculum vitae

I was born in Boston, in The United States of America, on June 12th 1966. In 1985 I received my Athenaeum diploma at Het Nieuwe Lyceum in Bilthoven. That same year my university education in physics started at the University Utrecht. In January 1992 I received my masters degree in physics. My masters thesis was about the design of an x-ray optical system for micro-lithography. This work was performed at the FOM-institute for Plasma Physics "Rijnhuizen". In January 1992 I started my PhD work on multilayer optics for micro-lithography, which is described in this thesis, also at the FOM-institute for Plasma Physics "Rijnhuizen".





## Dankwoord

Met het grote gevaar mensen te vergeten, zou ik graag iedereen willen danken die mij de afgelopen vijf jaar geholpen, gecorrigeerd, gesteund, of vermaakt heeft. In het bijzonder alle mensen die hun bijdrage hebben geleverd aan het EX2 project (met name Fred, Eric, Leonid, Norbert, David, Arjan, Casper, Henk, Emile, Joseph, en vele anderen) voor het onderzoek, de discussies, de correcties, en de samenwerking. Alle studenten, die de afgelopen jaren hun afstudeer of andere stages hebben uitgevoerd, wil ik danken voor het vele werk dat jullie ons uit handen hebben genomen. In het bijzonder Henk en Casper voor het ontwerp van de constructie van de telescoop, en Norbert, Ronald en Peter (DSRI) voor het ontwerp en constructie van de reflectometer in muco. Ik zou tevens de buitenlandse groepen willen danken voor de samenwerking, de metingen, e.d. In het bijzonder Gert (NWO-DRAL), altijd in voor het geven van een goed advies, Finn (DSRI), Salim (DSRI), Dick (PHILIPS), Paul (PHILIPS), Eric G. (LBL-CXRO), and Jim (LBL-CXRO) for the use of your reflectometers, and Yuri (IPM) and Salashchenko (IPM) for the reflectivity measurements. Tot slot wil ik me verontschuldigen bij iedereen die de afgelopen jaren te vergeefs een verzoek op mij heeft gedaan, omdat ik dacht belangrijkere zaken (dit proefschrift) aan mijn hoofd te hebben, waaronder natuurlijk Joke, en mijn familie, maar ook de Bandy Boys, Porca, en Heren 11.